N.Y.

PROPOSAL Publication No. U-4347
DOCUMENT W.O. 2273/2430
COPY OF
TOTAL PAGES:

GPO PRICE $ _____

CFSTI PRICE(S) $ _____

Hard copy (HC) 3.00

Microfiche (MF) 65

ff 653 July 65

DATE

FINAL REPORT

INVESTIGATION OF HEAT TRANSFER IN NONEQUILIBRIUM REACTING SYSTEMS

Covering the Period: July 14, 1964 to April 1, 1968

Prepared For: National Aeronautics and Space Administration
Washington, D. C.

SUBMITTED TO

Contractor: Applied Research Laboratories
Aeronutronic Division, Philco-Ford Corporation
Newport Beach, California

Contract No.: NASw-999

Prepared By: John L. Richardson
Richard J. Getz

Approved By: H. Shanfield, Manager
Chemistry Laboratory

April 1, 1968

N68-23192 (ACCESSION NUMBER)
138 (PAGES)
CR-94538 (NASA CR OR TMX OR AD NUMBER)
(THRU)
1 (CODE)
33 (CATEGORY)
FACILITY FORM 602

APR 1968
RECEIVED
NASA STI FACILITY
INPUT BRANCH

PHILCO
PHILCO-FORD CORPORATION
Aeronutronic Division
Newport Beach, Calif. • 92663

ABSTRACT

An experimental investigation was undertaken in order to determine how finite homogeneous reaction rates affect energy transfer rates in the case of fully developed turbulent tube flow. Both the time-average and turbulent scalar properties of the nonequilibrium reacting flow were measured and compared to similar data obtained for the case of nonreacting turbulent tube flow. Special instrumentation and a recirculating flow system were developed for use with the gaseous reacting NO_2 system at elevated temperatures and pressures. The results showed how the existing model for predicting the effect of reaction rate on heat transfer rate must be modified in order that better agreement can be obtained between the theoretical predictions and the experimental data. The turbulence measurements showed that the concentration and temperature fluctuation intensities are unusually large when the flow is undergoing a homogeneous nonequilibrium reaction compared with the intensities measured in a similar, but nonreacting, flow. This result helps, in part, to explain why the existing prediction model is of limited utility. Areas requiring further investigation were delineated.

START CONTINUATION PAGES HERE

CONTENTS

SECTION		PAGE
1	INTRODUCTION	1
	1.1 Background	1
	1.2 Program Objectives	6
2	EXPERIMENTAL	9
	2.1 Properties of the Reacting System	9
	2.2 Flow System	12
	2.3 Instrumentation	25
	2.4 Flow System Operation	43
3	RESULTS	51
	3.1 Data Reduction	51
	3.2 Reduced Data	51
	3.3 Errors and Corrections	62
	3.4 Friction Factor Results	64
	3.5 Nusselt Number/Reynolds Number Correlations	66
	3.6 Comparison of Data with Calculated Results from Model II	69
	3.7 Concentration Profiles — Time-Average Data	77
	3.8 Momentum/Energy Transport Analogy Considerations	82
	3.9 Normalized Radial Profiles of Specific Enthalpy and Temperature	85
	3.10 Eddy Diffusivities — Their Estimation and Comparison	87
	3.11 Turbulent Temperature Results — Nonreacting and Nonequilibrium Reacting Systems	91
	3.12 Turbulent Concentration Results	101
4	CONCLUSIONS	108
	4.1 Experimental Results	108
	4.2 Areas Requiring Further Investigation	111
	ACKNOWLEDGMENTS	113

START CONTINUATION PAGES HERE

CONTENTS (Continued)

SECTION	PAGE
NOMENCLATURE	114
APPENDIX	127
REFERENCES	131

START NEW SECTION PAGE HERE

STOP TOP 1 - PAGE TEXT HERE WHEN ILLUSTRATION FOLLOWS

START BOTTOM 2 - PAGE TEXT HERE WHEN ILLUSTRATION PRECEDES

SECTION 1

INTRODUCTION

1.1 BACKGROUND

There are numerous practical situations in which a knowledge of the heat transfer rate to or from a chemically reacting flow is needed. The prediction of the cooling requirements for heat exchangers on rocket combustion chamber walls, the prediction of heating or cooling requirements for flow reactors, and the prediction of heating loads on re-entry bodies are examples of design situations which require workable methods for determining the extent to which the chemical reactions in the flow stream affect the heat transfer rates (flow in conduits or flow over bodies). The approach required for treating each situation must be tailored to not only the fluid mechanics of the flow field (laminar or turbulent, developing or fully developed, mass addition at the wall, particles or droplets in the flow, etc.) but must also be consistent with the chemistry (binary or multicomponent, irreversible and/or reversible reactions, homogeneous and/or heterogeneous reactions, chemical equilibrium or nonequilibrium conditions prevailing, plasma or neutral chemistry, etc.) as well as any other peculiarities of the heat transfer situation (ablation, radiation, etc.) which may be present in the flow system of interest. Work on elementary aspects of the problem was not reported before the mid-1950's. Since that time considerable attention has been devoted to the problem including studies of heat transfer for both laminar and turbulent reacting flows and for the three different modes of heat (or energy) transfer — conduction, natural (or free) convection, and forced convection.

Several reviews of the problem have been made (1)(2)(3)(4). For convenience, a considerable number of experimental studies in the labora-

tory have used the reversible, homogeneous, equilibrium dissociating $N_2O_4 \rightleftarrows 2\ NO_2$ system (endothermic) at 1 to 2 atm total pressure in the temperature range of 100 to 570°F* and the nonequilibrium dissociating $2\ NO_2 \rightleftarrows 2\ NO + O_2$ system (endothermic) at 1 to 10 atm total pressure and 700 to 1200°F**. These include the work of Mason and coworkers (1)(5)(6)(7)(8)(9)(10), Brokaw and coworkers (2)(11)(12)(13), Smith and coworkers (14)(15)(16)(17), Presler (18), and Brian and coworkers (19)(20)(21)(22)(23). Some studies have also been done with the irreversibly dissociating ozone system, $2\ O_3 \rightarrow 3\ O_2$ (exothermic; system diluted with O_2), by Edwards and Furgason (24)(25).

In the case of reversible, equilibrium, homogeneous reacting systems, various studies (1)(6)(7)(10)(11)(18) have clearly shown that conventional heat transfer correlations for the turbulent flow of nonreacting gases are applicable if the proper substitution of thermodynamic and transport properties and driving forces (to specific enthalpy) is made in the dimensionless correlations and if the fluid properties are evaluated at a suitable film temperature. Exact calculations can give an adequate representation of both the laminar flow situation (16)(17) and of the stagnant film case (8)(12) even if a nonequilibrium reaction is occurring.

In the case of reversible nonequilibrium reacting systems in turbulent flow, Brian and coworkers (19)(20)(21)(23) have developed several models, based on various assumptions, for the prediction of the heat transfer rate between the wall and the fluid. In Table 1 a listing of each of the key assumptions associated with these models is presented.*** A comparison made between the results calculated for the film model (I) and results calculated for the model which incorporated eddy diffusivities based on nonreacting tube flow data (II) showed that for $N_{Le_\xi} \sim 1$ systems, the film

---

* Characteristic chemical reaction times for this system at these conditions are on the order of 10^{-6} seconds.

** Characteristic chemical reaction times for this system at these conditions are on the order of 1 to 10^{-2} seconds.

*** Symbols are defined in the Nomenclature.

TABLE 1

ANALYSES AVAILABLE FOR PREDICTING ENERGY TRANSFER IN NONEQUILIBRIUM REACTING TURBULENT FLOWS (SELF-MIXING CASE)

Key Features of the Model	I	II	III	IV
Flow Field Model	Thin Film (Plane or Cylindrical)	Pipe Flow (Fully Developed)	Thin Plane Film	Flow Outside a Rotating Cylinder (Stagnant Bulk Fluid)
Reaction Stoichiometry	$aA + bB \rightleftarrows uU + vV$	$A \rightleftarrows vV$	$2\,A \rightleftarrows 3\,U$	$A \rightleftarrows vV$
Temperature Driving Force	$\Delta T \rightarrow 0$	$\Delta T \rightarrow 0$	ΔT finite	$\Delta T \rightarrow 0$
Chemical Kinetic Expression	General* (Heterogeneous Kinetics also Included)	General*	Molecularity = Stoichiometry	General*
Bulk Boundary Condition	Chemical Equilibrium	(Nonequilibrium, Steady State Reaction Rate), $(\partial r_i/\partial L)_r = 0$	Chemical Equilibrium	Chemical Equilibrium
Eddy Diffusivity Model	$\varepsilon_i \equiv 0$ in Film $\varepsilon_i \rightarrow \infty$ in Bulk	$\varepsilon_H \equiv \varepsilon_m \equiv \varepsilon_M$ $\varepsilon_M \equiv \varepsilon_{M_\xi}$ $(r=r_o$ to $r=\frac{1}{2}r_o)$ $\varepsilon_{M_\xi}(r=0) \equiv \frac{1}{2}\varepsilon_{M_\xi}(r=\frac{1}{2}r_o)$ Linear Variation Assumed: $r=\frac{1}{2}r_o$ to $r=0$	$\varepsilon_i \equiv 0$ in Film $\varepsilon_i \equiv \infty$ in Bulk	$\varepsilon_H \equiv \varepsilon_m \equiv \varepsilon_M$ $\varepsilon_M \equiv \varepsilon_{M_\xi}$ (flow outside a rotating cylinder)
Effect of Turbulence on Reaction Rates	Neglected**	Neglected**	Neglected**	Neglected**
Reference	(19)***	(20)	(21)	(23)

*Molecularity does not need to correspond to stoichiometry.

**$\bar{r}_i \equiv \bar{r}_i(\bar{T},\bar{C}_i)$; no dependence of $\bar{r}_i$ on turbulent intensities (temperature or concentration) included.

***See also (12) and (13).

3-A

3-B

theory was indeed a good approximation. No experimental data for tube flow were available to check this result. The effect of finite driving force was also investigated. In Figure 1, calculations are presented which show a comparison between the ΔT finite case and the $\Delta T \rightarrow 0$ case. The dimensionless heat transfer coefficient ratio, φ, is shown as a function of the characteristic time ratio (molecular diffusion to chemical reaction), $\sqrt{m}$. As $\sqrt{m} \rightarrow 0$, the system approaches the "locally frozen" or nonreacting state. As $\sqrt{m} \rightarrow \infty$, the system tends toward the chemical equilibrium state. In between these two states, the system exhibits nonequilibrium behavior.* The solid lines are the results calculated for the case of $\Delta T = 190^{\circ}F$ (21). The significant effect of the equilibrium thermal conductivity on the calculated results is apparent. The dashed line was calculated for the case of $\Delta T \rightarrow 0$ (19). A comparison of the results for the same value of k/k_{ξ} (= 4.0) shows that in the $\sqrt{m} < 2$ range the theoretical line for the $\Delta T \rightarrow 0$ case is shifted from the line for the ΔT finite case to higher values of $\sqrt{m}$.

The only data which are available for checking the validity of the models listed in Table 1 are the data obtained by Bodman (22)(26) for the case of turbulent flow outside a rotating heated cylinder immersed in a chamber of stagnant gas. The experiments were made with dissociating NO_2. The experimental results were compared with both the film theory (22) and with the predictions derived from a model specifically developed for flow outside a rotating cylinder (23). Most of the data agreed with the film theory predictions within ± 10% (a few of the results deviated from the calculated results by as much as 25%). Calculated results derived from the model based on an eddy diffusivity (23) were in close agreement (< 4%) with the film theory result for values of $\eta < 50$ ($\eta \sim 4$ in the NO_2 dissociating system) over a wide range in Reynolds number. Since the gas

*Note that h^*, or the measure of resistance film thickness, appears in both the ordinate and the abscissa of the figure. Thus the gross fluid mechanical features are essentially divided out and the primary information left is the effect of reaction rate on heat transfer rate.

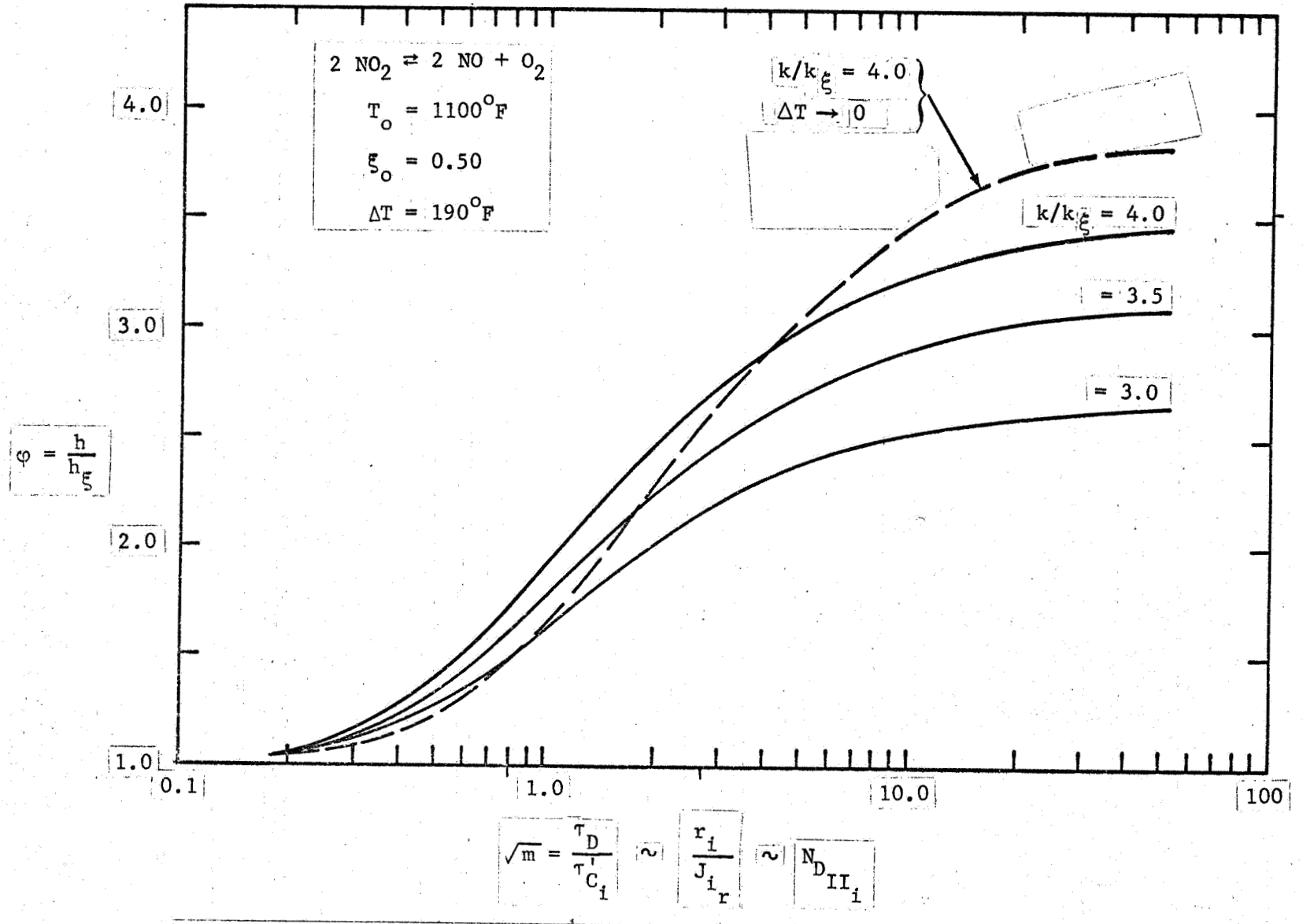

FIGURE 1. ESTIMATED EFFECT OF CHEMICAL REACTION RATE ON HEAT TRANSFER COEFFICIENT ($N_{Le_\xi} = 1$) (19)(21)

far from the surface of the rotating cylinder was essentially stagnant, the assumption of chemical equilibrium in the bulk was valid.

No data are available for testing the assumptions embodied in the model (II) derived for fully developed turbulent tube flow (20). In particular, the steady state reaction rate assumption of this model has not been experimentally checked.

The investigations referred to so far in this review were concerned only with the time-average properties of turbulent reacting flows of the "self-mixing" type (27). Various approaches toward gaining an understanding of how both the time-average and fluctuating quantities (scalar and momentum) in a turbulent flow are affected by chemical reactions have been made by several investigators (28)(29)(30)(31)(32). The results so far obtained via the statistical turbulence theory approaches, while showing promise for ultimately providing prediction tools for design purposes, have not yet provided a practical alternative to the models which have neglected the details of the turbulent mixing processes and have resorted to the use of eddy diffusivities measured for nonreacting flows.

1.2 PROGRAM OBJECTIVES

Because of the limitations of the available models for predicting the effect of reaction rate on turbulent heat transfer rates, and because of the essentially complete lack of experimental data (particularly in the case of tube flow) for critically testing any model, an experimental research program was undertaken with the overall objective of determining how finite homogeneous reaction rates can affect energy transfer rates for the practical case of fully developed turbulent tube flow.

The approach taken in this investigation consisted of the following steps:

a. Selection of an appropriate homogeneous reacting system for use in laboratory experiments

b. Selection, based on the results of heterogeneous kinetics measurements, of those materials of construction whose surfaces will neither react with the selected gaseous system at the temperatures and pressures of interest nor alter its homogeneous reaction rate (heterogeneous or catalytic effect)

c. Calculation of the required thermodynamic and transport properties (the homogeneous reaction rates of the selected system must be well known)

d. Design, fabrication, and test (with air) of a recirculating flow loop for heat transfer measurements with the selected system over the ranges of temperature, pressure, and flow rate required for the system to exhibit nonequilibrium behavior

e. Measurement of the heat transfer rates in the nonequilibrium reacting system over a range of temperatures, pressures, and flow rates

f. Development of an optical probe for measuring the local concentration of one of the chemical species participating in the reaction

g. Development of a fast response temperature sensor for use in measuring the local temperature

h. Measurement of radial profiles under various heat transfer conditions using these instruments

i. Analysis of the data obtained from these experiments including: comparison of experimental data with the predictions of available models, consideration of the existence of an analogy between turbulent energy and momentum transport in nonequilibrium reacting systems, estimation and comparison of eddy diffusivities, and consideration of the

implications of statistical turbulence theory.

The experimental program undertaken in order to complete these steps is described in Section 2. The results are presented in Section 3.

SECTION 2

EXPERIMENTAL

2.1 PROPERTIES OF THE REACTING SYSTEM

2.1.1 SELECTION OF REACTING SYSTEM

Based on a survey of the homogeneous kinetics literature and the results of selected thermodynamic calculations [$\xi_e(T,P)$, $\Delta\tilde{H}_R/RT$], the dissociating NO_2 ($2\ NO_2 \rightleftharpoons 2\ NO + O_2$) and dissociating NOCl($2\ NOCl \rightleftharpoons 2\ NO + Cl_2$) were found to be the most promising candidate systems for use in the experimental studies. Both systems exhibit the required characteristic reaction times at temperatures and pressures not far from ambient conditions. In addition, the effect of the reaction on the equilibrium thermal conductivity of each of these systems is expected to be significant. Finally, the calculation of the various thermodynamic and transport properties required for the analysis of the heat transfer data was expected to be relatively straightforward. In the final analysis, the NO_2 system was selected primarily because heterogeneous effects were known to occur in the nitrosyl chloride system at higher temperatures, while such effects were not expected in the case of the nitrogen dioxide system. Also, some thermodynamic and transport property data had already been reported for the equilibrium reacting NO_2 system. Other systems which were considered but which were ultimately eliminated for various reasons included the dissociating N_2O_4, HI, NH_3, SO_2Cl_2, and SO_3 systems.

2.1.2 HETEROGENEOUS EFFECTS ON THE NO_2 DECOMPOSITION

Even though the literature on the kinetics of decomposition of NO_2 show that the reaction is second order and homogeneous (33)(34)(35), no kinetic data were reported for this system in contact with materials such

as stainless steel — a useful material for construction of the heat transfer loop.

Differential pressure measurements were made of the rate of NO_2 decomposition in contact with various materials compared to its rate of decomposition while in contact with quartz at the same temperature and total pressure and in the same surface to volume ratio expected for the test section of the heat transfer loop. A summary of the rate constant data, expressed as a ratio of the homogeneous rate of decomposition divided by the measured increase in this rate (expressed in terms of a first order rate constant) caused by the presence of a clean surface of the material in question in contact with the NO_2, is given in Table 2. The stainless steels, nickel, aluminum, Inconel, and platinum were all found to lack catalytic activity. In all but the later case, a protective non-catalytic film (oxide and/or nitride) was formed at temperatures less than 600°F. The film appeared to be stable with respect to thermal and mechanical stresses and tended to provide a non-catalytic coating with respect to the NO_2 decomposition.

Corrosion tests carried out with both 316 stainless steel and aluminum at ~ 600°F and 4.6 atm in dry NO_2 for extended periods of time showed that, other than the formation of a slightly discolored film on the surface, the stainless steel had not changed in weight and was not corroded. On the other hand, the aluminum exhibited severe surface pitting.

Based on these results, 316 stainless steel was selected for the material of construction of the test loop, the total head probe, and the static temperature probe.

2.1.3 THE THERMODYNAMIC AND TRANSPORT PROPERTIES OF THE DISSOCIATING NO_2 SYSTEM

The thermodynamic and transport properties of both the frozen and equilibrium reacting NO_2 system used in this investigation were those calculated by Svehla and Brokaw (13)(36). The properties were tabulated for temperatures from 300 to 1280°K in 20°K increments and for pressures

TABLE 2

CATALYTIC EFFECT ON THE NO_2 DISSOCIATION OF VARIOUS MATERIALS COMPARED TO QUARTZ

Material	P_o (mm Hg)	T_o (°C)	$\frac{k_D C_o}{k_w}$
316 Stainless Steel+	46	324	49
	40	326	>200
	127	349	>200
Aluminum+	64	325	>200
	46	325	>200
Nickel+	51	326	1.6*
	60	327	>200
Graphite+	60	332	0.24
	34	329	0.68
	114	334	2.4
Steel+	56	325	0.92*
304 Stainless Steel+	44	327	2.2*
	70	326	>200
	154	325	>200
Inconel+	64	325	6.5*
	83	326	>200
"Pure" Platinum++ (99.95%)	66	328	124*
	81	331	>200
Thermocouple Platinum++ (99.99%)	70	325	65*
	52	325	>200

+Surface/volume = 1.08 cm^{-1}.

++Surface/volume = 0.044 cm^{-1}.

*Run was made without previously exposing the metal to nitrogen dioxide.

from 0.01 to 100 atmospheres. In the pressure range of 1 to 11 atm, all of the properties were tabulated at increments of 1 atm. These results are in good agreement with those obtained by Fan and Mason (37) for the same system at 1 atm total pressure. In formulating the Damkohler number (second type) and $\sqrt{m}$, it was necessary to have values for the binary ordinary molecular diffusion coefficients. These were obtained from Brokaw and Svehla (36) and Bodman (26).

Values of ξ_e, the equilibrium degree of advancement (related to the fraction dissociated), of both the N_2O_4 and NO_2 decompositions is shown in Figure 2. Also in this figure, the equilibrium and frozen thermal conductivities are shown for the two dissociating systems as a function of temperature for 1 and 10 atm total pressure.

2.1.4 THE HOMOGENEOUS KINETICS OF THE NO_2 REACTING SYSTEM

The forward and reverse specific reaction rate constants for the NO_2 reacting system have been measured by a number of different investigators (33)(34)(35)(26). The data compiled by Bodman (26) is shown in Figures 3 and 4.

It is of interest to note how the fraction of NO_2 decomposed depends on time and temperature. Calculated results obtained for 1 atm using the forward reaction rate data of Rosser and Wise (33), and the equilibrium constant data of Giauque and Kemp (38) are given in Figure 2 (1). It is apparent from these results that the characteristic chemical reaction time for NO_2 decomposition is between 0.1 and 1 sec for temperatures between 1200°F and 800°F. These times are decreased as the total system pressure is increased.

2.2 FLOW SYSTEM

A number of preliminary calculations were made using the model of Brokaw (13) in order to determine the conditions which must exist in the heat transfer test section in order for the dissociating NO_2 system to exhibit nonequilibrium behavior. The results of these calculations

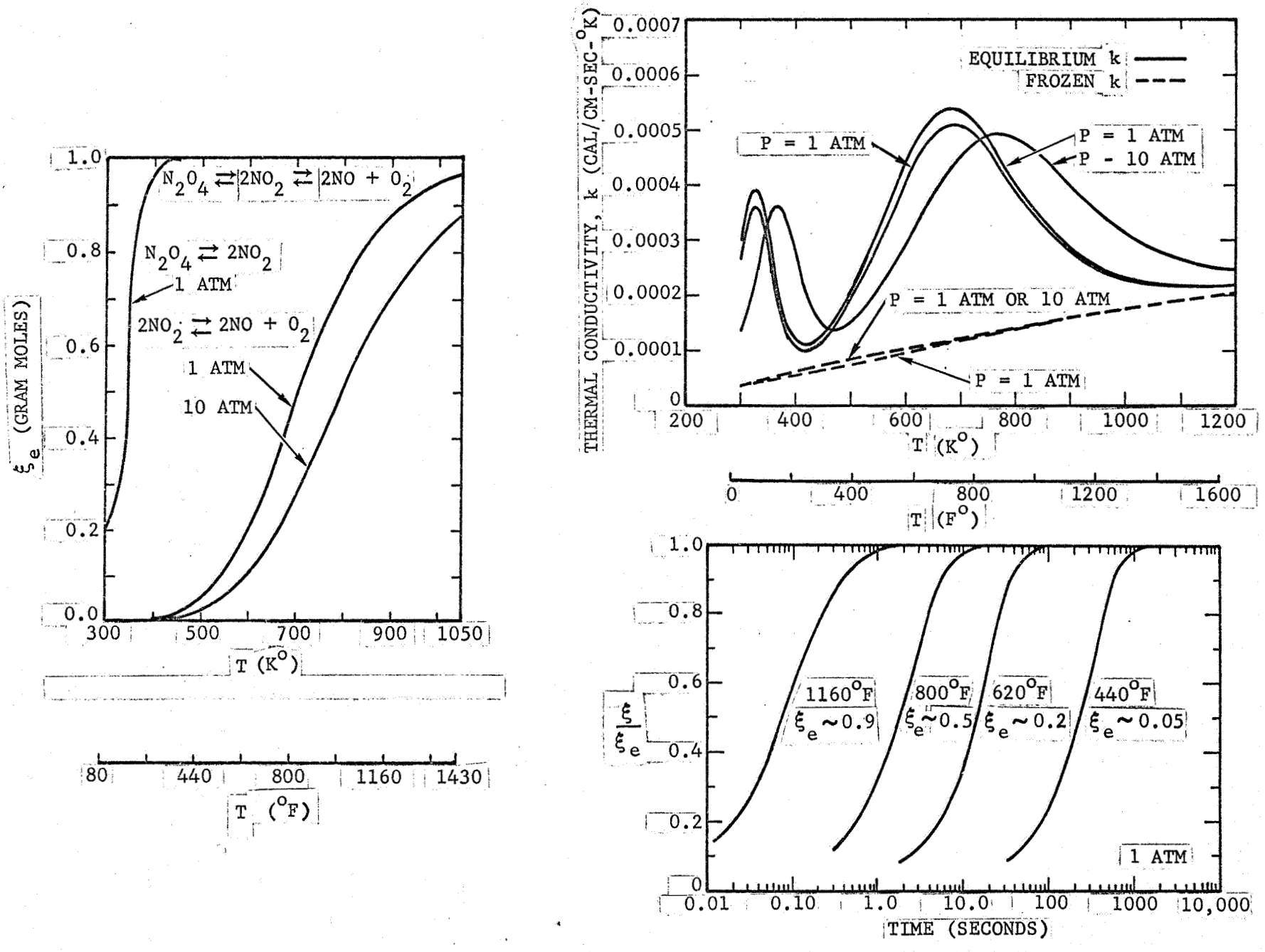

FIGURE 2. SELECTED THERMODYNAMIC, TRANSPORT, AND KINETIC PROPERTIES OF THE N_2O_4-NO_2-NO-O_2 SYSTEM

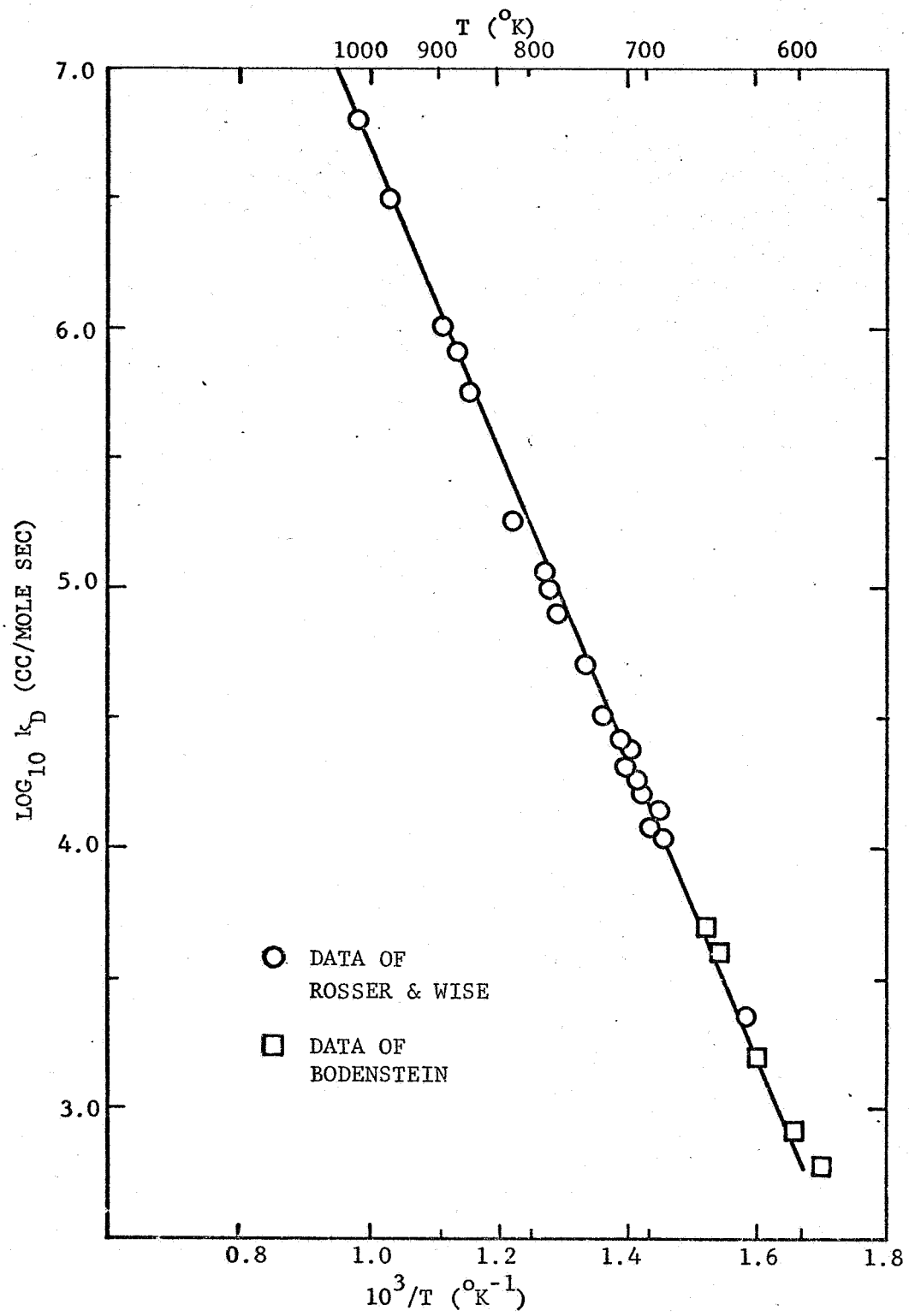

FIGURE 3. SPECIFIC RATE CONSTANT FOR THE DECOMPOSITION OF NITROGEN DIOXIDE (26)

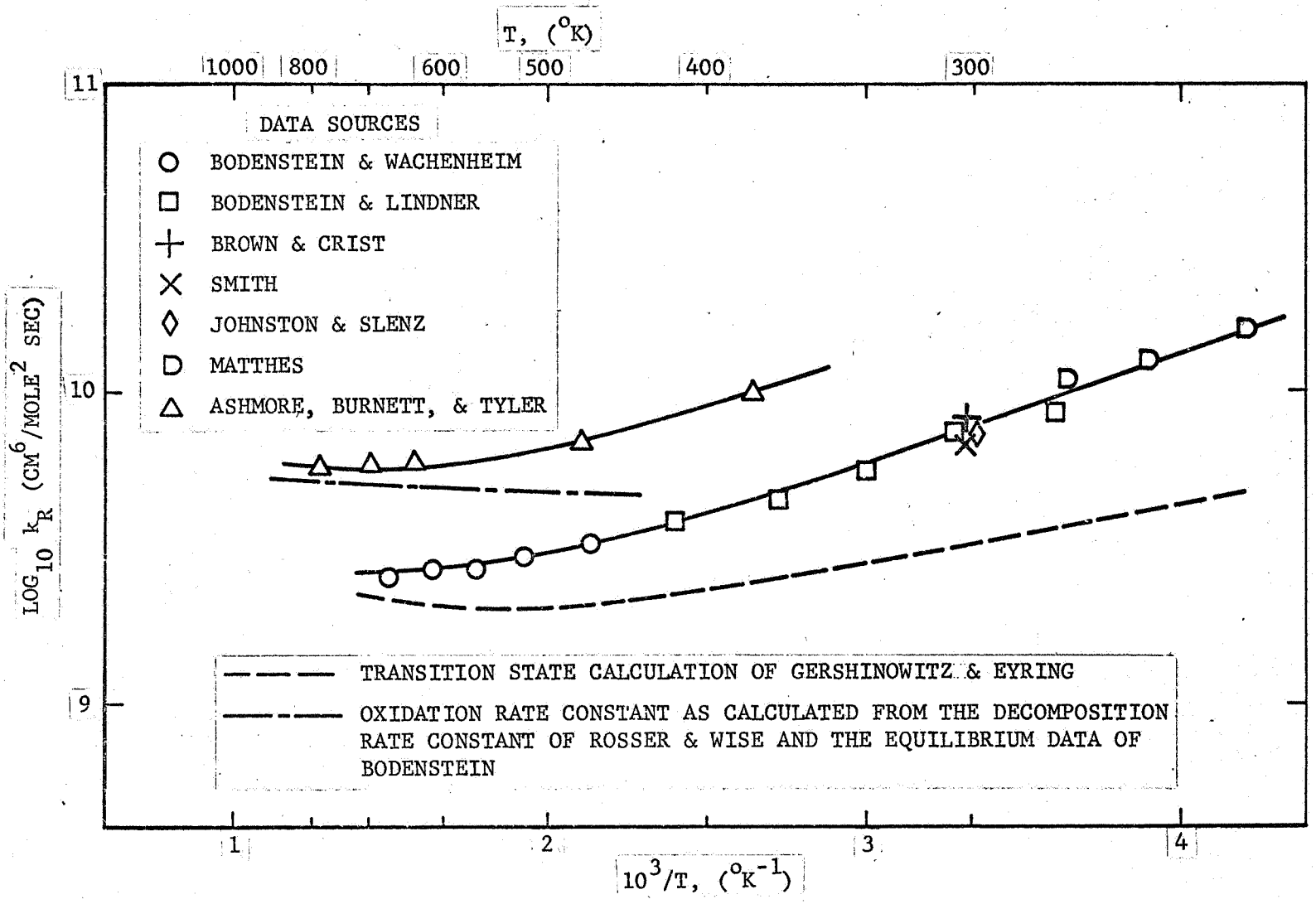

FIGURE 4. SPECIFIC RATE CONSTANT FOR THE OXIDATION OF NITRIC OXIDE (26)

clearly showed that the system must operate at temperatures as high as 1200°F and over a range of pressures from 1 to 10 atm for Reynolds numbers greater than 3,000 if nonequilibrium conditions were desired in the region between the wall and the core of the tube flow. A two-inch I.D. test section size was chosen in order that probes with support tubes as large as ¼" in outside diameter would not cause excessive blockage and distortion of the flow.

2.2.1 PIPING SYSTEM AND GASKETS

A schematic layout of the recirculating test loop is shown in Figure 5. All metallic parts were constructed of 316 stainless steel. The key overall dimensions of the loop, including the nominal pipe sizes are shown in Figure 6. All main piping connections were made with flanges and "Flexitallic" gaskets (layered chevron construction of blue asbestos and stainless steel) rather than screwed connections. The number of flanged joints was kept to a minimum in order to reduce the leakage control problem. Pipe wall and flange thicknesses were selected according to standard ASME 300 psig design in order to account for the elevated temperatures needed at the maximum expected test pressure of 150 psig. Expansion joints were required at the several locations shown in Figure 5. The piping system was thoroughly cleaned before NO_2 was brought into contact with it.

As is shown in the top part of Figure 5, a plenum section (containing screens, straightening vanes, and a contoured contraction) preceded the three portions of the test section and was designed to properly prepare the flow for its passage into the test section.

2.2.2 TURBOBLOWER WITH MECHANICAL SHAFT SEAL

The prime mover for the system was a 3 horsepower, 4 bearing, overhung turboblower* rated at 100 ICFM for 1 psi with gas of specific gravity equal to 1.588 at 800°F and 175 psia (an approximation to the upper operating

*Manufactured by the Spencer Turbine Co., New Haven, Conn.

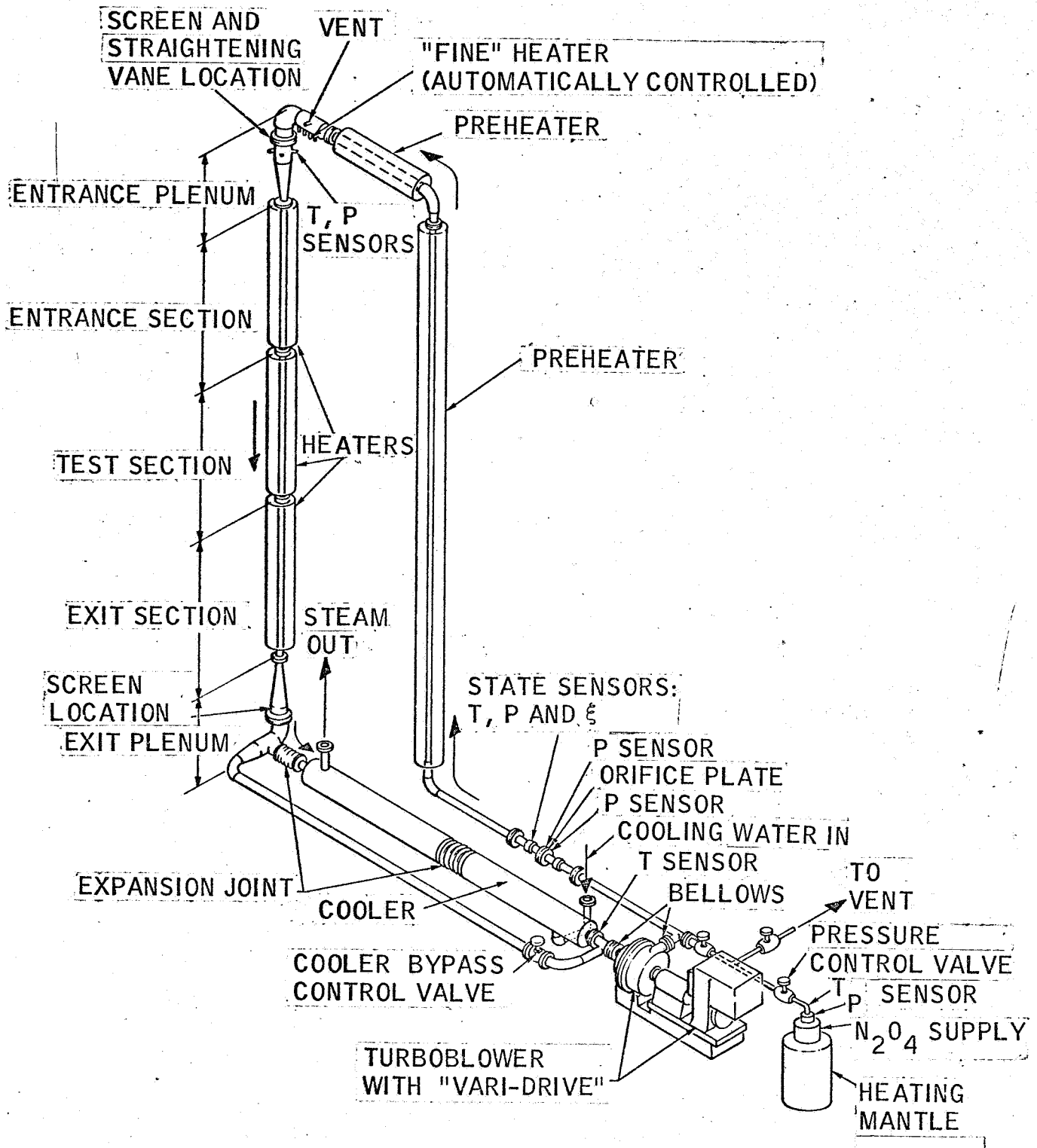

FIGURE 5. RECIRCULATING FLOW SYSTEM

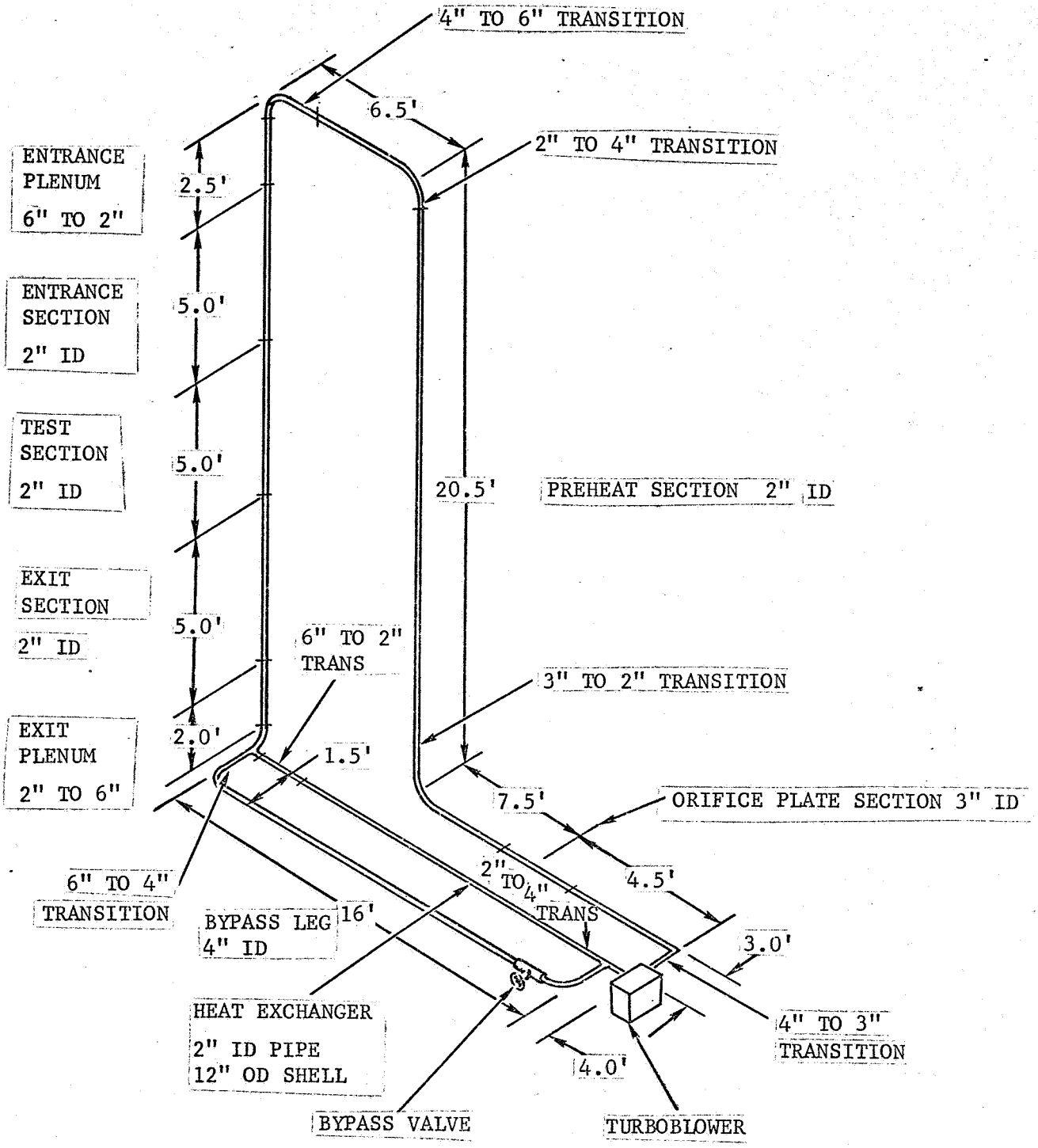

FIGURE 6. OVERALL DIMENSIONS AND NOMINAL PIPE SIZES OF THE RECIRCULATING FLOW SYSTEM

limit anticipated with the NO_2 system at the blower). The blower had 4" flanged inlet and outlet connections and was also provided with a 1" bypass line valved so as to provide flow rate control down to very low flow rates. Primary control of the flow rate was accomplished with a "Varidrive" variable speed motor system directly coupled to the blower shaft.

The seal between the hot reacting gases in the blower shell (at pressures to 10 atm) and atmospheric air was accomplished with a mechanical seal (Sealol #605 double bellows seal) cooled externally with water and attached to the rotating shaft of the blower. The gas seal occurred at the interface between a polished graphite ring rotating against a polished Stellite surface fixed to the blower shell. Great difficulty was encountered in effecting an adequate seal until various design modifications were made to the seal housing, the mounting plates, the static gaskets, and the bellows supports. Also, it was found that the alignment in all directions of the seal and shaft relative to the blower shell was an extremely critical factor in achieving the seal. The blower is now capable of running for extended periods of time with its shell heated to a temperature as high as 725°F without any significant leakage at the seal. What small NO_2 leakage does occur at the seal is not a hazard as the gas readily dissolves in the seal cooling water flow and passes to the drain.

A view of the turboblower is shown in the foreground of Figure 7. This figure shows the system before addition of the heating elements, instrumentation, cooling lines, guard heaters, etc. The lower portion of the test section and the exit plenum are visible in the background. A two level platform system was built in order to provide access to the various parts of the vertical sections. A view of the system after the insulation and cooling lines had been installed is shown in Figure 8.

2.2.3 HEATING AND ASSOCIATED CONTROLS

The heating was accomplished with ~ 30 kw of ac power supplied to nichrome wire embedded in semi-cylindrical annular elements cast from

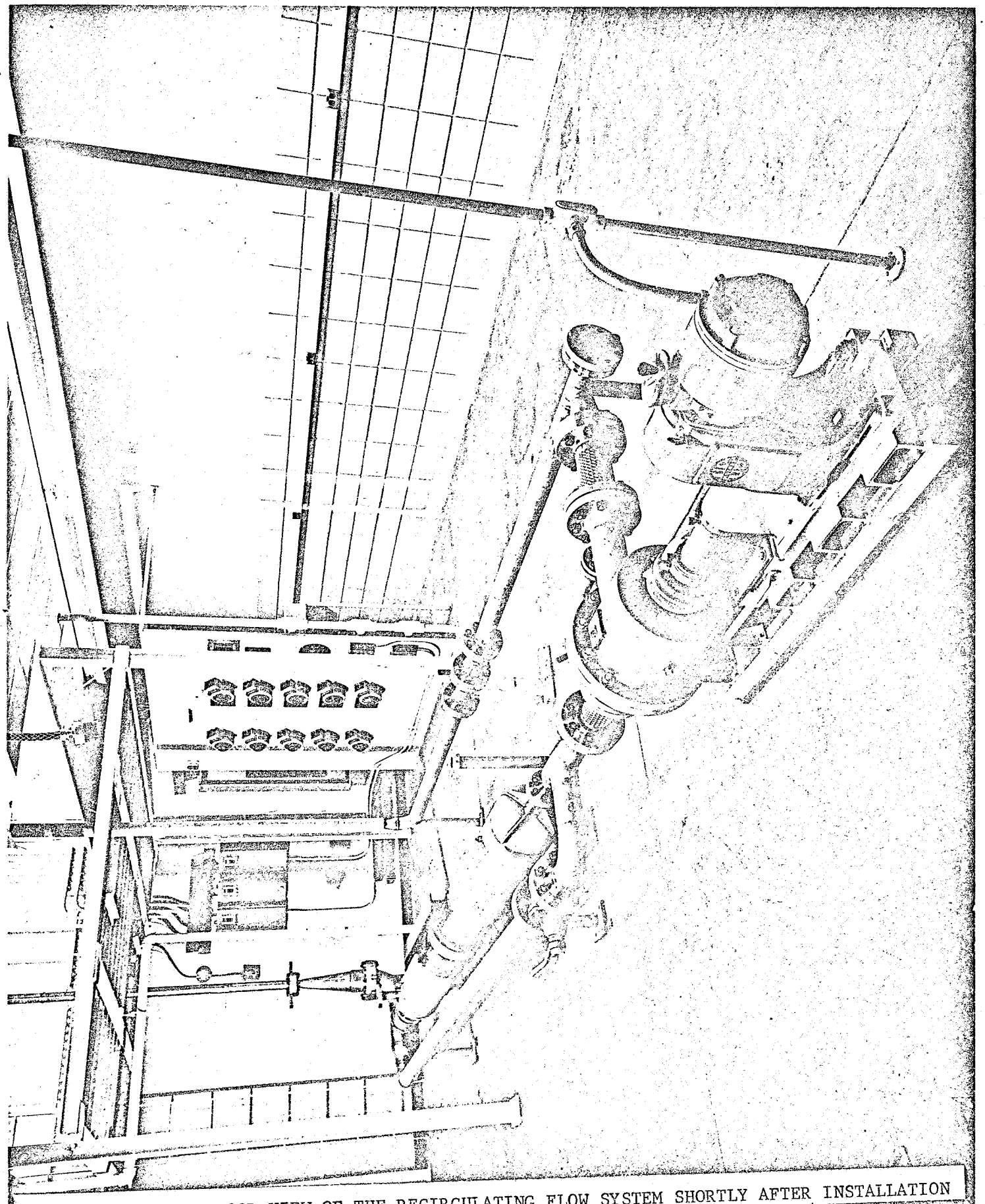

FIGURE 7. FIRST FLOOR VIEW OF THE RECIRCULATING FLOW SYSTEM SHORTLY AFTER INSTALLATION

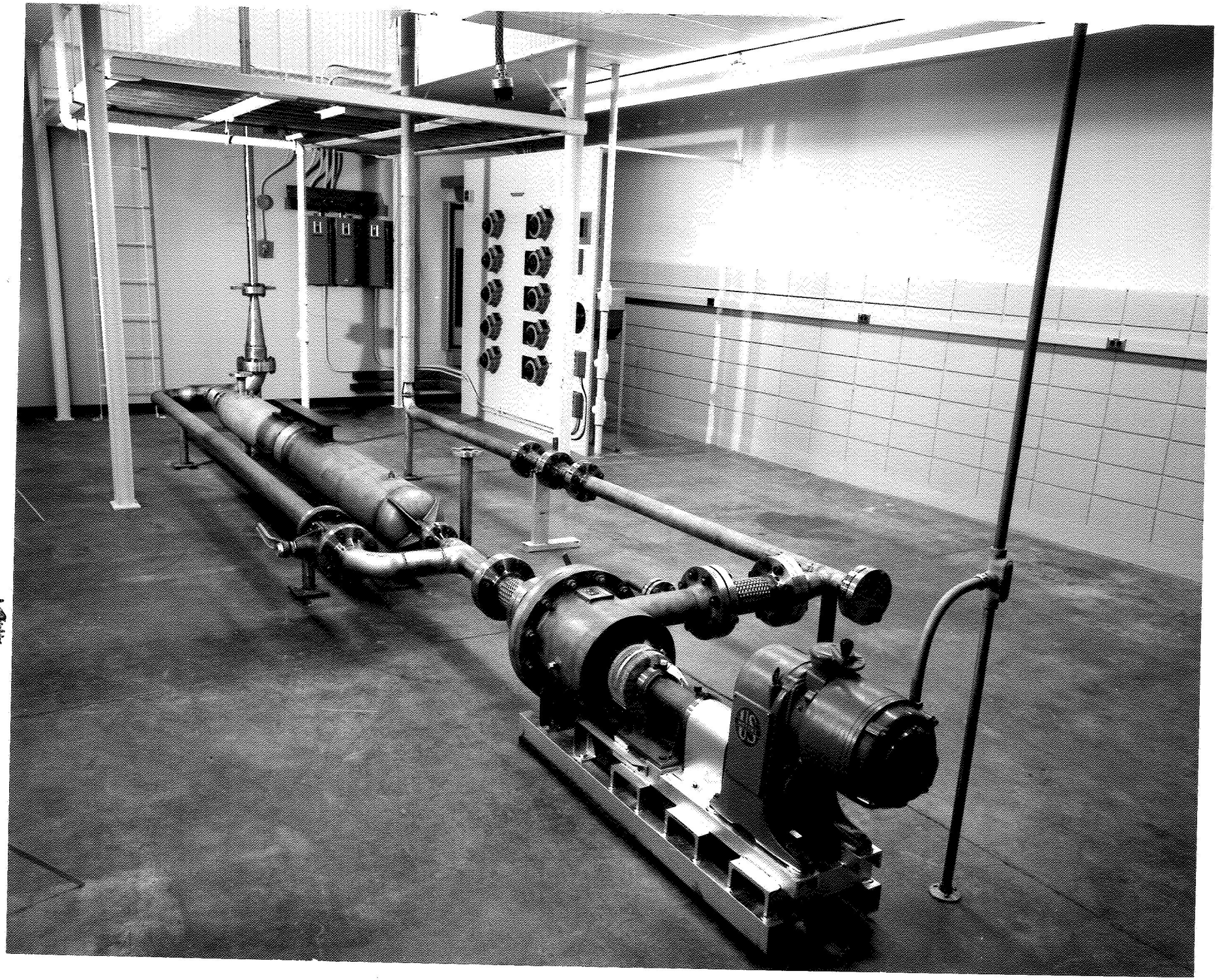

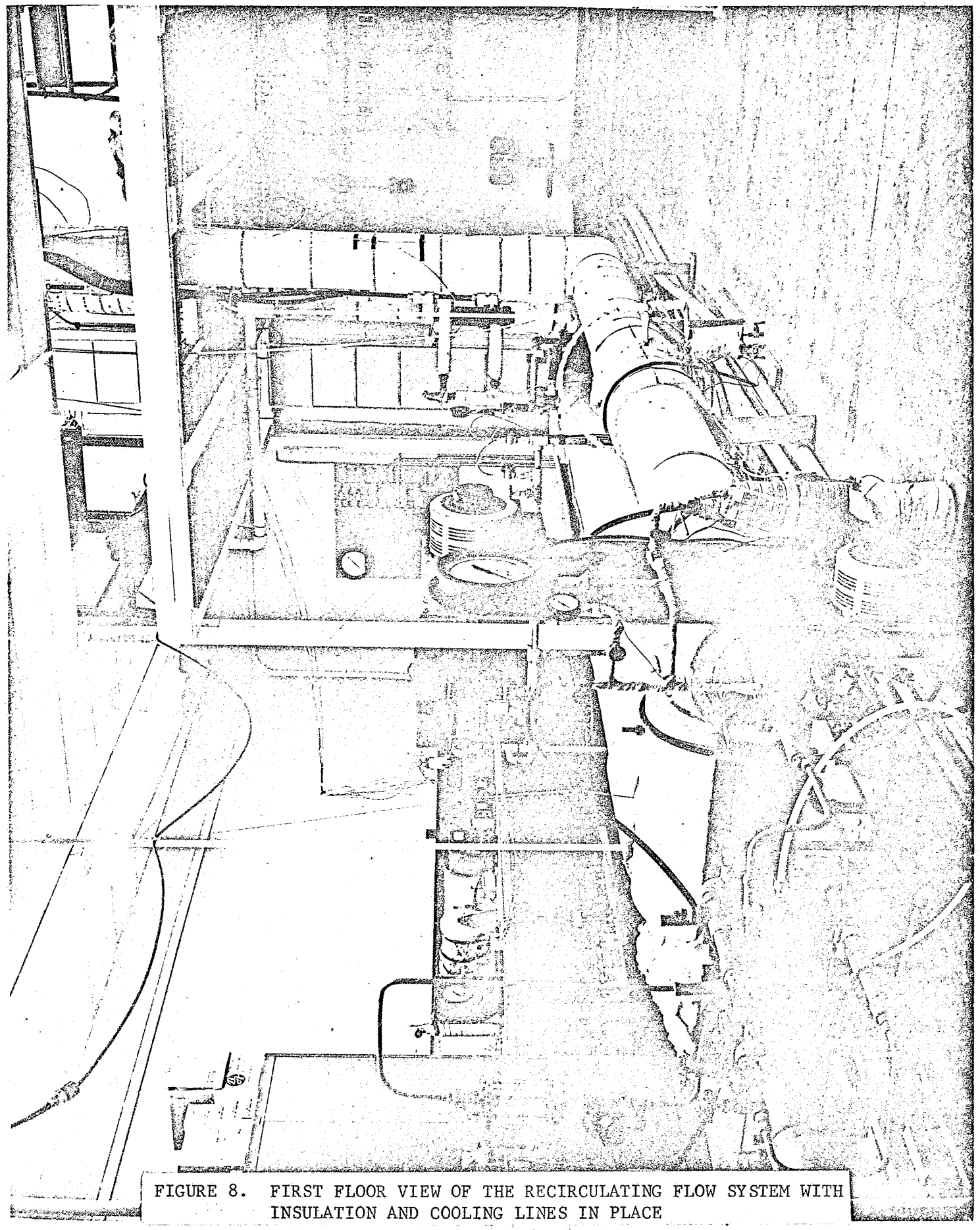

FIGURE 8. FIRST FLOOR VIEW OF THE RECIRCULATING FLOW SYSTEM WITH INSULATION AND COOLING LINES IN PLACE

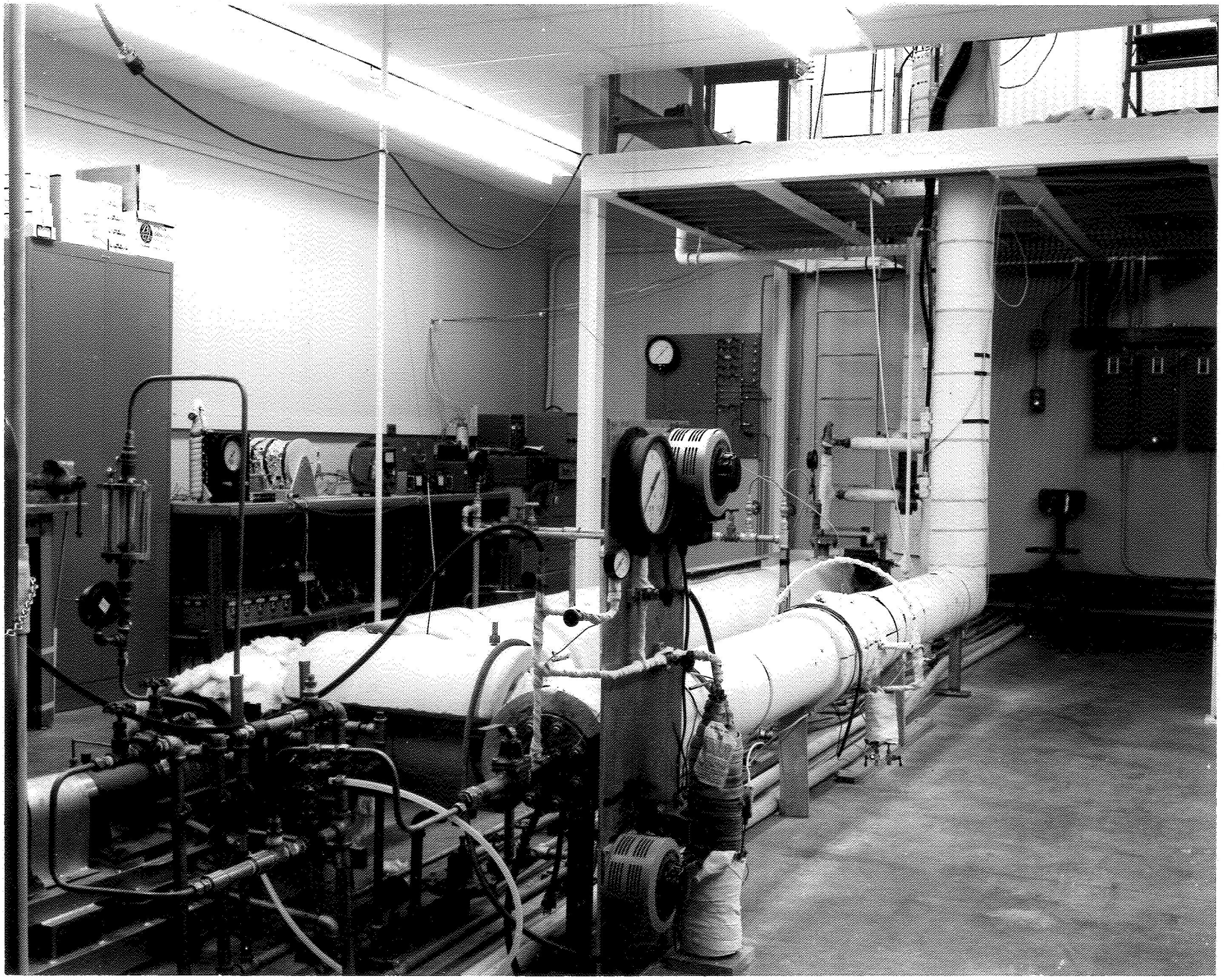

alumina. The heating elements were each 1 foot long, conformed closely to the outside dimensions of the pipe, and were capable of dissipating $\sim$ 1 kw of electrical power. The general distribution around the piping system is shown in Figure 5. The five 1-foot long heating elements in the center test section were controlled by proportional-mode type controllers so as to produce a desired back wall temperature (kept constant along the test section length). The other ten heating elements in the entrance and exit sections were controlled manually with autotransformers. Both on/off controllers and a large autotransformer were used to control the preheater elements. The "fine" or trim heater located at the entrance to the top plenum was controlled by a Leeds & Northrup controller containing proportional, reset and rate modes of control. Control of the bulk gas temperature entering the top plenum was better than $\pm$ 1°F. A portion of the electrical power control panel in the early stages of assembly of the system is shown in Figure 7.

Several of the cast alumina heating elements used on the test section (nominal 2" double extra heavy pipe honed out to 1.952" on the I.D.) were provided with holes in order to provide access for the probe holders and thermocouples spot welded to the back wall of the pipe. Numerous Chromel-Alumel thermocouples were located throughout the system in order to monitor the temperature and in order to adjust the manual controls accordingly.

2.2.4 NUCLEATE BOILING HEAT EXCHANGER

In order to cool the gas leaving the exit plenum down to a temperature compatible with the turboblower, a 2" tube in 12" shell heat exchanger connected in parallel with a ball valve controlled 4" bypass line was installed upstream of the turboblower inlet. Boiling water with the steam pressure controlled to 25 psig was found adequate for the various experiments so far completed. The liquid level in the shell was automatically controlled so as to maintain a level above the top of the center 2" pipe. The shell was designed so as to withstand pressures as high as 200 psig,

thus permitting a much larger cooling capacity than was actually found necessary.

All portions of the piping system were insulated with a 4" thickness of magnesia insulation. An approximately 2" thick blanket of magnesia insulation was wrapped around the turboblower shell as well.

2.2.5 PROBE HOLDERS AND ASSOCIATED SEALS

In Figure 9 the location of the heating elements, instrumentation probes, static pressure taps, and the trip plate are shown. Also, a number of the important dimensions are shown in this figure.

Each of the probes used to obtain the radial profiles (TC, PT, and OP) was installed in a probe holder assembly. The outer cylindrical housing of this assembly was sealed with a small "Flexitallic" gasket to the test section wall. The assembly itself consisted of a barrel statically sealed to the probe with a compression fitting which was in turn sealed, with two Viton A o-rings in tandem, to the cylindrical housing. The o-rings provided a sliding seal. The cross section of the cylindrical housing was significantly reduced in the immediate vicinity of the test section wall. At that point a guard heater was installed in order to minimize the loss of heat from the test section wall by conduction to the ambient surroundings and to assist in maintaining a uniform temperature on the inside of the test section wall at the probe entry point. The temperature of the cylindrical housing near its flanged end at the test section wall was monitored with a thermocouple. The electrical power to the electrical resistance-type guard heater was manually adjusted so that this temperature was comparable to that measured at the outside wall of the test section. Farther back from the guard heater a small cooling coil was fitted to the outside of the cylindrical housing in order to maintain the temperature in the vicinity of the o-rings at a level which would insure their proper functioning as seals ($< 400^{\circ}F$). Each probe assembly was fitted with a calibrated drive system and displacement gauge sensitive to translations of 0.001". The entire ensemble made it possible to obtain

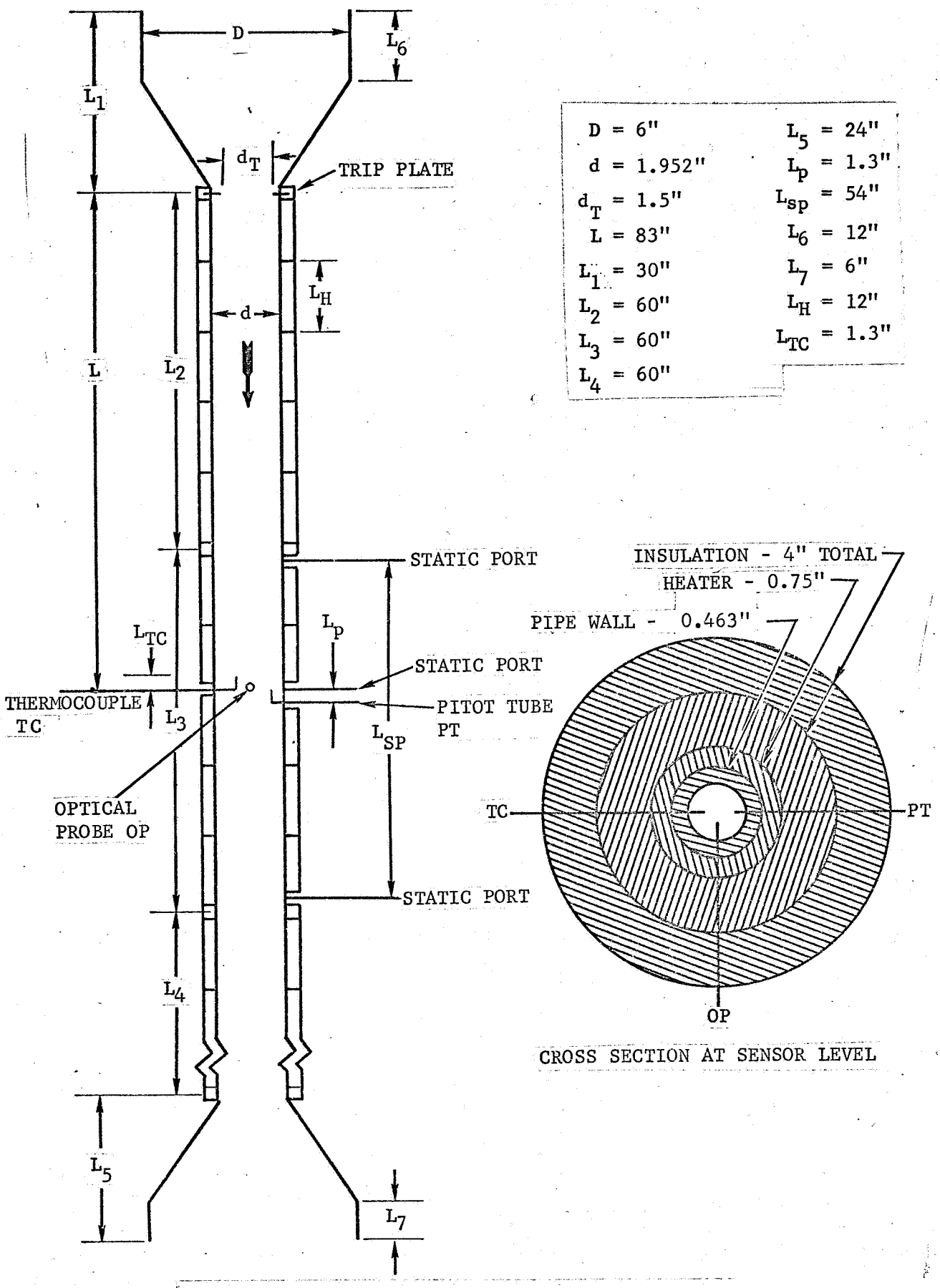

FIGURE 9. TEST SECTION DETAILS AND DIMENSIONS

reasonable radial profile data under quite hostile conditions.

2.3 INSTRUMENTATION

2.3.1 PRESSURE AND PRESSURE DIFFERENCE MEASUREMENTS

Since the vapor pressure of the NO_2 system is such that at 10 atm total pressure the boiling point of liquid N_2O_4-NO_2 is on the order of 80°C, care had to be taken to insure that liquid droplets did not obstruct the pressure lines connected to the system. This was accomplished by connecting each pressure line to a drip pot assembly (18) at a point close to the flow system itself and by guard heating to over 100°C the interconnecting pressure line between the system and the drip pot as well as the drip pot itself. The pressure line connecting the drip pot to the pressure sensor was in each case of considerable length. At the start of each experiment these lines were filled with dry N_2 in order to provide a buffer between the sensor and the drip pot. In no experiment was NO_2 vapor detected at the sensor location. In some cases, erratic pressure difference measurements were thought to be caused by the hold-up of liquid N_2O_4-NO_2 in the pressure lines, possibly at some point between the drip pot and the sensor. When erratic results were being obtained, the simple expedient of purging with N_2 under pressure was used to clear the lines. This usually restored the system to its normal condition.

Total system pressure measurements were made with precision stainless steel bourdon tube gauges. All pressure difference measurements were made with the specially designed nulling-type micromanometer shown in Figure 10. Water was used as the displacement fluid. Displacements were measured to within 0.001". Total displacements of up to 8 inches could be measured with this device. Both fine and coarse translations of the sloping glass capillary tube could be made. Accurate measurement of small pressure differences was required for the determination of mass flow rates with the aid of the orifice plate installed downstream of the blower outlet, for the determination of the static pressure drop down the test section (static pressure holes in the test section wall were 0.0135" in diameter), and for

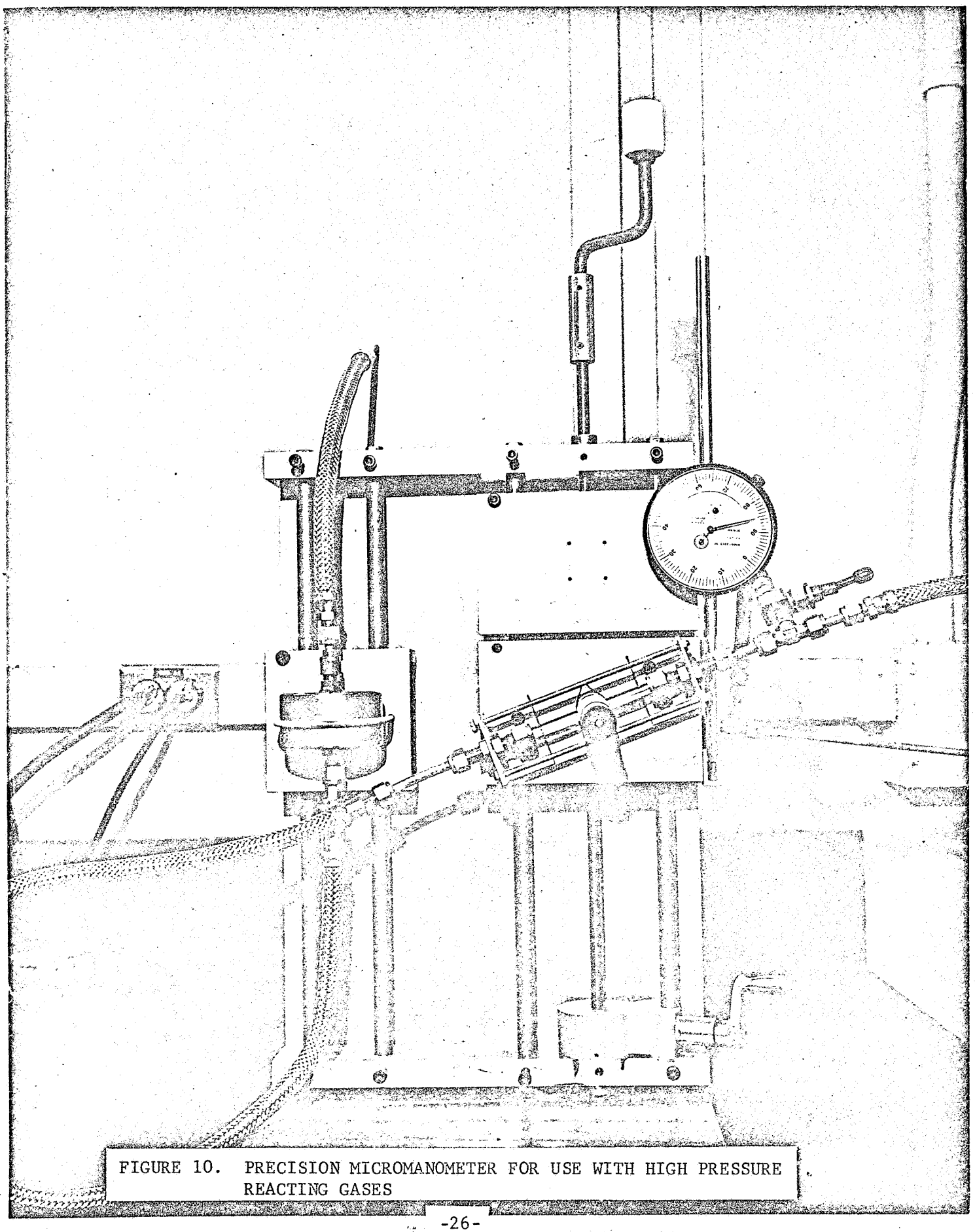

FIGURE 10. PRECISION MICROMANOMETER FOR USE WITH HIGH PRESSURE REACTING GASES

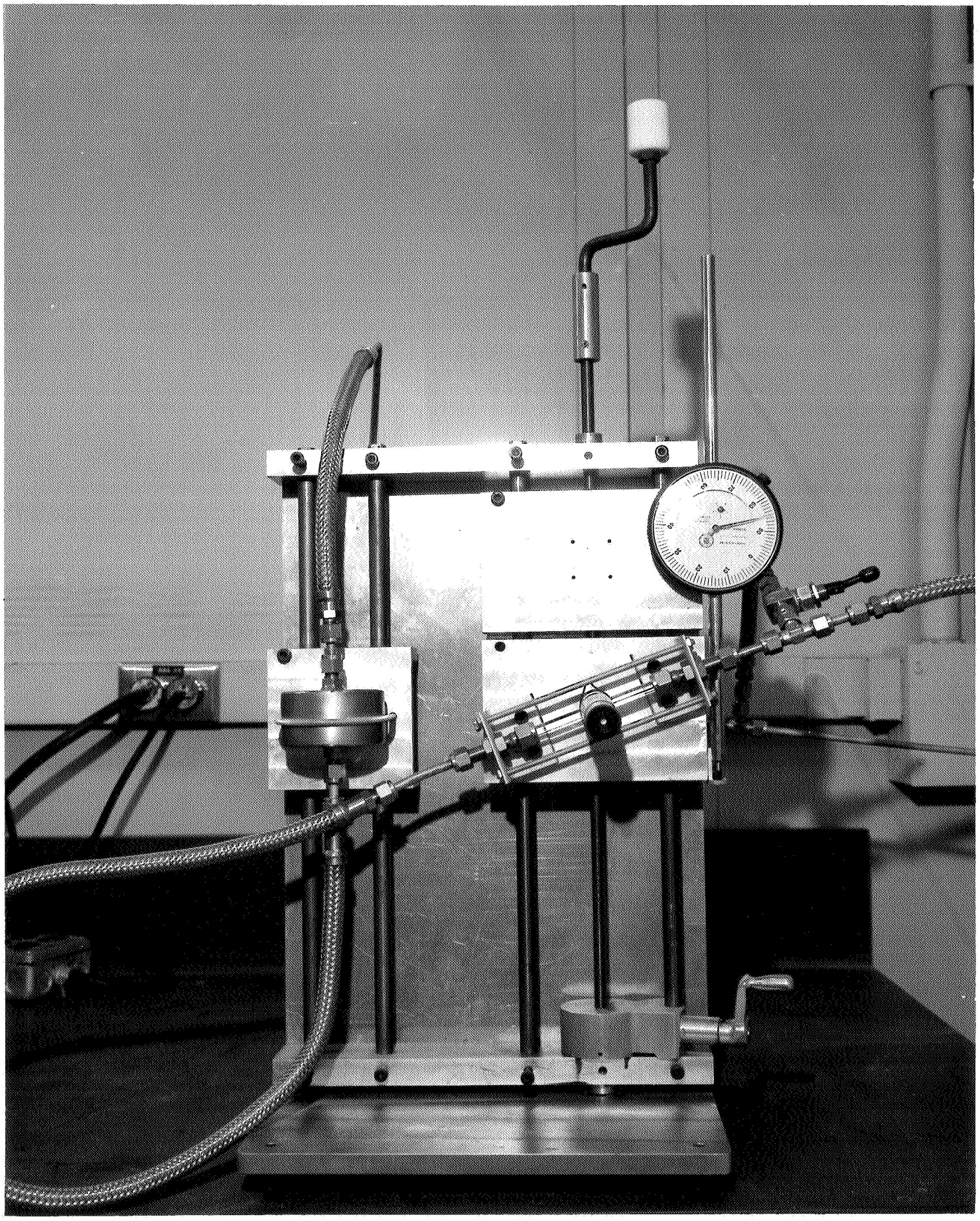

the determination of the local velocity in the test section with the aid of the total head tube and appropriately located static pressure tap (see Figure 9).

The orifice plate was of standard square edge design (orifice flange with orifice diameter of 2.15" — flange installed in a nominal 3" schedule 40 pipe). The sensing end of the total head tube was constructed of standard stainless steel hypodermic tubing (outside diameter $\simeq$ 0.050" or 0.065", internal diameter $\simeq$ 0.034" or 0.040", respectively).

2.3.2 MEAN TEMPERATURE AND HEAT FLUX MEASUREMENTS

The time-average radial temperature profiles were measured with a butt welded exposed junction of Chromel-Alumel thermocouple wire. The wires were sealed in a stainless steel support tube filled with magnesia and swaged to effect a pressure tight seal around each of the wires. In some of the latter experiments, the fast response thermocouple probe (see Section 2.3.3) was also used for time-average profile measurements. It consisted of an exposed junction of Platinum/Platinum-10% Rhodium. In both cases the junction was in the shape of a sphere several times larger than the supporting wire diameter. The sizes for the Chromel-Alumel couple were: sheath outside diameter = 0.062", wire diameter = 0.011", and junction diameter = 0.020". All temperatures were measured with a precision potentiometer (Leeds and Northrup Model K-3). The overall accuracy of the time-average temperature measurements was estimated to be within 0.1°F.

Wall heat fluxes were determined by measuring the electrical power dissipated in a 1 foot long heating element (consisting of two semi-cylindrical halves) located just upstream of the probe insertion position in the center test section (see Figure 9). Longitudinal losses in the test section wall were accounted for with the aid of axial back wall temperature measurements via spot-welded thermocouples (leads from the junction were "guard heated" by being aligned with and attached to the back wall for several inches away from the junction). Losses through the four inch

thickness of magnesia insulation were accounted for by measuring the temperature at two different depths in the insulation. Inside wall temperatures at the steady state were determined by calculation knowing the net heat flux into the test section wall, the back wall temperature, the wall thickness, and the dependence on temperature of the thermal conductivity of the wall material.. An indication of how the total power consumed by one heating element varied with time during the course of an experiment is shown in Figure 11. Note that approximately four hours were required for the heat flux to settle down to a reasonably steady value. Considering the uncertainty associated with the corrections, we estimate that the heat fluxes were known to within 10% (at best).

2.3.3 THE FAST RESPONSE THERMOCOUPLE PROBE AND ASSOCIATED ELECTRONICS

The sensor selected for use in measuring the fluctuating temperature and its dependence on frequency in the high temperature reacting NO_2 system was a fast response thermocouple based on the design of Sesonske and coworkers (39)(40). The form used in this investigation is shown in Figure 12. The junction size is expected to be small enough so that its frequency response should be good out to 10 k Hz (39). The fluctuating dc signal from the thermocouple probe was amplified by a low noise amplifier modified so as to have a gain of 12,600:1 (41)(42). The output of the amplifier was independent of frequency in the range 10 Hz to 1 k Hz. The narrow band noise was measured over this frequency range and was found to be on the order of 0.01 to 0.05 microvolts. Input signal levels with the corrosion resistant Platinum/Platinum-10% Rhodium thermocouple were on the order of 20 to > 100 microvolts. The data from the probe/amplifier system was processed according to the methods outlined by Rust (43). The electronic instruments used to carry out the data processing are shown in Figure 13. A band width calibration for the wave analyzer used in obtaining the spectral information is shown in Figure 14. A true RMS meter was used to obtain the wide band, or total, rms fluctuating temperature. The arrangement of the electronic instrumentation for processing the data is similar to that used in conjunction with the

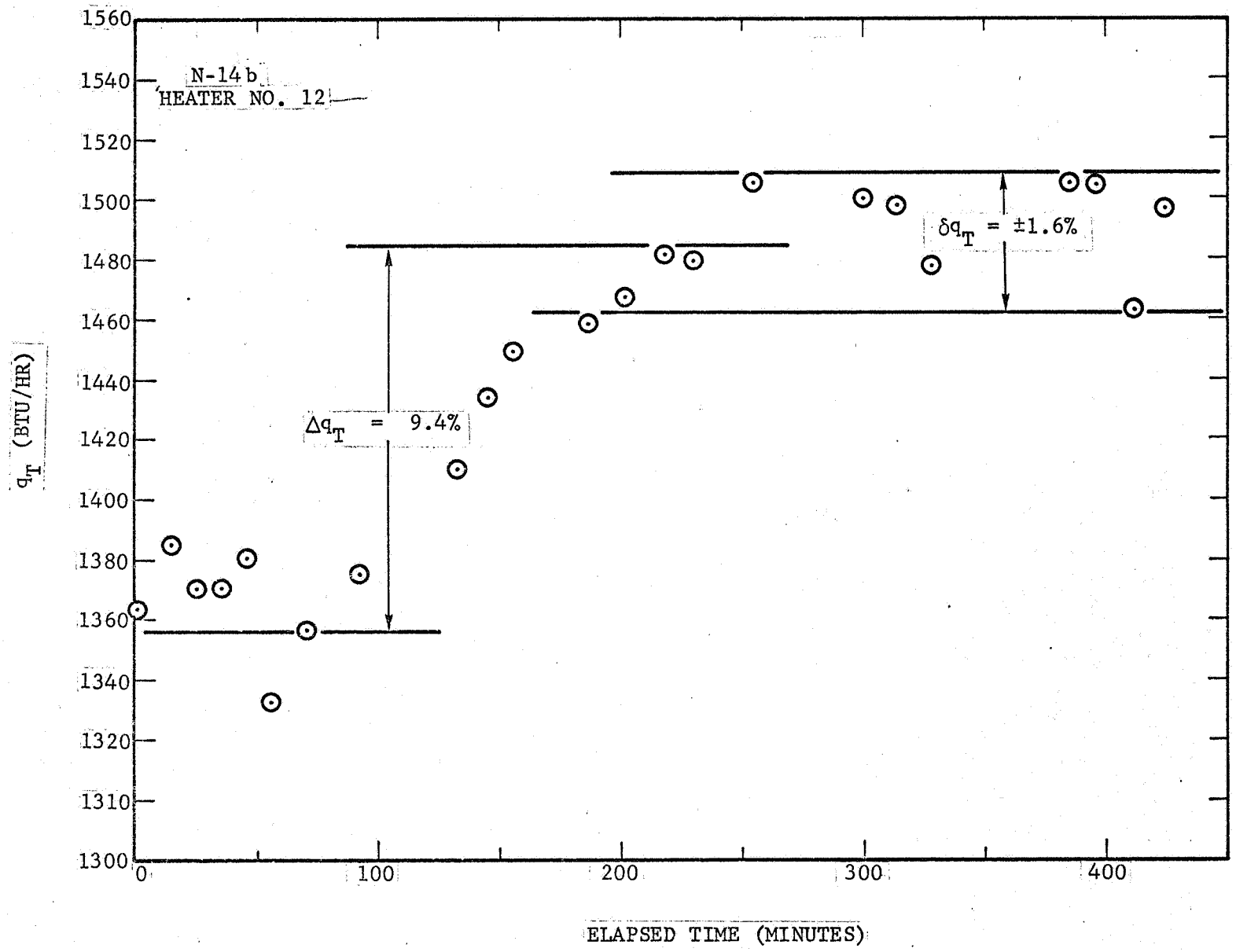

FIGURE 11. VARIATION WITH TIME OF THE TOTAL ELECTRICAL POWER REQUIRED BY ONE HEATING ELEMENT ON THE TEST SECTION (1 FOOT LENGTH)

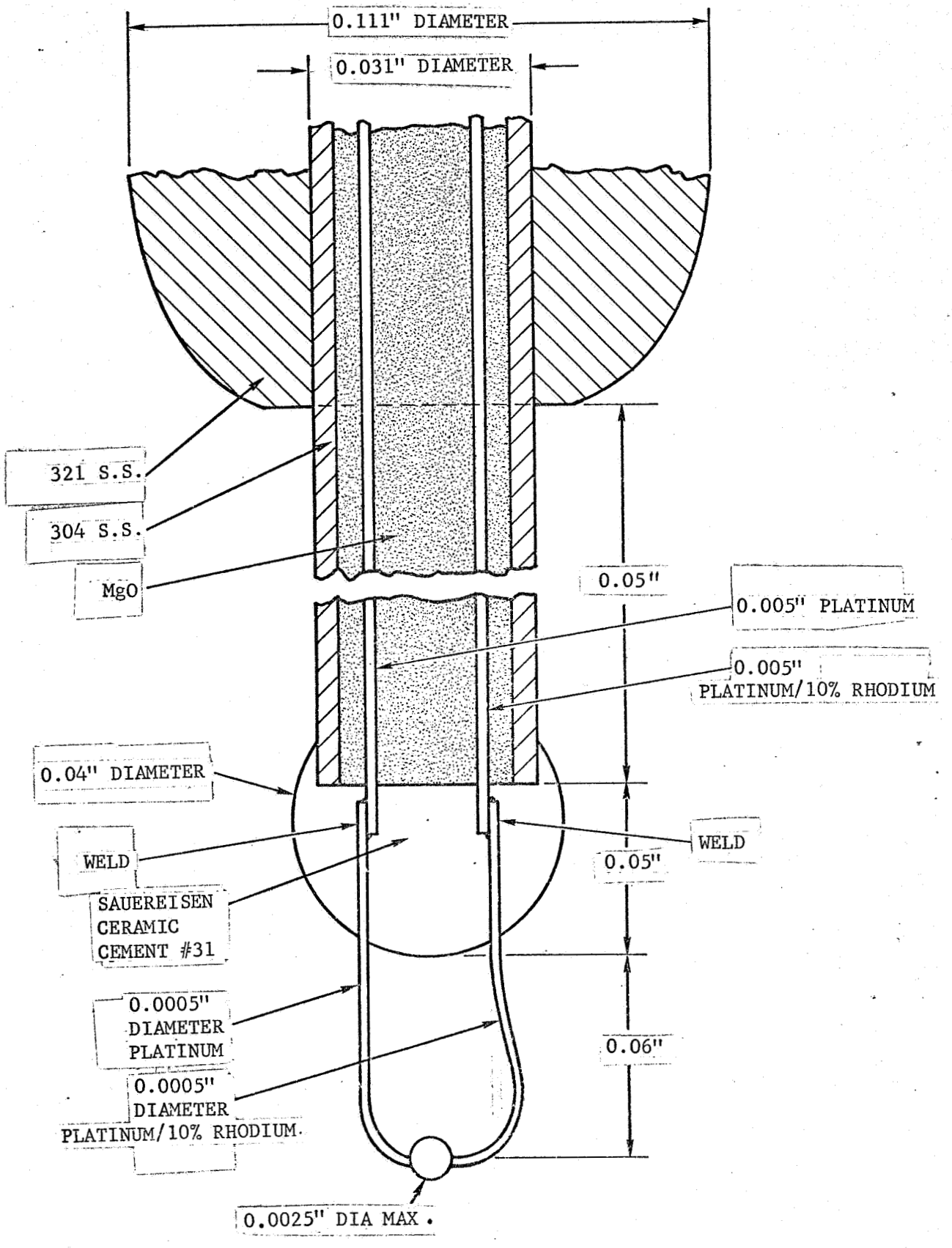

FIGURE 12. SENSING END - FAST RESPONSE THERMOCOUPLE PROBE

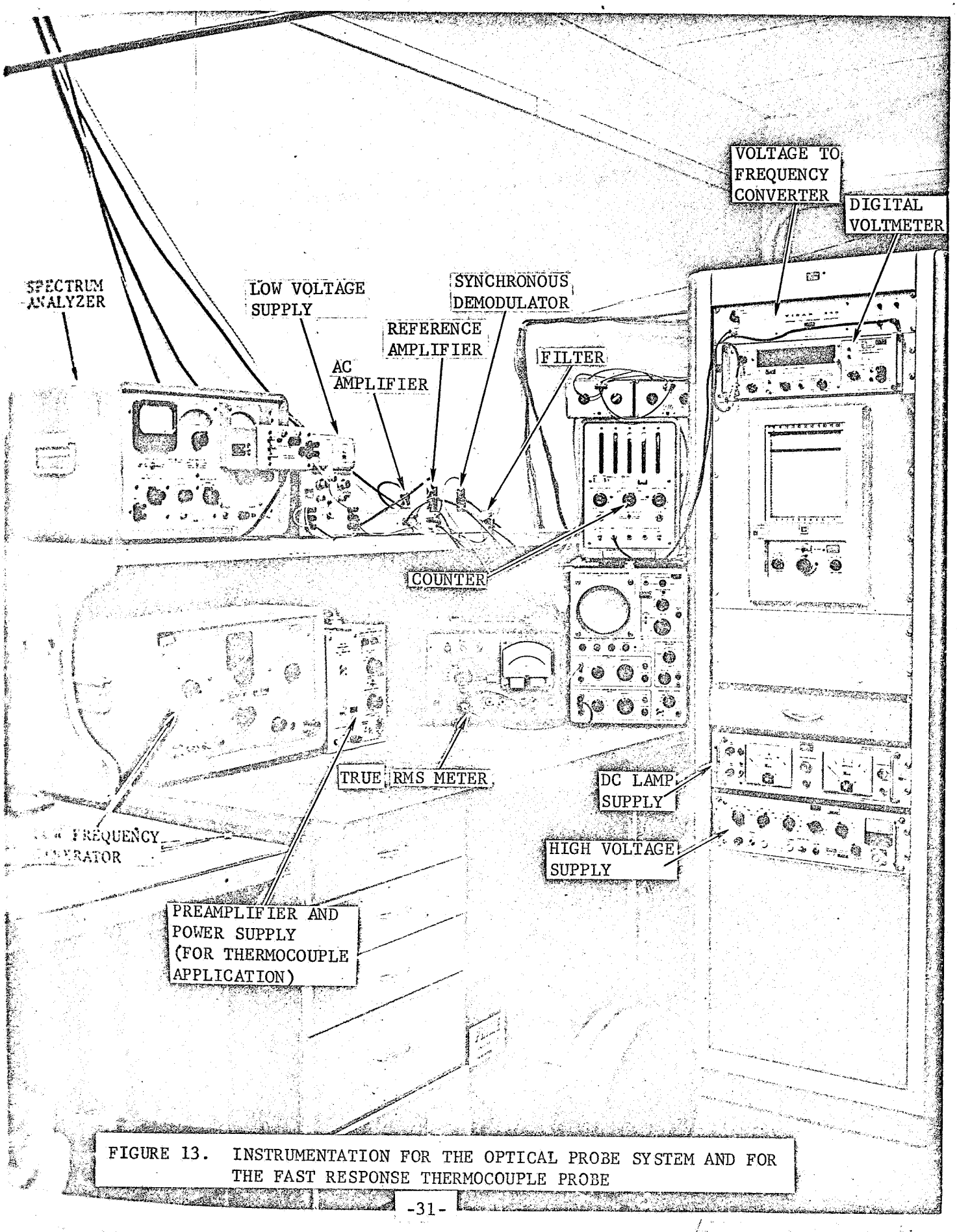

FIGURE 13. INSTRUMENTATION FOR THE OPTICAL PROBE SYSTEM AND FOR THE FAST RESPONSE THERMOCOUPLE PROBE

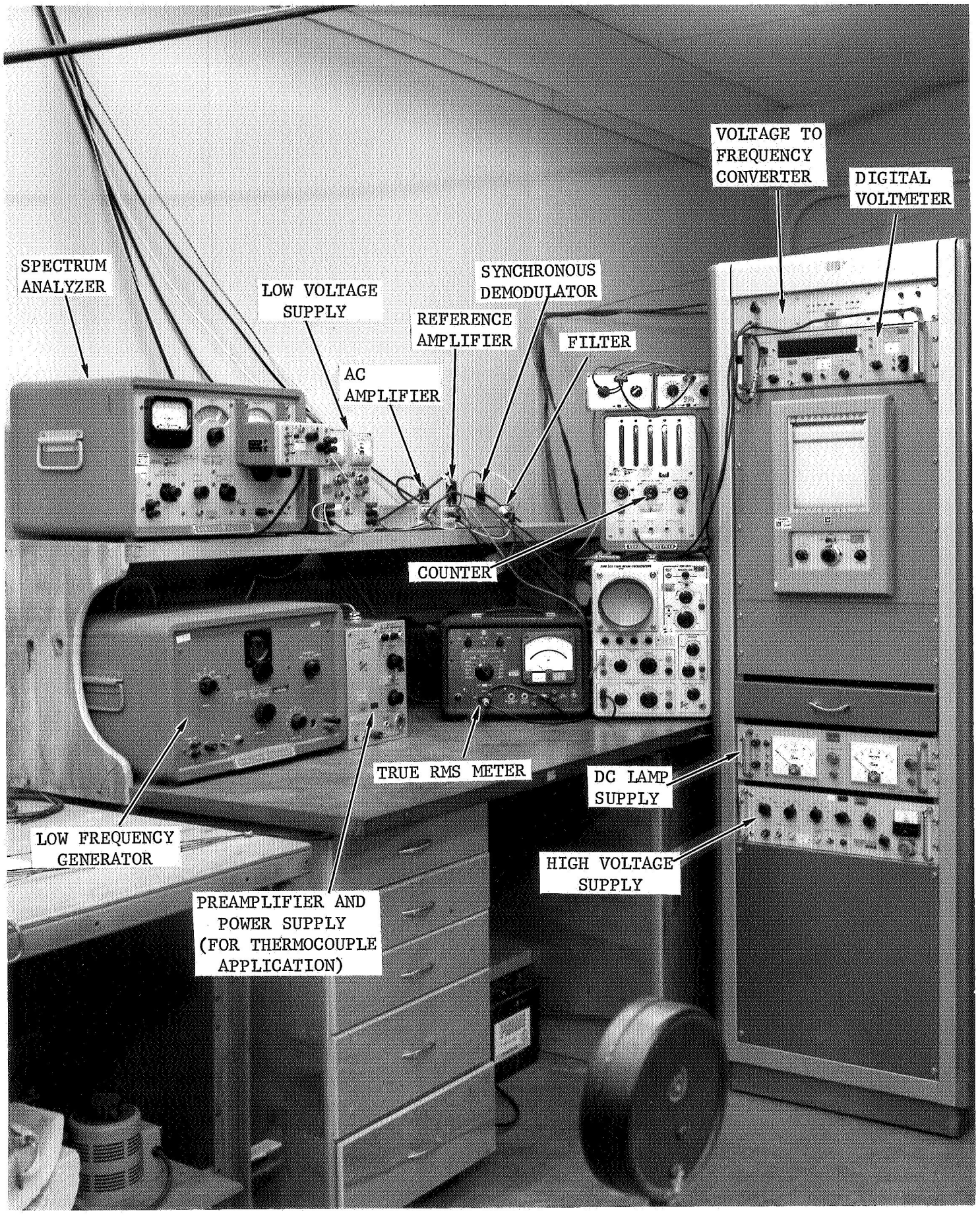
VOLTAGE TO FREQUENCY CONVERTER
DIGITAL VOLTMETER
SPECTRUM ANALYZER
LOW VOLTAGE SUPPLY
SYNCHRONOUS DEMODULATOR
REFERENCE AMPLIFIER
FILTER
AC AMPLIFIER
COUNTER
TRUE RMS METER
DC LAMP SUPPLY
LOW FREQUENCY GENERATOR
HIGH VOLTAGE SUPPLY
PREAMPLIFIER AND POWER SUPPLY (FOR THERMOCOUPLE APPLICATION)

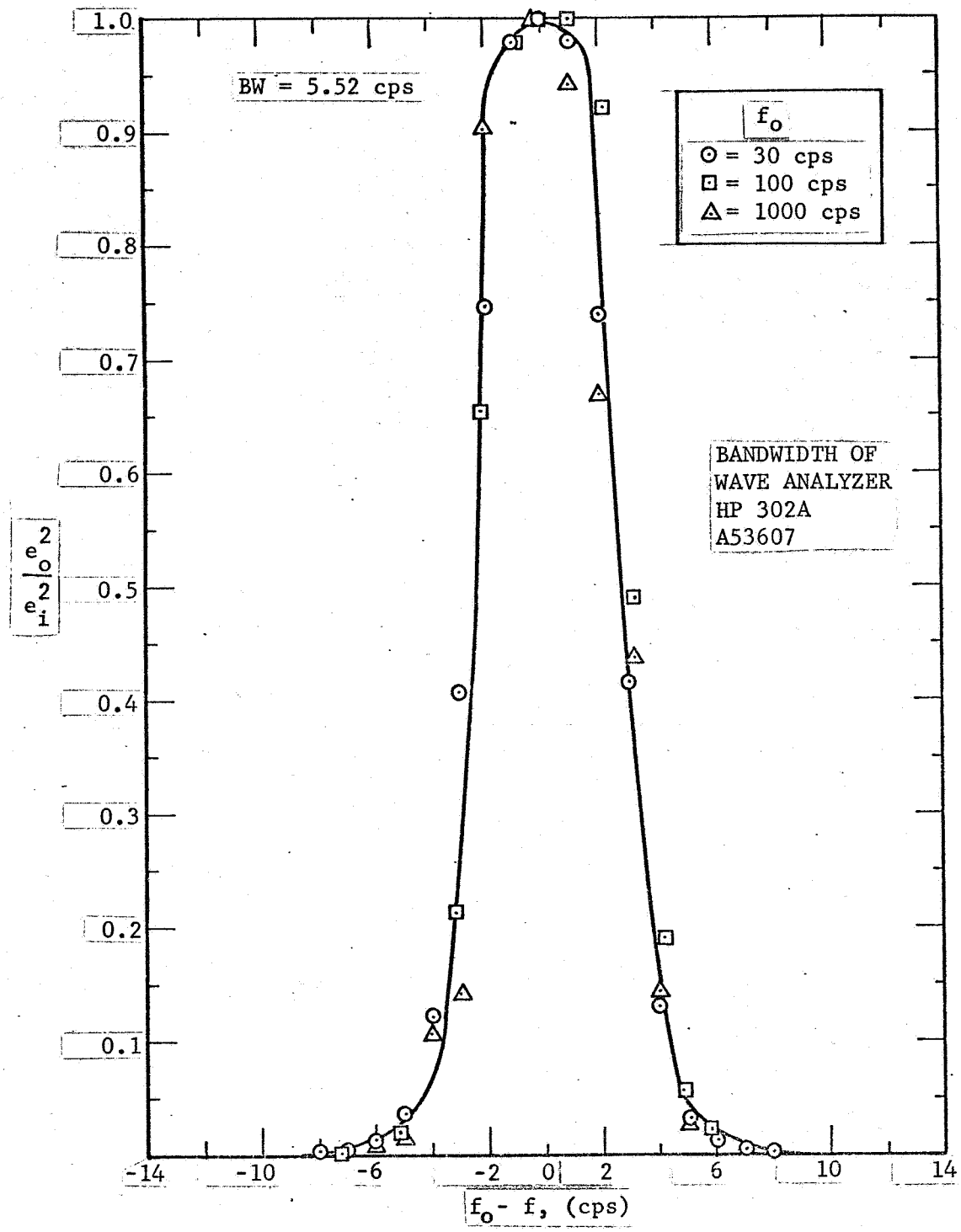

FIGURE 14. BANDWIDTH CALIBRATION OF THE WAVE ANALYZER

optical probe system (see Section 2.3.4).

2.3.4 THE OPTICAL PROBE SYSTEM FOR MEASUREMENT OF LOCAL NO_2 CONCENTRATIONS

Lambert-Beers absorption law,

$$\frac{I}{I_o} = \exp\left(- \epsilon_{NO_2} \ell C_{NO_2}\right) \tag{1}$$

was the basis for the design of a light absorption system capable of measuring the local NO_2 concentration in the high temperature flow system in which the total gas pressure could reach values as high as 150 psig.*

An optical probe system used for making local transmittance measurements in dye and water flows at $\sim 25^{o}C$ and 1 atm has been described by Brodkey and coworkers (44)(45). The system and probe design developed for use in this investigation was significantly different than that used by Brodkey and coworkers. It is a dual beam (sample and reference), chopped system with high signal to noise ratio characteristics and good stability.

The optical system used in this investigation is shown in Figures 15 and 16. Radiant energy emitted by the tungsten iodine light source (A) is divided into two separate channels, reference and sample, by the cubic beamsplitter (B). After traversing the two optical paths, the energy is brought to a common focus on the face of the photomultiplier tube (I). In order for the PMT to receive both reference and sample signals alternately, a reflective chopper is inserted in the system near the PMT. The chopper alternates passing the sample signal and reflecting the reference signal for equal amounts of time.

The sample channel which contains the optical test probe for the concentration measurements absorbs a significantly larger amount of radiation than the reference channel. Consequently, it requires a greater amount of input radiation if a balance between the two channels is to be obtained at the PMT. The beamsplitter transmits more energy than it reflects; therefore, it is positioned so that the reference channel receives the reflected radiation and the sample channel receives the trans-

---

*$\epsilon_{NO} = \epsilon_{O_2} \simeq 0$ for $3000 < \lambda < 5000$ angstroms.

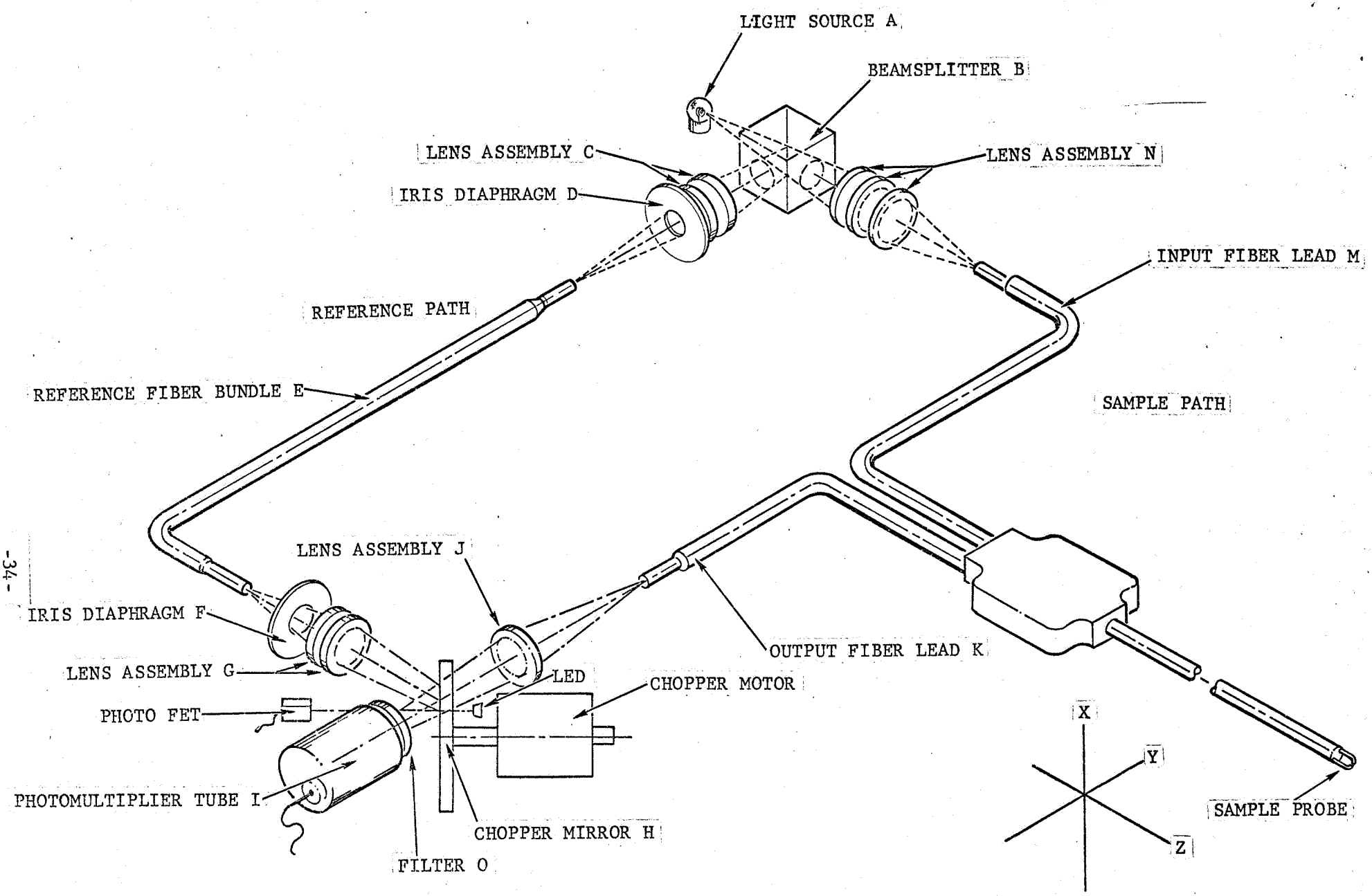

FIGURE 15. OPTICAL SYSTEM SCHEMATIC

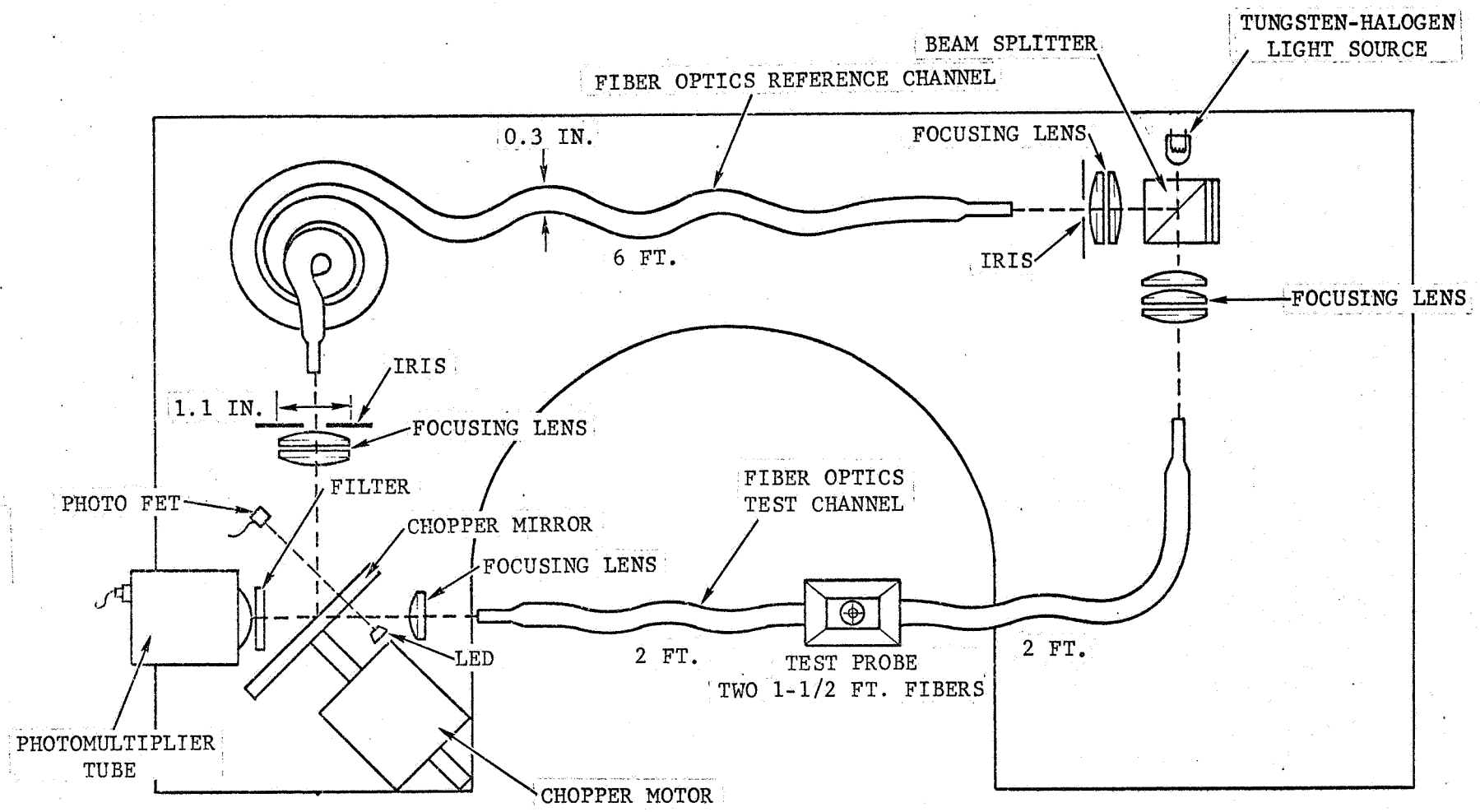

FIGURE 16. OPTICAL SYSTEM SCHEMATIC

mitted radiation.

The optical test probe consists of glass fiber bundles, plastic fibers, tapered light pipes, and plastic fiber bundles used as input and output optical leads. The overall configuration of the optical probe itself is shown in Figure 17. The probe tip region is shown in Figure 18. The gap between the optical fiber bundles was ~ 0.010" (the exact gap was different for each probe made). The optical fiber bundle diameter was 0.025". The bundle pair was contained in 0.25" O.D. 316 stainless steel tube ~ 12" long. The transition from the stiff fiber bundles containing the high temperature glass to the flexible fiber lines used to connect the probe to the optics was made with the plastic fibers and tapered light pipes in the rectangular housing shown in Figure 17. Ceramic cement was used to fix the gap width at the sensing end (Figure 18). It was found necessary to thermally condition the probe sensing end at high temperature in order to obtain stable performance characteristics.

In addition to the apparatus discussed above, the sample channel also contains two lens assemblies, (J) and (N). Lens assembly (N) focuses the radiation from the source at the end of the input optical lead, and lens assembly (J) focuses the radiation emerging from the output fiber lead on the face of the PMT. The lens assemblies (J) and (N) have focal lengths of 2.3 inches and 1.3 inches, respectively.

The reference channel is similar to the sample channel, except for the addition of two iris disphragms and the lack of an optical probe. The iris disphragms are used to balance the two signals by controlling the amount of light passing through the reference channel.

To enhance the performance of the electronic system, an even level of illumination was maintained at the surface of the PMT by forming nearly identical images at the PMT face. Since the image of the sample channel was formed with a fiber bundle end as the object, a fiber bundle (E) has been used in the reference channel. The fiber bundle has the same effective 1/8 inch diameter as the input-output leads of the optical probe and has a

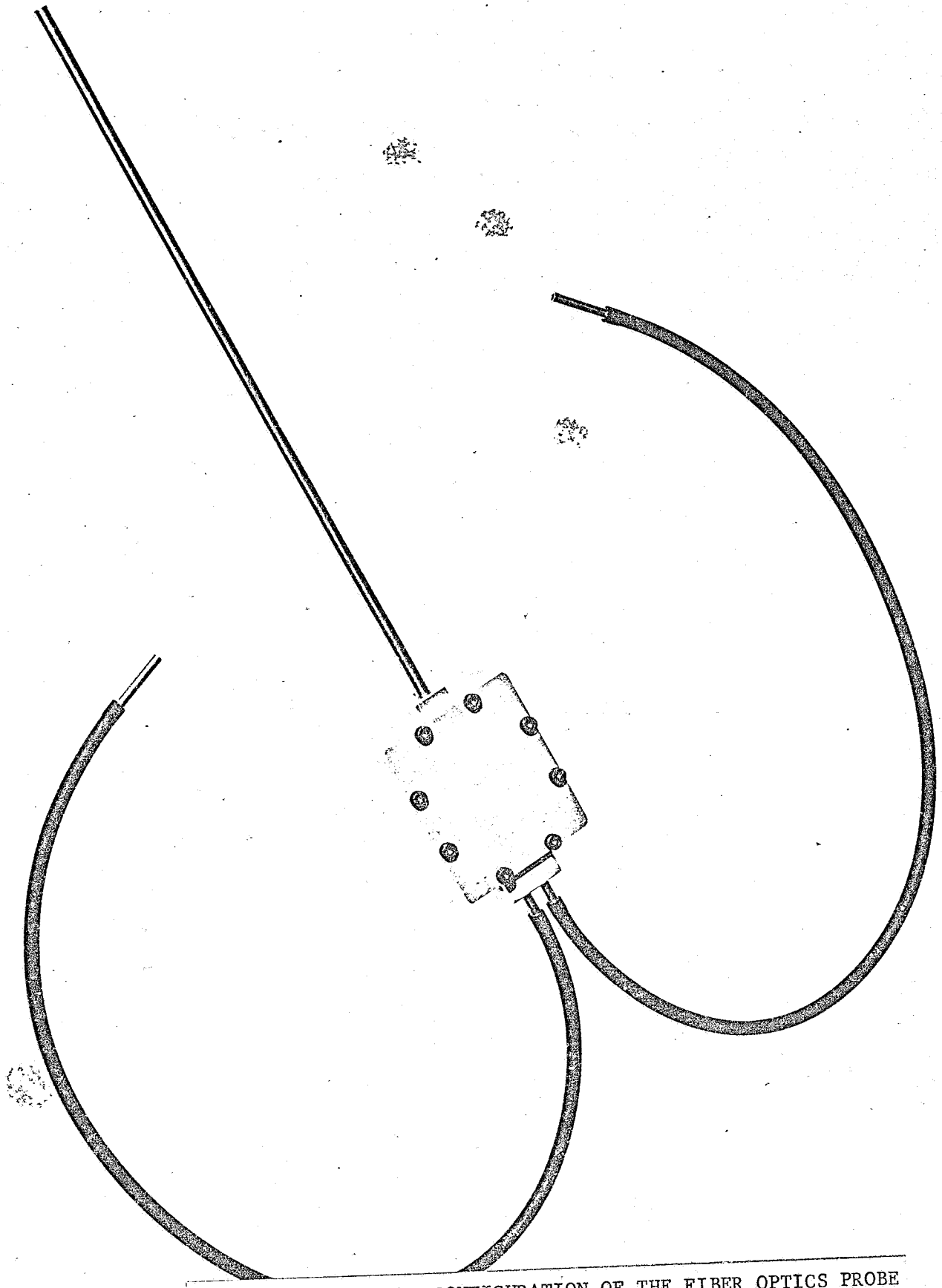

FIGURE 17. OVERALL CONFIGURATION OF THE FIBER OPTICS PROBE (¼" IN OUTSIDE DIAMETER x ~ 12" LONG)

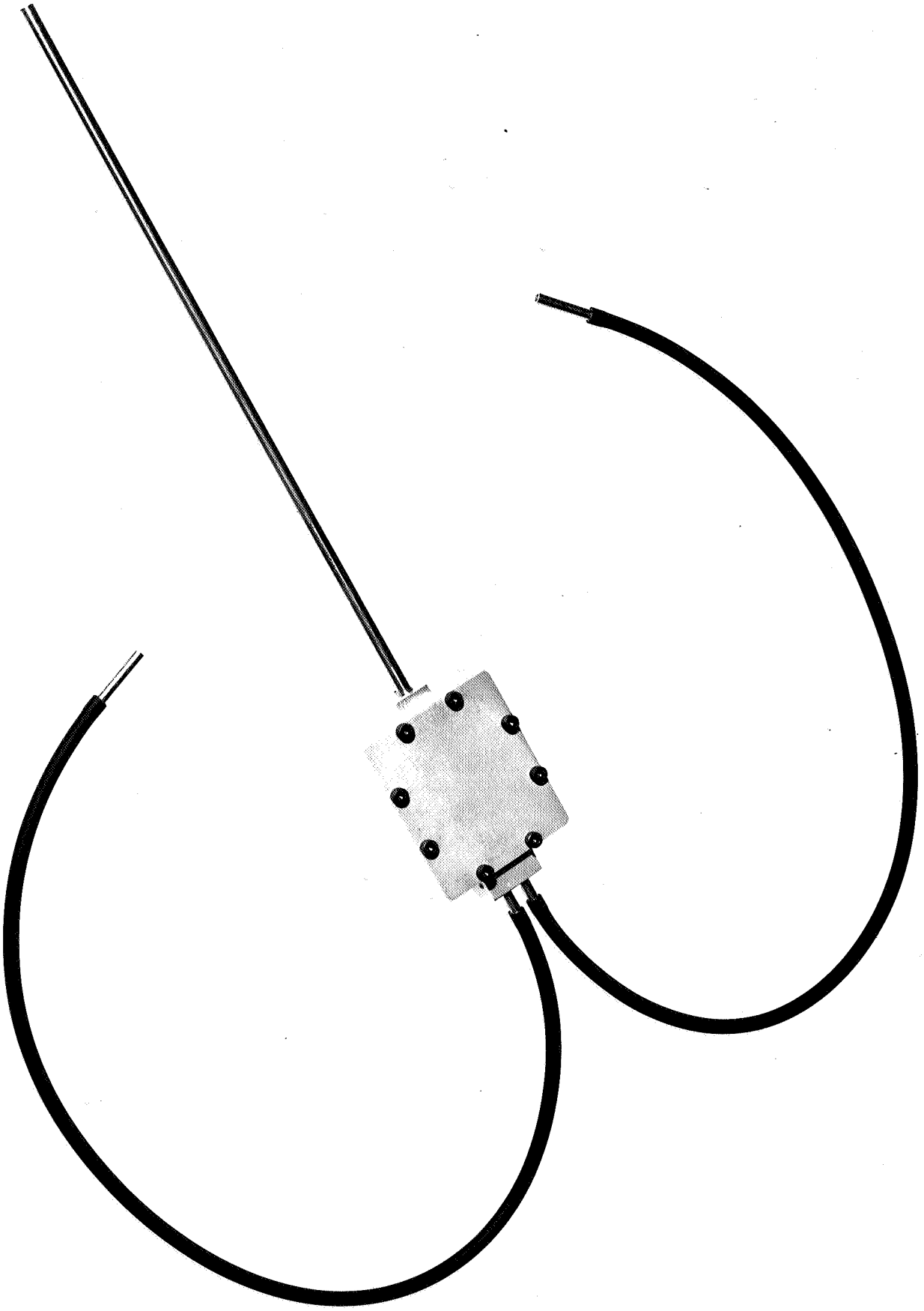

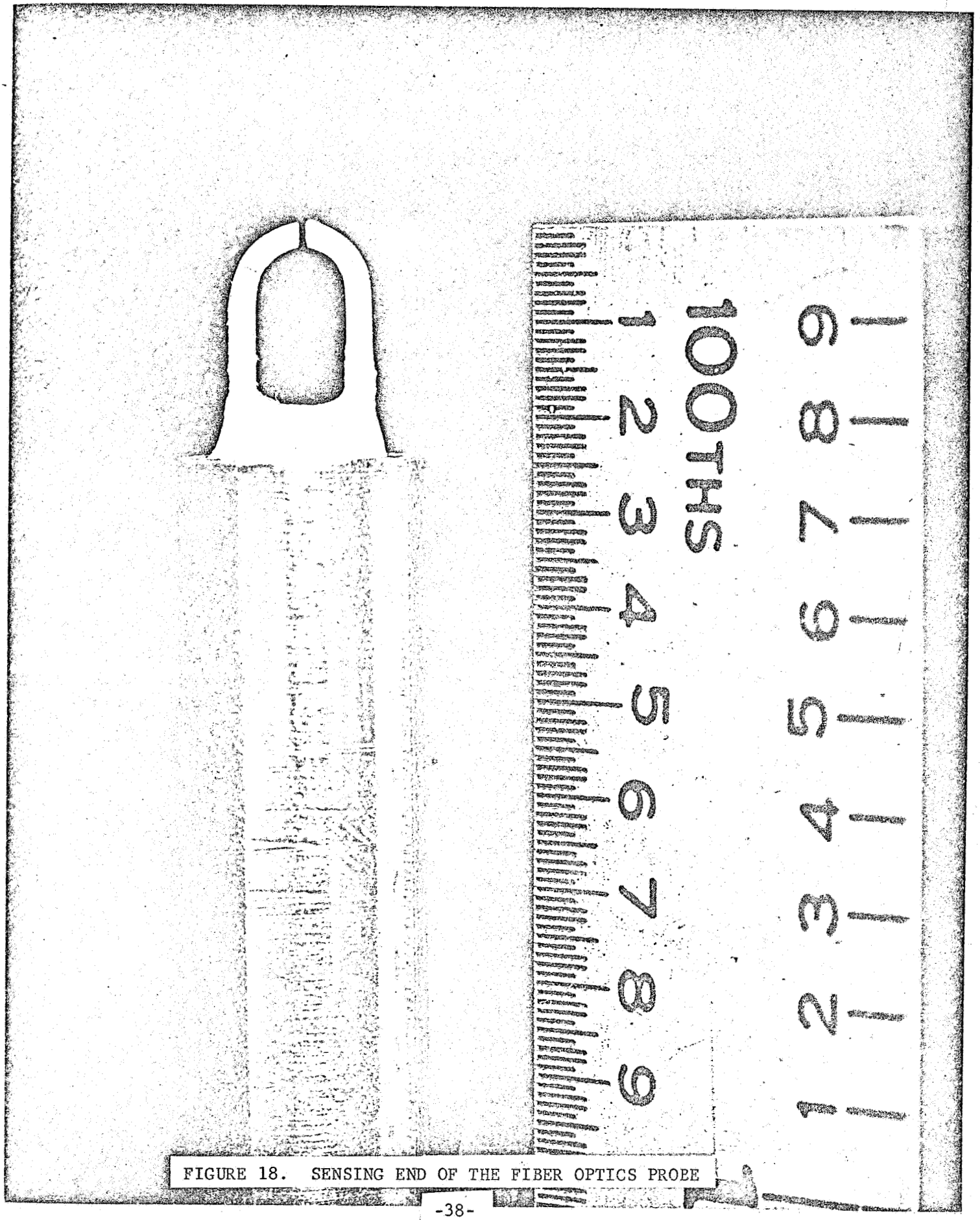

FIGURE 18. SENSING END OF THE FIBER OPTICS PROBE

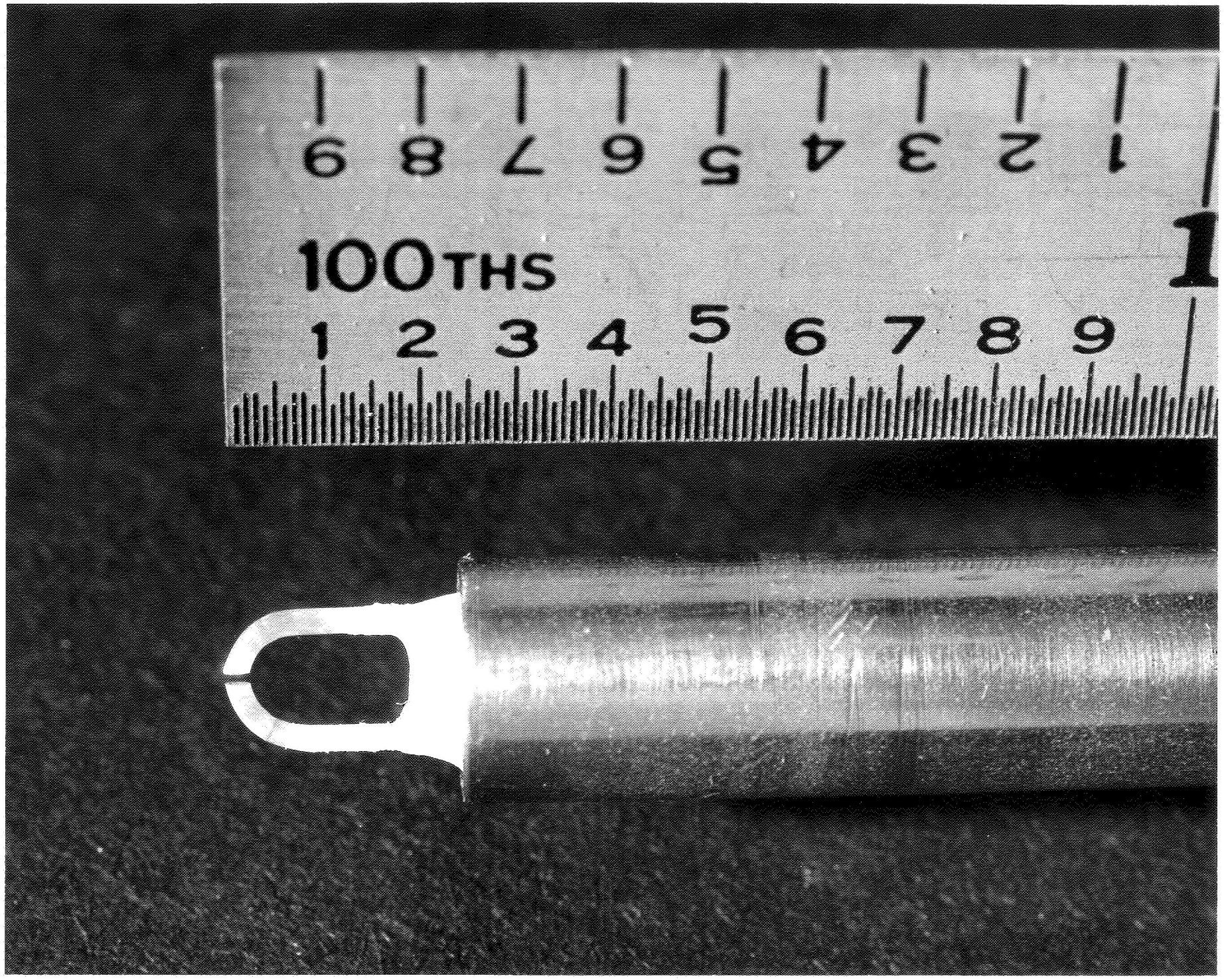
100THS

length of 6 feet, approximately the same as the path length of the probe with leads (K) and (M) attached.

The lens assembly (C) focuses the energy of the source onto the end of the fiber bundle. The assembly consists of two single convex lenses with an effective focal length of 2.7 inches.

After passing through the fiber bundle, the energy is focused on the face of the PMT by means of lens assembly (G) which also has an effective focal length of 2.7 inches.

In addition to the two channels, a light emitting diode (LED) is used in combination with a field effect transistor and chopper for synchronous demodulation. An optical filter, located in front of the photomultiplier, eliminates extraneous LED radiation from reaching it. The filter also shapes the spectral composition of the light striking the photomultiplier tube.

The spectral characteristics of the photomultiplier tube and the filter are shown in Figure 19. The associated electronics layout is shown in Figure 20.* With the system so arranged the signal to noise ratio of the entire system was on the order of 250:1 which was quite adequate for the measurements of both the time-average and fluctuating concentrations. The electronic instruments used with the optical probe are shown assembled in Figure 13.**

Measurements of the extinction coefficient $\epsilon_{NO_2}(\lambda,T)$ were made with a pair of 0.25" quartz rods in place of the optical fiber probe. The measurements were made with NO_2 contained in a static reactor consisting of a 1 foot long section of the same pipe material used in the test section. In Figure 21, the optical housing system is shown with the light-tight cover plates removed. Liquid N_2O_4-NO_2 was vaporized into the

---

*The filtered output of the synchronous demodulator was directly proportional to $\overline{E}_o-\overline{E}$, the time-average voltage difference corresponding to the reference and sample beams, respectively.

**Neutral density filters were used in the transmittance calibration of the system.

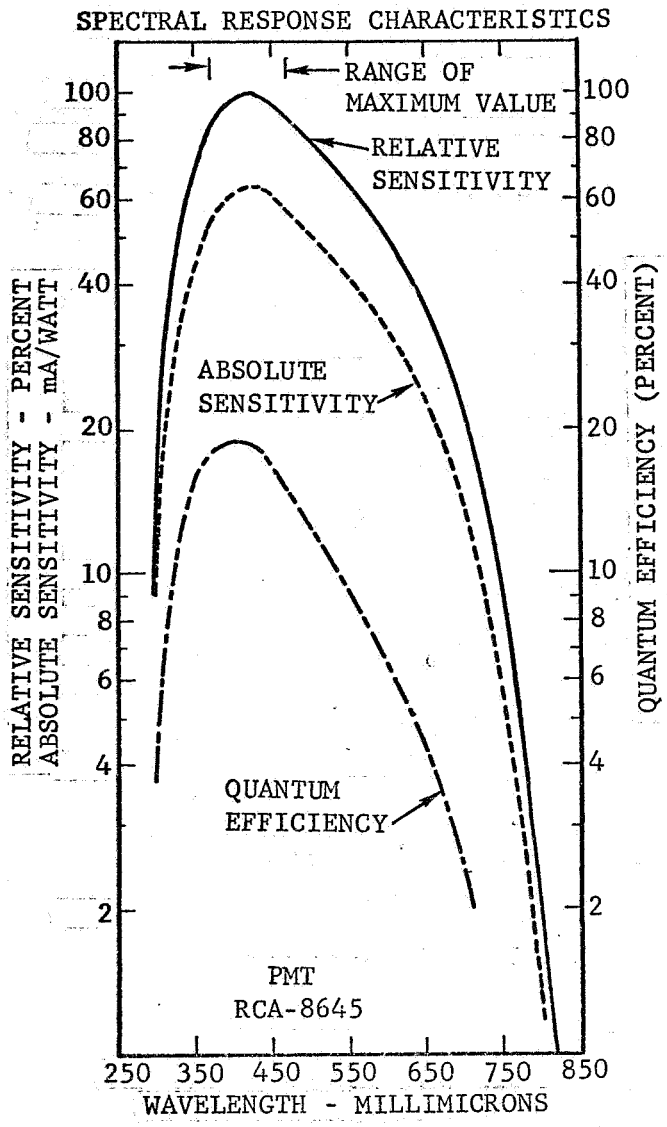

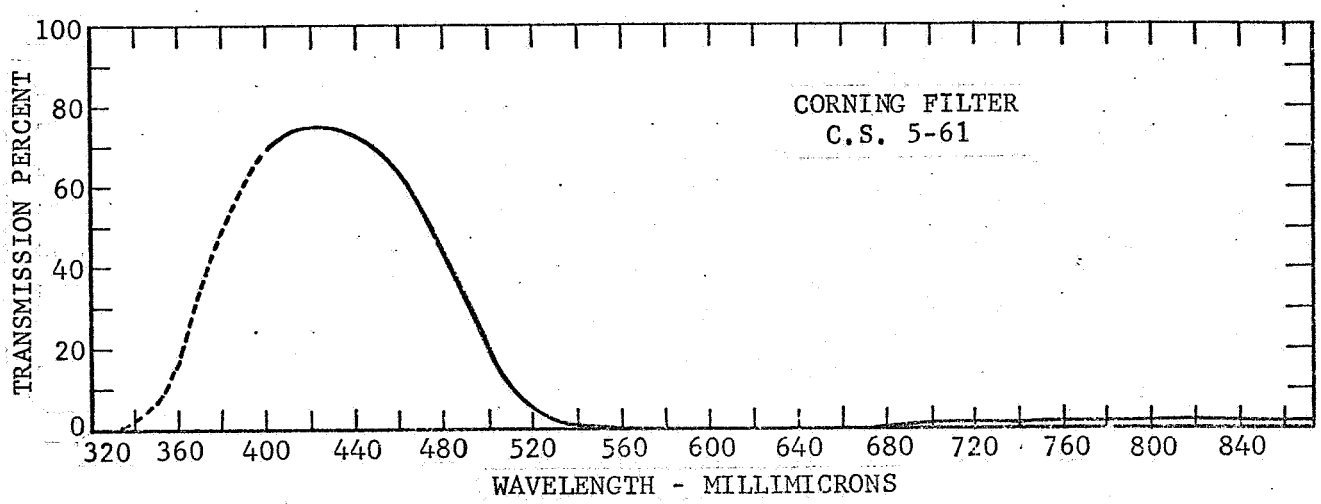

FIGURE 19. CHARACTERISTIC SPECTRAL CURVES OF THE PHOTOMULTIPLIER TUBE AND THE FILTER

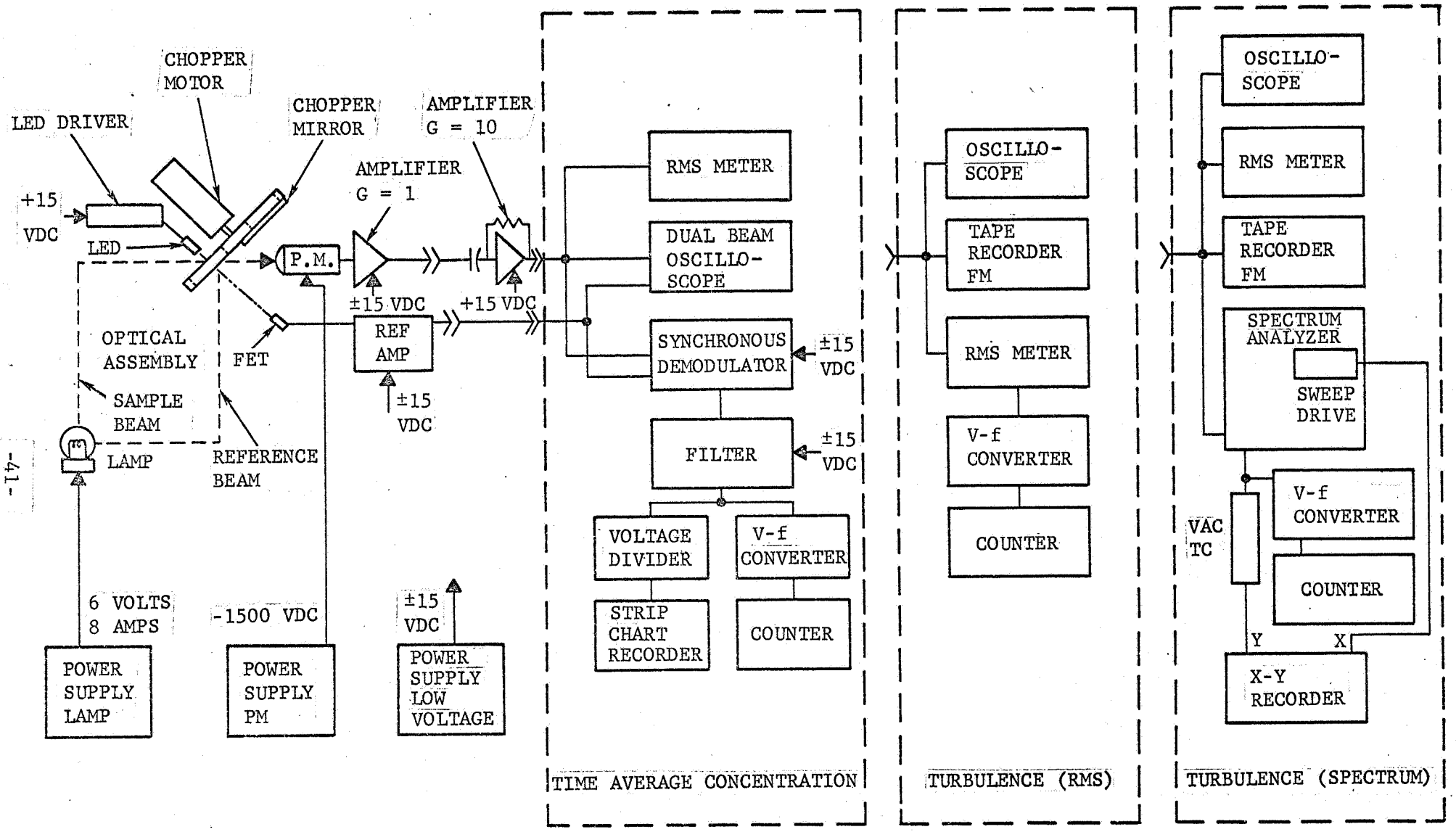

FIGURE 20. SCHEMATIC DIAGRAM OF ELECTRONIC SYSTEM USED FOR THE TIME AVERAGE AND FLUCTUATING CONCENTRATION MEASUREMENTS

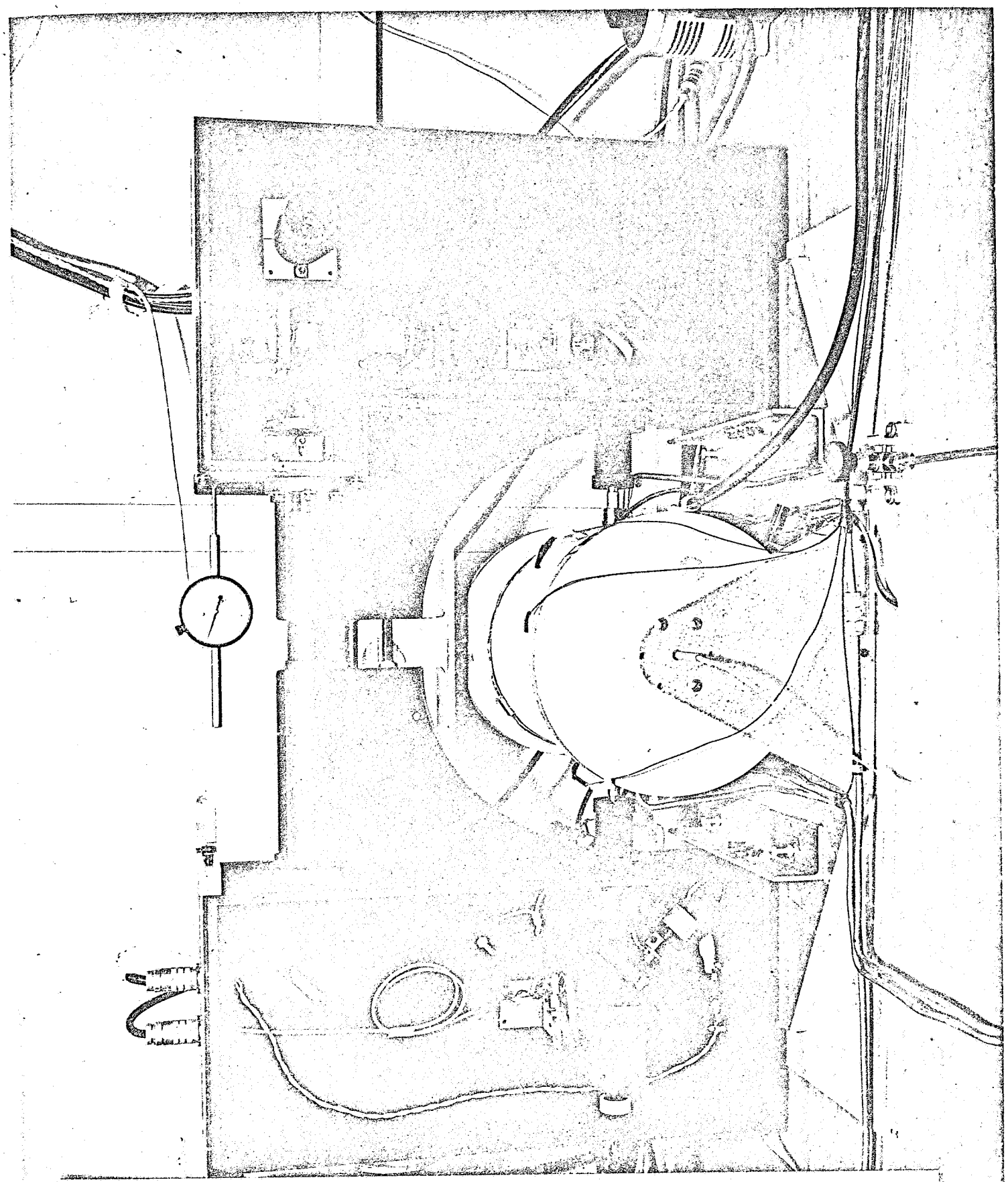

FIGURE 21. OPTICAL PROBE SYSTEM WITH QUARTZ RODS MOUNTED AT THE STATIC REACTOR (COVER PLATES REMOVED IN ORDER TO SHOW SYSTEM COMPONENTS)

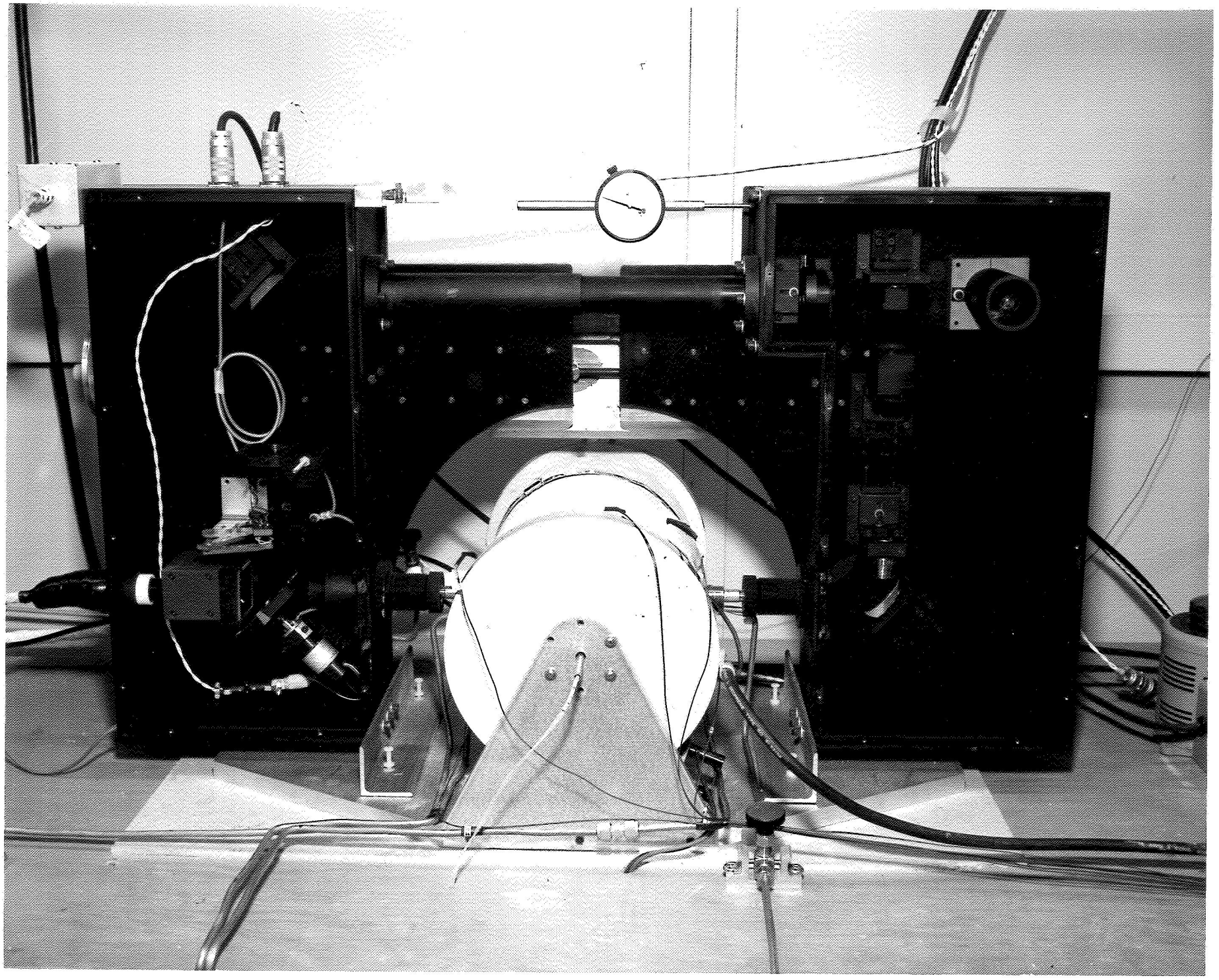

static reactor to the desired pressure. Temperature was controlled with resistance heaters around the outside of the reactor. The distance between the polished and optically flat ends of the quartz rods was measured to 0.001" with a precision displacement gauge. Measurements of transmittance with this system were commenced only after sufficient time had been allowed to elapse (Figure 2) so that chemical equilibrium would be expected to prevail throughout the gas in the static reactor. The 4360 angstrom results* obtained for 2, 5, and 10 atm total pressure and temperatures to $> 900^{\circ}K$ are shown in Figure 22 and Table 3. The resulting extinction coefficient data are shown in Figure 23 compared to the scatter of the data of Schott and Davidson (46)(47). The results are comparable.

2.4 FLOW SYSTEM OPERATION

2.4.1 START-UP

A brief summary of the most important steps involved in the start-up of the flow system is as follows:

1. Checkout of all instruments for proper functioning
2. Evacuation of the system (with a jet ejector) to a pressure of less than 0.1 atm
3. All electrical resistance heaters turned on (temperature of piping system in preheat sections kept $< 1400^{\circ}F$)
4. Guard heaters on probe holders turned on
5. Cooling water to cooling coils on probe holders turned on
6. Pressure lines between the flow system and the micromanometer and the Bourdon gauges filled with dry nitrogen to a pressure slightly exceeding the desired pressure for the experiment
7. Liquid N_2O_4-NO_2 vaporized into system at the rate of ~ 1

*Obtained using a narrow band Bausch and Lomb interference filter.

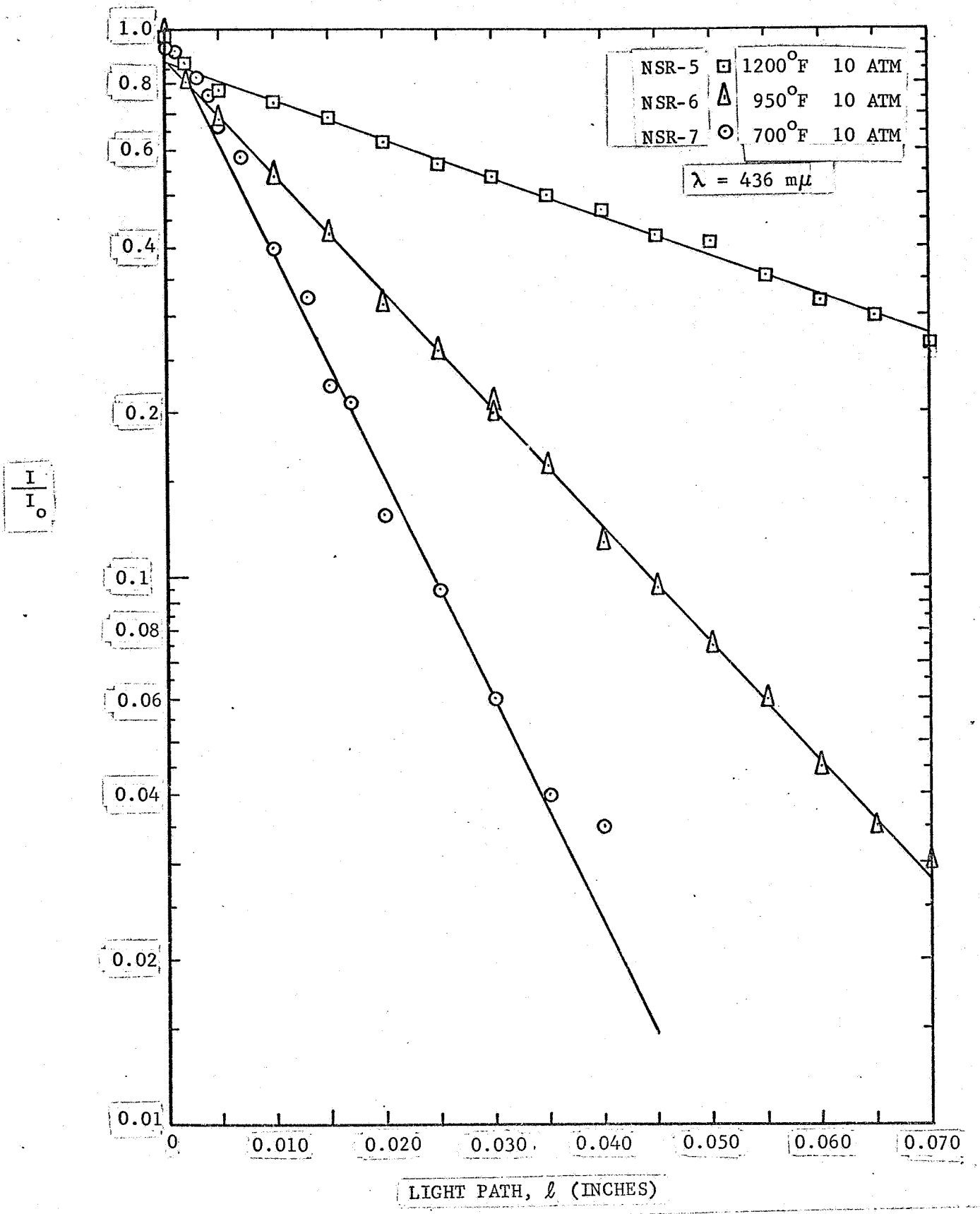

FIGURE 22. NO_2 TRANSMITTANCE DATA AS A FUNCTION OF THE LIGHT PATH LENGTH - MEASUREMENTS MADE UNDER EQUILIBRIUM CONDITIONS IN THE STATIC REACTOR

TABLE 3. EXTINCTION COEFFICIENTS OF NO_2-EQUILIBRIUM CONDITIONS

Experiment Number NSR-	Reactor Temperature T (^oK)	Total Pressure P (atm)	Molar Concentration of NO_2 C_{NO_2} (moles/liter)	Extinction Coefficients† $\epsilon^*_{NO_2}$ (liters/mole cm)	ϵ_{NO_2} (liters/mole cm)	Deviation‡ (percent)
8	644	2	0.024	123	127	-3.15
9	783	2	0.008	126	120	+5.00
10	922	2	0.003	98	114	-14.0
2e	644	5	0.067	111	127	-12.6
3	783	5	0.027	135	120	+12.5
4	922	5	0.009	123	114	+7.89
7	644	10	0.144	111	127	-12.6
6	783	10	0.066	129	120	+7.50
5	922	10	0.024	114	114	0
				Average % Deviation		8.36

† $\epsilon^*_{NO_2}$ = Extinction coefficient measured at a wavelength of 4360 angstroms.

ϵ_{NO_2} = Value of extinction coefficient taken from curve drawn through the data given in Figure 2, p. 18, Ref. 46(at a wavelength of 3660 angstroms).

‡ Percent Deviation = $(\epsilon^*_{NO_2} - \epsilon_{NO_2})/\epsilon_{NO_2}$ (100) .

Average % Deviation = $\sum_n |(\epsilon^*_{NO_2} - \epsilon_{NO_2})(100)|/n\ \epsilon_{NO_2}$.

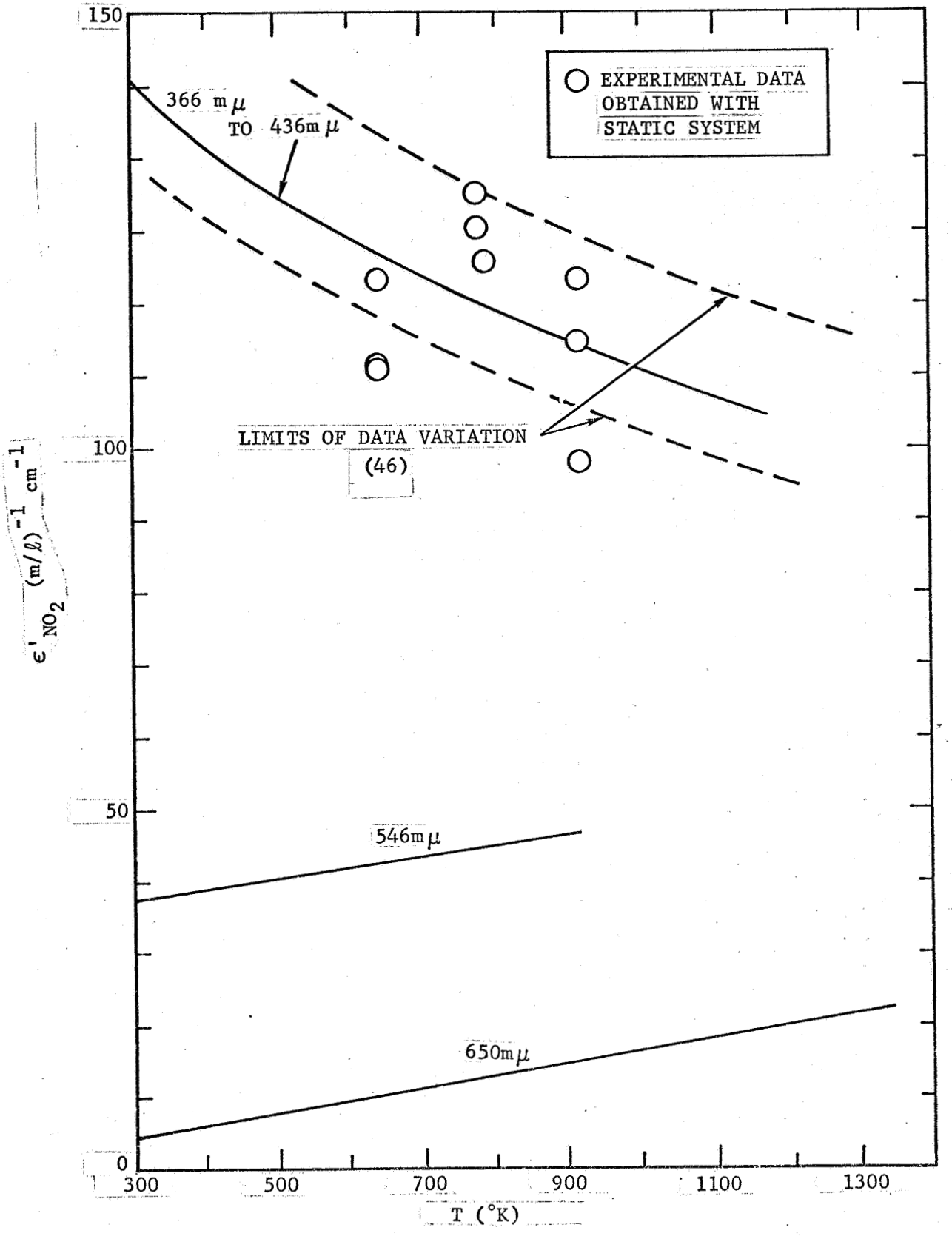

FIGURE 23. EXTINCTION COEFFICIENTS OF NO_2 - DATA FROM QUARTZ ROD SYSTEM

psi increase in total system pressure per minute

8. Cooling water to the mechanical seal housing of the turboblower turned on when total NO_2 gas pressure in the system reaches 5 psig

9. Turboblower turned on

10. Temperature controllers adjusted to give the desired temperatures in the bulk gas and at the back wall of the test section

11. Heat flux and wall temperatures monitored until a steady state is reached

12. Start experimental measurements.

From four to six hours were usually required for the completion of steps 2 through 11.

2.4.2 SHUT-DOWN

A brief summary of the most important steps involved in the shut-down of the flow system is as follows:

1. All electrical power to the heaters shut off except for that to the probe holder guard heaters and to the drip pots

2. Vent hot gaseous NO_2 until total system pressure drops to 1 atm

3. Stop the turboblower

4. Drain the water from the mechanical seal housing; neutralize any residual acid with an aqueous sodium bicarbonate solution

5. Vent valve closed; system evacuated with the jet ejector (driven with water under pressure)

6. Purging of the system continued for ~ 12 hours with room air entering the system through the micromanometer pressure lines; drip pot and probe holder guard heaters left on until the end of this purging.

Steps 1 through 5 usually take less than one hour to complete.

SECTION 3

RESULTS

3.1 DATA REDUCTION

All the equations required for reducing the data to forms considered in subsequent sections are given either in Appendix 1 or in the Nomenclature. The characteristic reaction time parameter, $\sqrt{m}$ or $N_{Da_{II_{NO_2}}}$, was derived for the reaction 2 A $\rightleftarrows$ 3 U which is a reasonable model of the dissociating NO_2 system as shown by Bodman (26).

3.2 REDUCED DATA

The reduced data from both the air and NO_2 experiments (the former are denoted with a suffix A-, the latter with a suffix N-) are given in Tables 4 to 14. All NO_2 system thermodynamic and transport properties (Section 2.1) used to reduce the data from the NO_2 experiments to the forms considered in subsequent sections consisted of the equilibrium values unless specifically noted otherwise with the subscript ξ (for frozen). The following limitations should be noted:

N-11: No radial temperature or velocity profile data were obtained; T_c and T_w estimated from N-1, N-13a, and N-14a

N-14: No radial velocity data were obtained

N-14b: No radial velocity data were obtained; values of h obtained in N-14a were used

N-15: No radial velocity profile data were obtained; values of h obtained in N-7 were used.

TABLE 4.

EXPERIMENTAL RESULTS FOR AIR - MOMENTUM TRANSFER

Run Number	m (lb$_m$/sec)	T_b (°F)	m^* (lb$_m$/sec)	G (lb$_m$/sec ft^2)	N_{Re_f}	N_{Re_b}	f	τ_w (lb$_f$/ft^2)	P (atm)	BS
A13	0.291		0.2970	14.0	147,000	155,200	0.0082	0.0423	9.9	3.0
A14	0.450		0.4930	21.6	231,300	241,300	0.0048	0.0586	10.7	4.5
A15	0.571		0.5960	27.4	243,600	307,600	0.0039	0.0764	10.5	5.5
A16		75	0.0245	1.18		15,600	0.0064		1.0	1.0
A17		75	0.0269	1.29		17,100	0.0065		1.0	1.5
A18		75	0.0316	1.52		20,100	0.0060		1.0	2.0
A19		75	0.0362	1.74		23,000	0.0056		1.0	2.5
A20		76	0.0415	1.99		26,400	0.0057		1.0	3.0
A21		76	0.0467	2.24		29,700	0.0057		1.0	3.5
A22		76	0.0522	2.51		33,200	0.0055		1.0	4.0
A23		76	0.0579	2.78		36,800	0.0052		1.0	4.5
A24		77	0.0653	3.14		41,500	0.0052		1.0	5.0
A25		77	0.0730	3.51		46,300	0.0050		1.0	5.5
A26		77	0.2782	13.4		176,700	0.0036		10.3	1.0
A27		77	0.3207	15.4		203,600	0.0036		10.2	1.5
A28		77	0.3670	17.6		232,900	0.0035		10.2	2.0
A29		79	0.4121	19.8		260,800	0.0035		10.2	2.5
A30		80	0.4631	22.2		292,600	0.0034		10.1	3.0
A31		80	0.5252	25.2		331,600	0.0040		10.1	3.5
A32		82	0.5622	27.0		354,100	0.0035		10.1	4.0
A33		84	0.6080	29.2		382,000	0.0037		10.1	4.5
A34		85	0.6779	32.5		425,000	0.0034		10.1	5.0
A35		86	0.7591	36.4		475,500	0.0035		10.1	5.5
A36						~20,000			1.0	2.5
A37						~25,000			2.4	2.5

TABLE 5

EXPERIMENTAL RESULTS FOR AIR

Run Number	Operating Conditions						
	P (atm)	BS	$(T_{ow})_{cs}$ (^oF)	$(T_\infty)_{cs}$ (^oF)	Q (BTU/sec ft^2)	T_{ow} (^oF)	T_c (^oF)
A13	9.9	3.0	400	200	0.6529	300	206
A14	10.7	4.5	300	200	0.9417	301	203
A15	10.5	5.5	300	200	0.9552	304	203
A36	1.0	2.5	950	850	0.3237	997	812
A37	2.4	2.5	950	850	-	968	750

	Heat Transfer Driving Forces				
	T_w (^oF)	T_f (^oF)	T_b (^oF)	$T_w - T_b$ (^oF)	$T_w - T_c$ (^oF)
A13	292	252	213	79	86
A14	289	249	209	80	86
A15	292	249	205	87	89

	Heat Transfer		
	h (BTU/ft^2 sec ^oF)	N_{Nu_f}	N_{Pr_f}
A13	0.00830	252	0.686
A14	0.01177	359	0.686
A15	0.01109	338	0.686

PRECEDING PAGE BLANK NOT FILMED.

START CONTINUATION PAGES HERE

TABLE 6

EXPERIMENTAL RESULTS FOR THE NONEQUILIBRIUM REACTING NO_2 SYSTEM - OPERATING CONDITIONS

START NEW SECTION PAGE HERE

Run Number	P (atm)	BS	$(T_{ow})_{cs}$ (°F)	$(T_{\infty})_{cs}$ (°F)	Q (BTU/sec ft^2)	T_{ow} (°F)	T_c (°F)
N-1	9.5	4.0	1300	900	1.8083	1094	904
N-2	7.8	5.5	1300	900	1.7759	1105	912
N-3	6.3	5.5	1300	850	1.7511	1095	873
N-4	5.1	4.0	1300	850	1.3665	1149	919
N-5	4.3	4.0	1300	800	1.4256	1143	879
N-6	3.7	5.5	1300	800	1.4701	1113	856
N-7	2.9	2.7	1300	800	1.1594	1199	930
N-8	4.5	4.0	1150	700	1.3608	962	740
N-9	4.0	5.5	1150	700	1.3907	955	736
N-11	8.5	4.0	950	875	0.7626	960	886
N-13a	10.0	2.5	1000	900	1.0337	1010	923
N-14	10.0	2.5	950	850	1.0065	937	864
N-14a	10.2	2.5	950	850	0.6825	942	863
N-14a-1	9.4	3.3	950	850	-	942	856
N-14a-2	9.3	4.3	950	850	-	942	848
N-14a-3	9.2	5.5	950	850	-	942	835
N-14b	9.1	2.5	950	850	0.6743	942	843
N-15	2.7	2.5	950	850	0.2793	963	888

TABLE 7.

EXPERIMENTAL RESULTS FOR THE NONEQUILIBRIUM REACTING NO_2 SYSTEM - ENERGY TRANSFER DRIVING FORCES

Run Number	T_w (^oF)	$T_{f'}$ (^oF)	$T_{b'}$ (^oF)	$T_w - T_{b'}$ (^oF)	$T_w - T_c$ (^oF)	$H_w - H_b$ (BTU/lb_m)	$H_{\xi_w} - H_b$ (BTU/lb_m)
N-1	1077	998	919	158	173	143	36.3
N-2	1089	1013	937	151	177	137	34.8
N-3	1079	985	892	186	206	176	42.9
N-4	1137	1038	939	197	218	170	45.4
N-5	1130	1022	915	215	251	187	49.5
N-6	1099	995	891	209	243	187	48.0
N-7	1189	1079	970	219	259	164	50.6
N-8	949	859	770	179	209	187	40.8
N-9	941	852	763	179	205	189	41.0
N-11	952	-	-	-	74	-	-
N-13a	1000	-	-	-	77	-	-
N-14	927	-	-	-	63	-	-
N-14a	935	899	862	73	72	68	19.0
N-14b	935	893	852	83	92	81	21.6
N-15	960	930	899	61	72	59	15.9

TABLE 8.

EXPERIMENTAL RESULTS FOR THE NONEQUILIBRIUM REACTING NO_2 SYSTEM - MOMENTUM TRANSFER

Run Number	m	m^*	G	N_{Re_f},	N_{Re_b},	ρ_b,	U_b	f	τ_w
	(lb_m/sec)	(lb_m/sec)	(lb_m/sec ft^2)			(lb_m/ft^3)	(ft/sec)		(lb_f/ft^2)
N-1	0.258	0.285	12.4	77,000	80,500	0.3468	35.8	0.0052	0.0360
N-2	0.278	0.299	13.4	81,900	85,200	0.2792	47.9	0.0059	0.0589
N-3	0.212	0.232	10.2	63,100	66,900	0.2333	43.6	0.0070	0.0481
N-4	0.135	0.131	6.49	39,400	42,500	0.1767	36.7	0.0075	0.0279
N-5	0.104	0.141	4.98	30,500	31.900	0.1513	32.9	0.0102	0.0260
N-6	0.147	0.146	7.06	43,800	46,300	0.1341	52.7	0.0064	0.0370
N-7	0.057	0.065	2.75	16,300	17,100	0.0948	29.0	0.0111	0.0138
N-8	0.140	0.225	6.70	45,000	47,700	0.1959	34.2	0.0077	0.0273
N-9	0.177	0.260	8.51	57,200	60,600	0.1736	49.0	0.0068	0.0441
N-13a	-	0.153	-	-	-	-	-	-	-
N-14	-	0.172	-	-	-	-	-	-	-
N-14a	0.221	0.209	10.60	69,800	71,300	0.4075	26.0	0.0047	0.0184
N-14b	0.210	0.157	10.10	66,600	68,500	0.3650	27.6	0.0042	0.0182
N-15	0.058	0.055	2.79	17,600	18,000	0.0967	28.8	0.0057	0.0075

TABLE 9

EXPERIMENTAL RESULTS FOR THE NONEQUILIBRIUM REACTING NO_2 SYSTEM — MOMENTUM TRANSFER BASED ON ORIFICE PLATE MEASUREMENTS

Run Number	m^* (lb_m/sec)	G^* (lb_m/sec ft^2)	N^*_{Re}	ρ'_b (lb_m/ft^3)	U^*_b (ft/sec)	f^*
N-1	0.285	13.69	103,800	0.3468	39.46	0.0043
N-2	0.299	14.39	109,200	0.2792	51.65	0.0051
N-3	0.232	11.16	74,000	0.2333	47.79	0.0058
N-4	0.131	6.27	56,200	0.1767	35.63	0.0080
N-5	0.141	6.79	63,700	0.1513	44.78	0.0055
N-6	0.146	7.00	63,900	0.1341	52.32	0.0065
N-7	0.065	3.13	31,600	0.0948	32.95	0.0086
N-8	0.225	10.83	89,800	0.1959	55.19	0.0030
N-9	0.260	12.47	106,700	0.1736	71.97	0.0032
N-13a	0.153	7.37	47,600	0.3667	20.10	0.0084
N-14	0.172	8.38	56,400	0.4075	20.54	0.0100
N-14a	0.209	10.02	67,000	0.4075	24.60	0.0048
N-14a-1	0.244	11.73	78,800	0.4135	28.37	0.0046
N-14a-2	0.303	14.54	97,800	0.4226	34.40	0.0052
N-14a-3	0.411	19.75	132,800	0.4286	46.04	0.0038
N-14b	0.157	7.53	54,200	0.3650	20.67	0.0075
N-15	0.055	2.63	20,900	0.0967	27.34	0.0067

TABLE 10

EXPERIMENTAL RESULTS FOR THE NONEQUILIBRIUM REACTING NO_2 SYSTEM - ENERGY TRANSFER

Run Number	h' (lb_m/sec ft^2)	h'' (BTU/ft^2 sec ^oF)	h^* (BTU/ft^2 sec ^oF)	φ	$N'_{Nu_{f'}}$	$N'_{Nu_{b'}}$	$N''_{Nu_{f'}}$	$N'''_{Nu_{f'}}$
N-1	0.01264	0.01145	0.00855	1.339	59.9	59.9	292	236
N-2	0.01294	0.01174	0.00900	1.304	61.6	62.4	296	243
N-3	0.00992	0.00939	0.00729	1.288	48.1	48.6	242	198
N-4	0.00803	0.00692	0.00531	1.303	38.5	39.3	168	144
N-5	0.00762	0.00663	0.00435	1.524	36.7	37.2	162	139
N-6	0.00785	0.00704	0.00557	1.264	38.5	39.1	180	150
N-7	0.00708	0.00529	0.00281	1.883	33.0	34.9	123	107
N-8	0.00727	0.00761	0.00510	1.492	35.6	36.0	230	163
N-9	0.00737	0.00778	0.00612	1.271	36.0	36.4	235	166
N-14a	0.01007	0.00934	0.00654	1.428				
N-14b	0.00832	0.00810	0.00706	1.147				
N-15	0.00473	0.00459	0.00267	1.719				

TABLE 11

EXPERIMENTAL RESULTS FOR THE NONEQUILIBRIUM REACTING NO_2 SYSTEM - FLUID PROPERTIES

Run Number	N_{Pr_f},	N_{Pr_b},	$N_{Le_{\xi_c}}$
N-1	0.765	0.741	0.960
N-2	0.773	0.750	0.945
N-3	0.771	0.741	0.960
N-4	0.790	0.763	0.920
N-5	0.788	0.760	0.938
N-6	0.785	0.755	0.945
N-7	0.799	0.785	0.886
N-8	0.735	0.699	1.042
N-9	0.770	0.699	1.040
N-14a	0.730	0.717	0.990
N-14b	0.732	0.714	0.998
N-15	0.773	0.763	0.908

TABLE 12

EXPERIMENTAL RESULTS FOR THE NONEQUILIBRIUM REACTING NO_2 SYSTEM - PARAMETERS REQUIRED FOR CALCULATION OF CHEMICAL KINETICS MODULI

Run Number	k_{D_c} x 10^{-4} (cm^3/mole sec)	$k_{F_{B_c}}$ x 10^4 (mole/sec cm^3 atm^2)	C_c x 10^4 (mole/cm^3)	ξ_c (mole)	$(x_{NO_2})_c$	D_c (cm^2/sec)	h_c^* x 10^3 (cal/cm^2 sec ^oK)	k_{ξ_c} x 10^4 (cal/cm sec ^oK)
N-1	6.891	0.178	1.529	0.425	0.474	0.0980	4.08	1.35
N-2	7.656	0.196	1.246	0.455	0.444	0.1209	4.33	1.36
N-3	4.551	0.123	1.032	0.420	0.479	0.1435	3.49	1.33
N-4	8.379	0.212	0.814	0.503	0.397	0.1857	2.50	1.37
N-5	4.940	0.133	0.701	0.469	0.430	0.2119	2.02	1.33
N-6	3.593	0.100	0.618	0.452	0.447	0.2341	2.64	1.31
N-7	9.638	0.240	0.455	0.582	0.324	0.3340	1.31	1.38
N-8	5.991	0.200	0.830	0.257	0.658	0.1719	2.43	1.18
N-9	5.598	0.188	0.730	0.270	0.643	0.1957	2.88	1.18
N-14a	4.023	0.111	1.688	0.363	0.539	0.0875	2.875	1.32
N-14b	3.004	0.085	1.532	0.350	0.553	0.0959	3.148	1.29
N-15	5.544	0.147	0.440	0.530	0.372	0.3389	1.300	1.34

TABLE 13

EXPERIMENTAL RESULTS FOR THE NONEQUILIBRIUM REACTING NO_2 SYSTEM - CHEMICAL KINETICS MODULI

Run Number	m_c	$\sqrt{m_c}$	$\bar{m}_c$	$\sqrt{\bar{m}_c}$	$(N_{D_{II_{NO_2}}})_c$	ℓ (cm)	ψ_c (cm^{-1})
N-1	0.325	0.570	0.943	0.971	0.0559	0.0340	58
N-2	0.186	0.431	0.542	0.736	0.0347	0.0322	46
N-3	0.135	0.367	0.500	0.707	0.0227	0.0395	34
N-4	0.209	0.457	0.758	0.871	0.0438	0.0563	26
N-5	0.158	0.397	0.752	0.867	0.0304	0.0878	21
N-6	0.057	0.238	0.271	0.521	0.0104	0.0519	17
N-7	0.188	0.434	0.835	0.914	0.0473	0.1104	13
N-8	0.046	0.215	0.236	0.486	0.0045	0.0520	19
N-9	0.022	0.148	0.110	0.332	0.0022	0.0427	16
N-14a	0.619	0.787	1.02	1.01	0.089	0.0487	47
N-14b	0.269	0.519	0.509	0.714	0.045		
N-15	0.127	0.357	0.188	0.434	0.028		

TABLE 14

EXPERIMENTAL RESULTS FOR THE NONEQUILIBRIUM REACTING NO_2 SYSTEM - ADDITIONAL GOVERNING PARAMETERS

Run Number	η_c	η_c'	$\bar{\eta}$	μ_c	λ_c	$\chi_{f'}$	$\lambda_{99\%}$
N-1	3.70	3.79	3.75	0.0560	2.27	6.03	10.3
N-2	3.74	3.92	3.83	0.0563	2.29	6.31	17.1
N-3	3.85	4.06	3.96	0.0547	2.82	6.81	25.7
N-4	3.73	4.00	3.87	0.0566	2.79	5.63	23.7
N-5	3.87	4.13	4.00	0.0549	3.41	5.42	32.0
N-6	3.95	4.13	4.04	0.0540	3.43	6.96	73.2
N-7	3.52	3.89	3.71	0.0570	3.26	4.69	43.3
N-8	3.90	3.82	3.86	0.0492	3.53	9.63	79.1
N-9	3.94	3.87	3.91	0.0491	3.50	10.20	151
N-14a	3.70	3.77	3.74	0.0542	1.02	2.08	6.2
N-14b	3.71	3.75	3.73	0.0535	1.32		12.6
N-15	3.79	4.05	3.92	0.0558	0.803		58.4

Unless noted otherwise, all values tabulated are time-average values.

3.3 ERRORS AND CORRECTIONS

3.2.1 RADIATION CORRECTION TO GAS TEMPERATURE MEASUREMENTS

Estimates were made of the effect of radiation from the heated wall of the test section to the thermocouple junction (spherical in shape) of the temperature probes. In the case of the NO_2 experiment with the largest ΔT, N-7, the true gas temperature at the centerline, taking into account the net radiant heat flux [in the manner described in (48-p.262)] between the walls and the junction bead, was estimated to be $\sim 9.3^{o}F$ less than the $930^{o}F$ actually measured (or $\sim$ 1% error). Since this represents less than a 4% error in ΔT, no attempt was made to correct the radial temperature profiles for radiation. In the case of N-11, where the ΔT was smallest, the true gas temperature was estimated to be $\sim 0.6^{o}F$ less than that which was actually measured. No attempt was made to correct for the specular absorption of the radiant energy as it passed through the NO_2 laden gas because such correction (26) was also thought to be significantly less than the error of the other measurements.

3.3.2 CHARACTERISTIC CHEMICAL RELAXATION, MOLECULAR DIFFUSION, AND FLOW TIMES IN THE VICINITY OF THE PROBE TIPS

Assuming that the flow "streamlines" are distorted from their undisturbed state (when no probe is inserted into the flow) by a distance comparable to the probe diameter at the sensing end, then the following characteristic times can be compared in order to ascertain whether or not the probes (total head tube and thermocouple probe) are capable of sensing the local nonequilibrium state of the flow,

$$\tau_F \sim \frac{d_p}{\bar{U}} \tag{2}$$

$$\tau_D \sim \frac{d_p^2}{\bar{D}} \tag{3}$$

$$\tau'_{C_{NO_2}} \sim (k_D \, C_{NO_2})^{-1} \, . \tag{4}$$

At 1 atm, $\tau'_{C_{NO_2}}$ varies between ~ 0.1 sec to 3 sec for the temperature range of 1200°F to 800°F (see Figure 2). At 10 atm total system pressure these characteristic chemical reaction times would be about 1/10 as large as those for 1 atm. In the bulk of the flow, τ_F for the impact (or total head) tube tip is on the order of 0.0001 sec for the velocities characteristic of the NO_2 experiments (Table 8). The τ_F for the thermocouple probe is ~ 1/10 of τ_F for the impact tube. Thus $\tau_F \ll \tau'_{C_{NO_2}}$ for the conditions of these experiments and thus, on this basis, the properties of the gas would not be expected to change appreciably during its "flight" from one probe diameter upstream of the probe tip down to the probe tip itself. Estimates of τ_D for the NO_2 experiments fall within the range of 0.1 to 0.3 sec which suggests that at lower total system pressures, τ_D is comparable to $\tau'_{C_{NO_2}}$ so that when molecular diffusion is the predominant transport mechanism, the chemical state of the gas could be changed in the vicinity of the probe tip.

3.3.3 CHANGE IN OPTICAL PROBE GAP WIDTH WITH TEMPERATURE

Even after thermal conditioning, the gap width between the optically flat and polished ends of the glass fiber bundles would be expected to change with temperature due to the thermal expansion characteristics of the ceramic cement, glass, and outer stainless steel tube. An estimate was made of the net gap width change expected in heating the probe tip from 77°F to 852°F (T_b, for N-14b) taking into account the actual geometry of the sensing end (ℓ = 0.0095" for Optical Probe #3 used in N-14b) and the known thermal expansion coefficients of the materials involved. The result showed that the gap width change over this temperature interval would be less than 10% of the initial gap width as measured under a microscope at ambient temperature. Such a change in ℓ would lead to a less than 10% change in the measured $\overline{C}_{NO_2}$ (i.e., the $\overline{C}_{NO_2}$ values obtained by using the ℓ based on an ambient temperature measurement should actually be decreased by up to 10% in order to take into account the actual gap width

existing at the time when the transmittance measurements were made in the high temperature flow). Since this estimate was only approximate and since a 10% change represented an upper limit (in practice, the change is probably on the order of 1%) the gap width measured at ambient temperature was used in reducing the observed transmittance data to local time-average molar concentrations of NO_2.

3.4 FRICTION FACTOR RESULTS*

Friction factor measurements were made in order to ascertain whether the presence of a nonequilibrium homogeneous reaction in the turbulent gas flow had any appreciable effect on the overall momentum transport process.

Fanning friction factor data obtained from the air experiments is shown in Figure 24. The solid line is for the correlation usually used for smooth wall tubes ($\epsilon/D = 0$)(48,p.155). The dashed line represents the influence of wall roughness on the Fanning friction factor for a wall roughness corresponding to $\epsilon/D = 0.005$ ($\epsilon = 0.010$ rms inches for $D = 1.95$ inches)(50). Results are shown for experiments carried out under isothermal conditions as well as for those in which heat transfer was taking place. Since a thin layer of scale did form on the inside of the pipe wall, particularly when the test section was heated to excessively high temperatures ($> 1400^{\circ}F$), some of the effects of surface roughness would be expected (more so in the case of the latter air experiments and the NO_2 experiments N-1 to N-9; after experiment N-9 the inside wall of the center test section was re-honed, re-establishing a relatively "smooth"

*In the case of the results presented in this and subsequent sections, all radial profile measurements were made at essentially one longitudinal position. Profile measurements were made at an L/D of 43 from the trip plate at the beginning of the entrance section (d/D of 1.50"/1.95")(see Figure 9). The flow was always directed vertically downward in the test section. The acceleration correction was not made to the static pressure drop measurements. In order to minimize the report length, most of the extensive profile measurements and property data used in the calculations was not tabulated. It was possible to cover such a large range in Reynolds number because of the capability of the flow system for handling gases at pressures up to 11 atm.

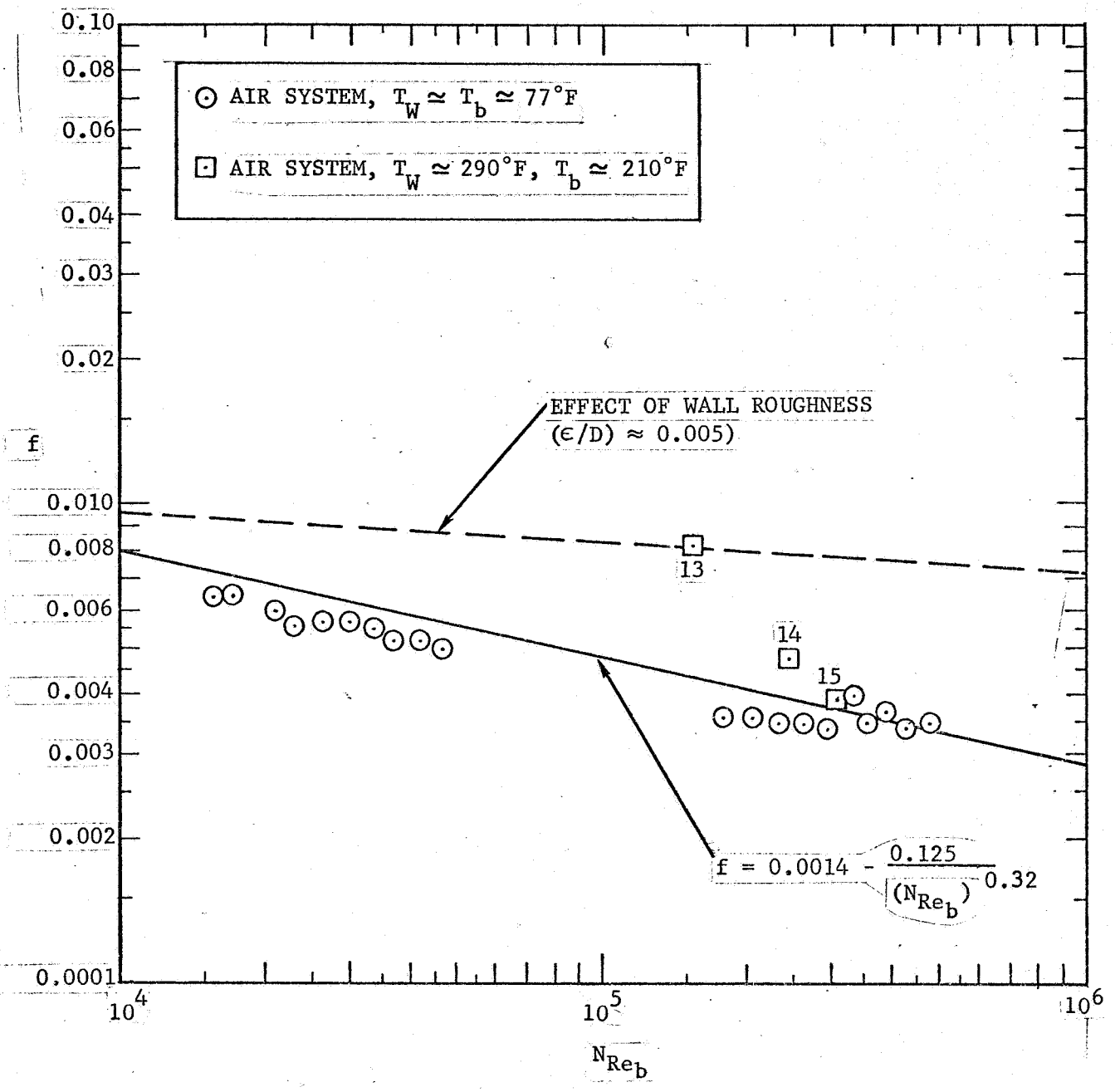

FIGURE 24. FANNING FRICTION FACTOR AS A FUNCTION OF THE BULK REYNOLDS NUMBER - AIR EXPERIMENTS

wall).

Results for the nonequilibrium reacting NO_2 system are shown in Figure 25. The data obtained after N-9 fall in the same general region as the early air data (before the system was overheated). The effect of heat transfer for the conditions of N-7 were calculated according to (48,p.157) and the result is also shown in Figure 25. Considering these results* it appears that for the conditions of these experiments there was a negligible influence of the homogeneous nonequilibrium reaction on the momentum transport.

The data shown in Figures 24 and 25 are based on velocities measured with the total head tube/static port at the test section approximately midway between the static pressure taps used for the measurement of τ_w.** Similar results were obtained with the data based on the mass flow rate measured at the orifice plate.**

3.5 NUSSELT NUMBER/REYNOLDS NUMBER CORRELATIONS

It is known from previous work (see Section 1.1) that energy transfer data for equilibrium reacting systems (arbitrary N_{Le_ξ}) will follow the same Nusselt/Reynolds number dependence characteristic of nonreacting systems provided that appropriate changes are made in the fluid properties, driving force, and choice of film temperature. This result has been substantiated by the results calculated from Model II (Table 1) for a wide range of Reynolds and Prandtl numbers (20)(case for $\sqrt{m} \to \infty$). The first step in considering the correlation of the nonequilibrium reacting system energy transfer data might best be an examination of the data in these forms.

In Figure 26, the influence of the chemical reaction on the heat transfer rate is clearly shown, i.e., under heating conditions, the homo-

*Data from experiments N-14a-1, -2, and -3 all fall reasonably close to the solid line.

**Local mass densities assumed to be equilibrium values.

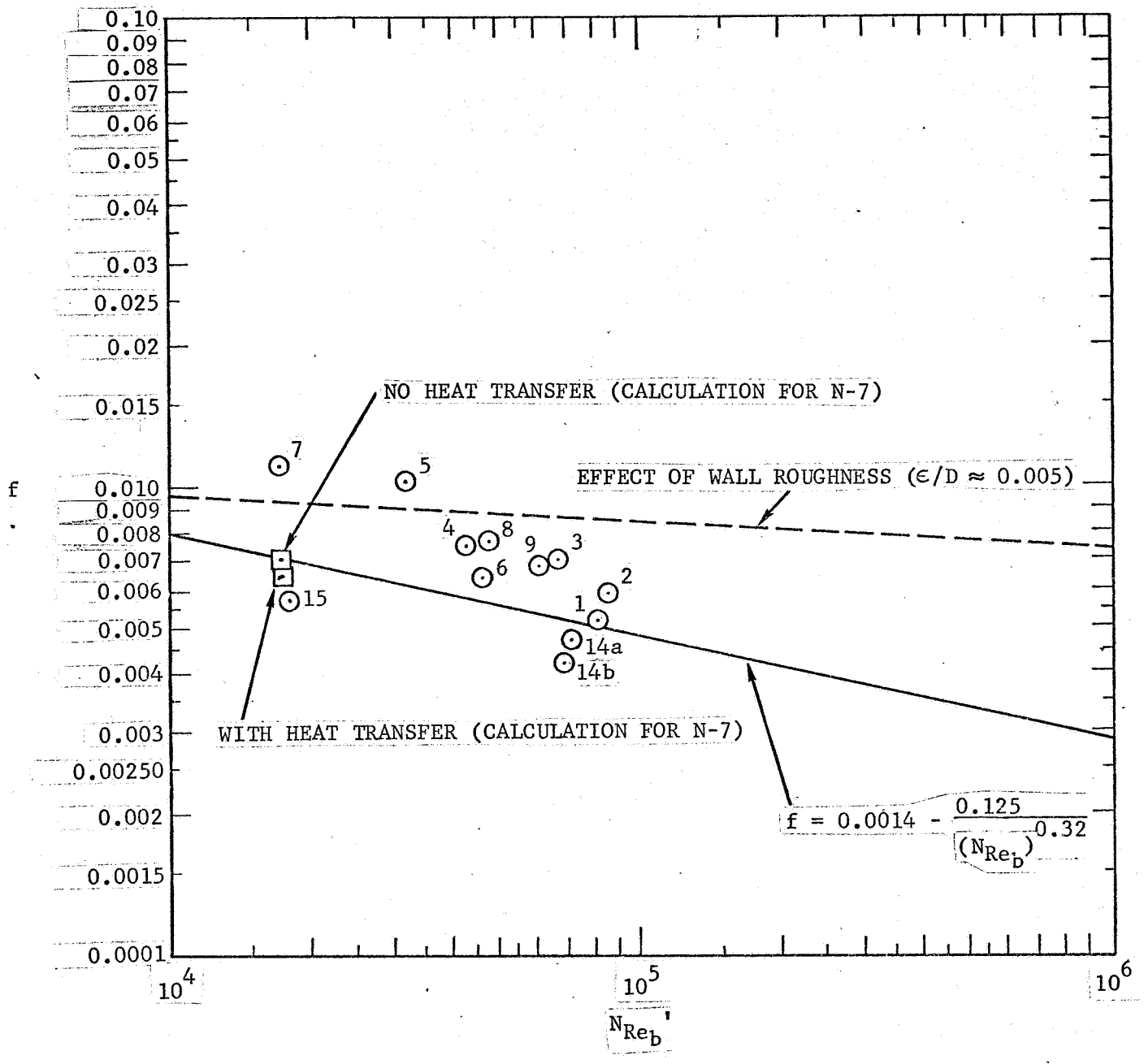

FIGURE 25. FANNING FRICTION FACTOR AS A FUNCTION OF THE BULK REYNOLDS NUMBER - NONEQUILIBRIUM NO_2 EXPERIMENTS

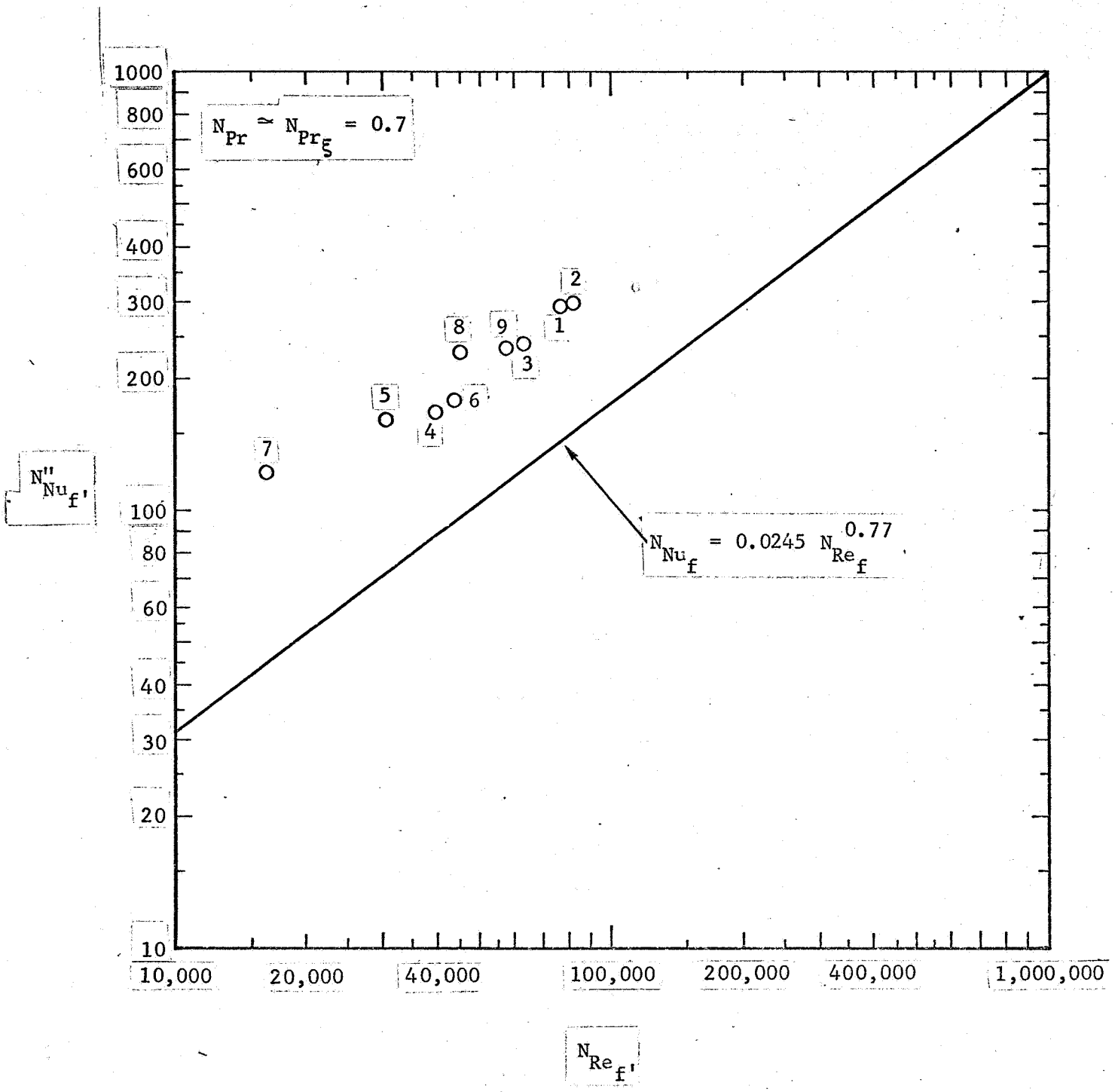

FIGURE 26. REYNOLDS NUMBER DEPENDENCE OF NUSSELT NUMBER BASED ON A TEMPERATURE DIFFERENCE DRIVING FORCE AND A FROZEN THERMAL CONDUCTIVITY - NO_2 EXPERIMENTS

geneous, endothermic chemical reaction leads to enhanced heat transfer coefficients defined in the usual sense.

In Figure 27, the necessary adjustments were made in the fluid properties, driving force, and film temperature in order to cause equilibrium reacting data to fall on the usual curve for nonreacting systems (1)(6)(10)(18). However, as would be expected, the nonequilibrium data does not correlate in that manner.

In Figure 28, a further modification is made in the driving force. Since the data shifted from below the curve in Figure 27 to above it in this figure by changing the assumed wall condition in the driving force from equilibrium to frozen, it is tempting to conclude that the true wall state is somewhere between these two extremes; and if it were known, a priori, a correlation of the data could be obtained. What is needed is a correlation which does not require such foreknowledge (i.e., in effect, the answer sought).

It has been suggested (13), based on film theory considerations, that a chemical kinetic rate-film thickness parameter, χ, might be useful in correlating heat transfer data for nonequilibrium reacting systems. The lack of such correlation is shown in Figure 29.

3.6 COMPARISON OF DATA WITH CALCULATED RESULTS FROM MODEL II

In Section 1.1 the principal assumptions of the only available analytical model (II) for predicting the effect of chemical reaction rate on energy transfer rates (or "heat" transfer coefficients) in the case of fully developed turbulent tube flow were considered. Results calculated from the film model (I) and a modification of it for the case of finite ΔT (III) were presented in Figure 1. The film model was a precursor of the tube flow model film which incorporated an eddy diffusivity. The trend of the results given in Figure 1 (normalized heat transfer coefficient as a function of the ratio of the chemical reaction rate to the molecular diffusion rate) is essentially the same as that calculated for the tube

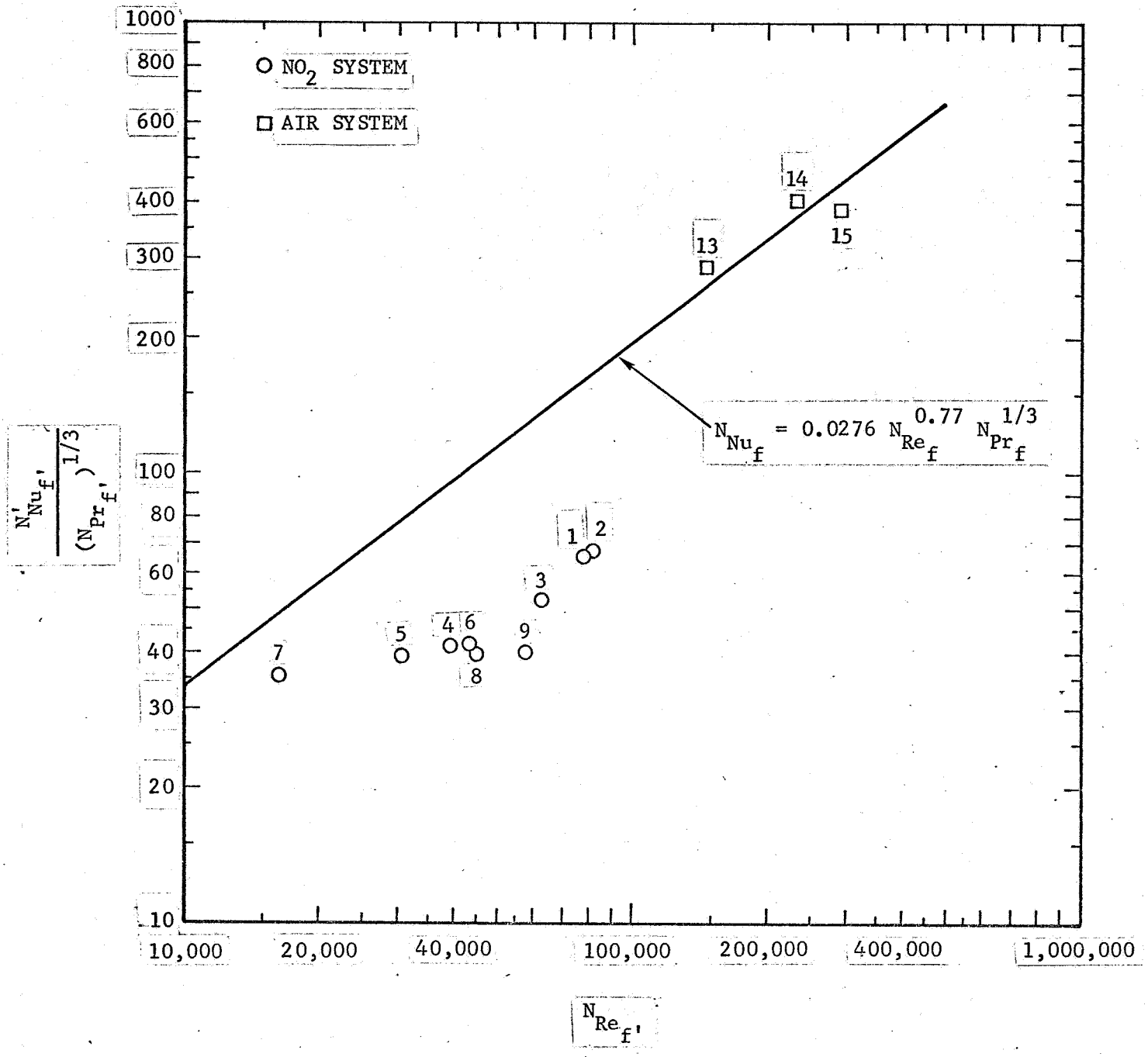

FIGURE 27. REYNOLDS NUMBER DEPENDENCE OF NUSSELT NUMBER BASED ON A SPECIFIC ENTHALPY DIFFERENCE DRIVING FORCE - NO_2 AND AIR EXPERIMENTS

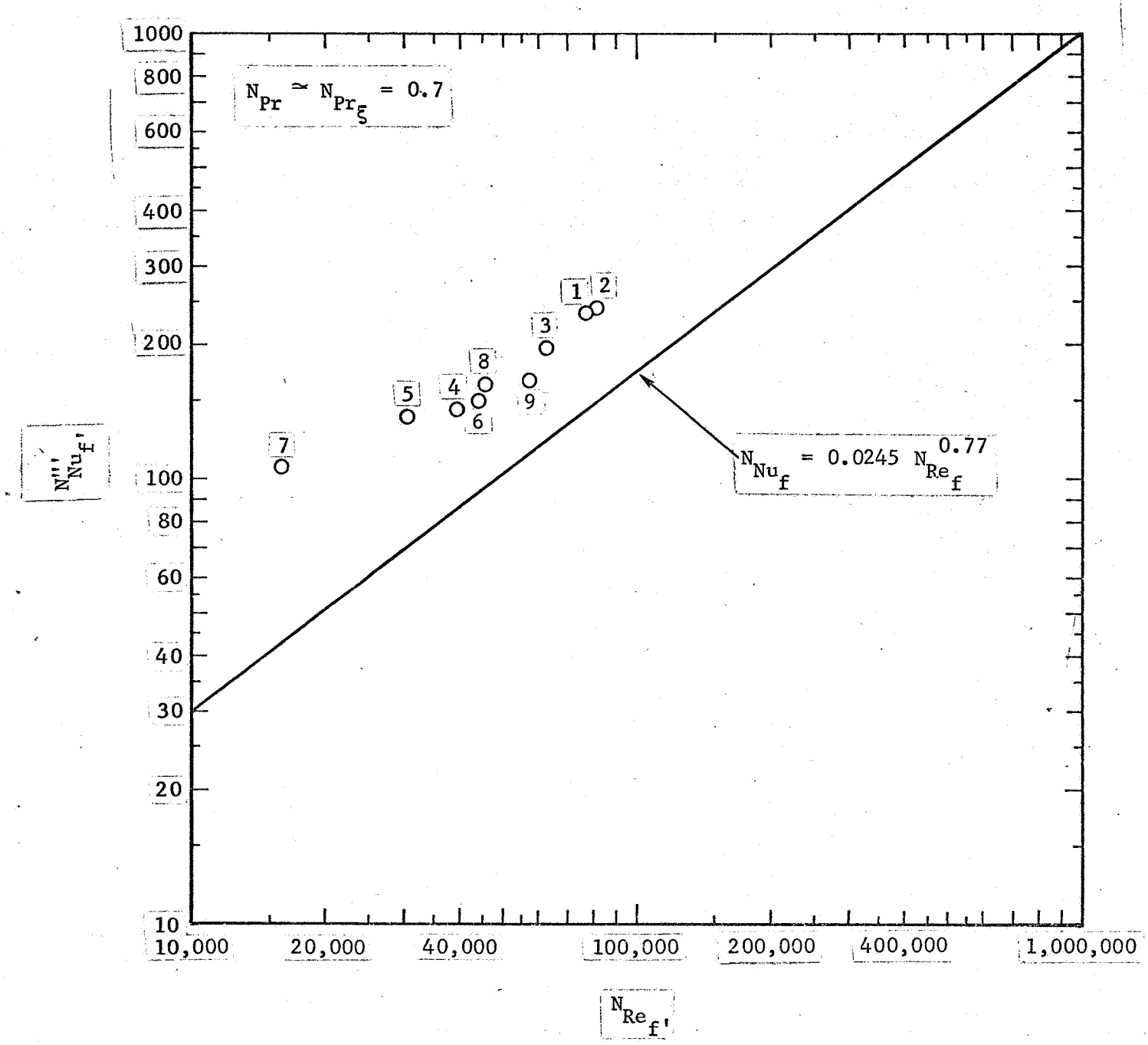

FIGURE 28. REYNOLDS NUMBER DEPENDENCE OF NUSSELT NUMBER BASED ON A SPECIFIC ENTHALPY DIFFERENCE DRIVING FORCE ASSUMING A FROZEN STATE AT THE WALL AND EQUILIBRIUM IN THE BULK - NO_2 EXPERIMENTS

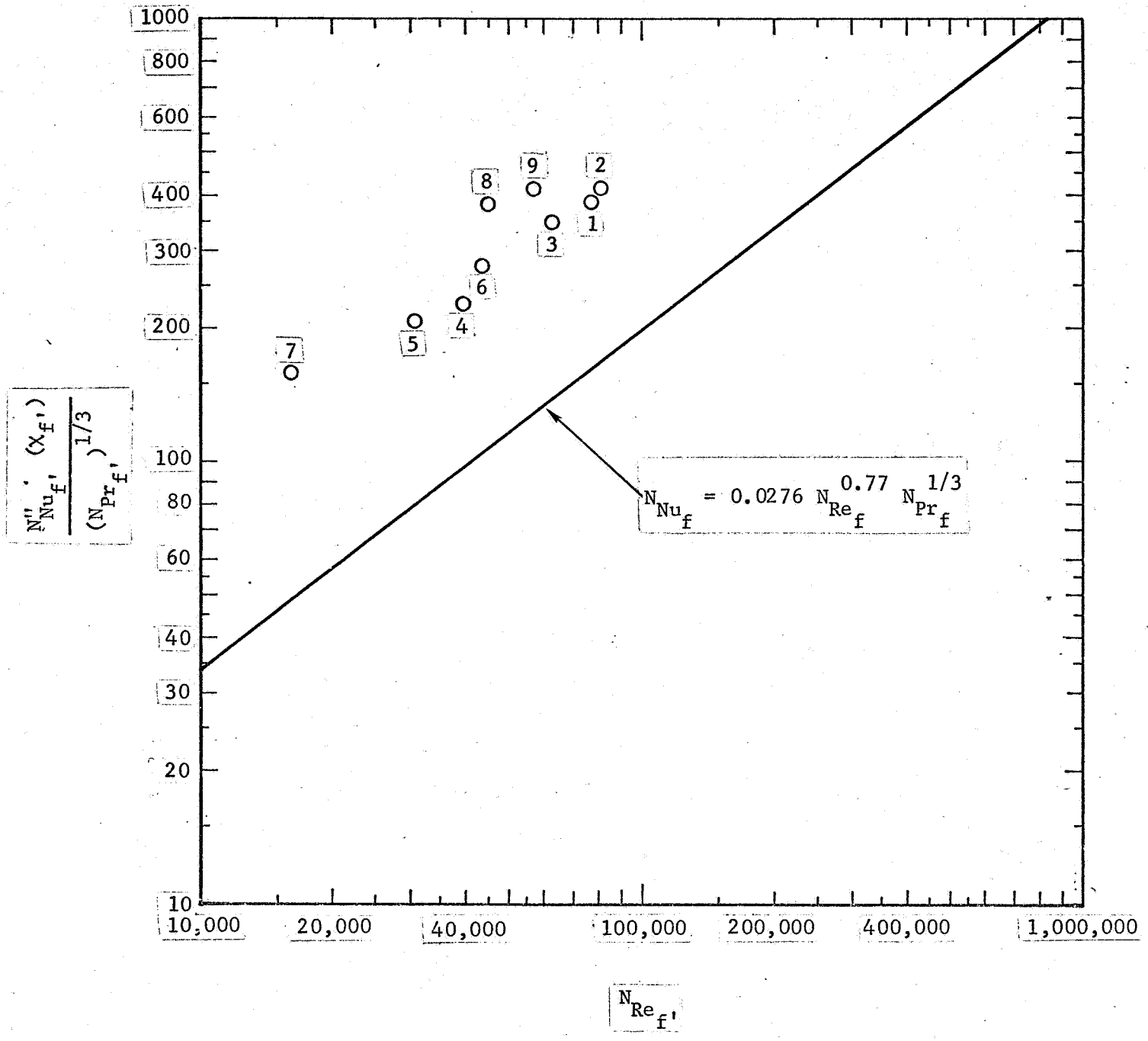

FIGURE 29. REYNOLDS NUMBER DEPENDENCE OF NUSSELT NUMBER BASED ON A TEMPERATURE DIFFERENCE DRIVING FORCE BUT MODIFIED BY A FUNCTION OF THE REACTION RATE PARAMETER, ψ - NO_2 EXPERIMENTS

flow model.

Twelve different complete ($0.1 \leq \sqrt{m} \leq 100$) calculations were made using Model II with $N_{Le_\xi} = 1$ for the Reynolds numbers, Prandtl number, and $\overline{\eta}$ values corresponding to experiments N-1 to N-9, N-14a, N-14b, and N-15 (values of $N_{Re_b'}$, $N_{Pr_b'}$, and $\overline{\eta}$ for these experiments are listed in Tables 8, 11, and 14, respectively). As has been noted (20), the dependence of φ on $\sqrt{m}$ is quite insensitive to Reynolds number when $N_{Le_\xi} = 1$. The results of the calculations for two cases (using $N_{Re_b'}$, $N_{Pr_b'}$, and $\overline{\eta}$ values corresponding to experiments N-2 and N-7) are shown in Figure 30. Previous calculations carried out with model II for $N_{Le_\xi} = 1$ had not been reported for $\overline{\eta} < 6$ (20). The dependence of φ on $\sqrt{m_c}$ is sensitive to the value of $\overline{\eta}$ (at $\sqrt{m_c} = 10$, our calculations show that φ increases essentially linearly with increasing $\overline{\eta}$ with a slope of 0.63 — the influence of Reynolds number is slight; at $\sqrt{m_c} = 1$, φ increases only slightly with increasing $\overline{\eta}$). The calculated curves which are shown in Figure 30 bracket all of the calculated results we obtained for the other ten cases in the $\sqrt{m_c} < 2$ region. Thus these two curves are sufficient for comparison, in a qualitative sense, of the experimental data with the predictions of the model.

The experimental data (tabulated in Tables 10 and 13) are also shown in Figure 30. The open circles represent the data uncorrected for the fact that in each experiment a $\Delta T > 40^{\circ}F$ [if $\Delta T < 40^{\circ}F$, in the case of the NO_2 decomposition, it was found that the film model corrected for ΔT finite gave results very close to those obtained for $\Delta T \rightarrow 0$ — quite large differences were noted at $\Delta T = 190^{\circ}F$ (21)] prevailed. The solid circles represent a correction made to m_c in order to account for the exponential dependence of the forward specific reaction rate constant on temperature between the wall and the bulk regions of the flow. Using the same procedure as applied in the case of the film model (21), k_{F_B} was corrected by,

$$\overline{k}_{F_B} = \left(k_{F_B}\right)_c \exp\left[-\frac{H^{\dagger}}{R}\left(\frac{1}{T_f} - \frac{1}{T_c}\right)\right] \tag{5}$$

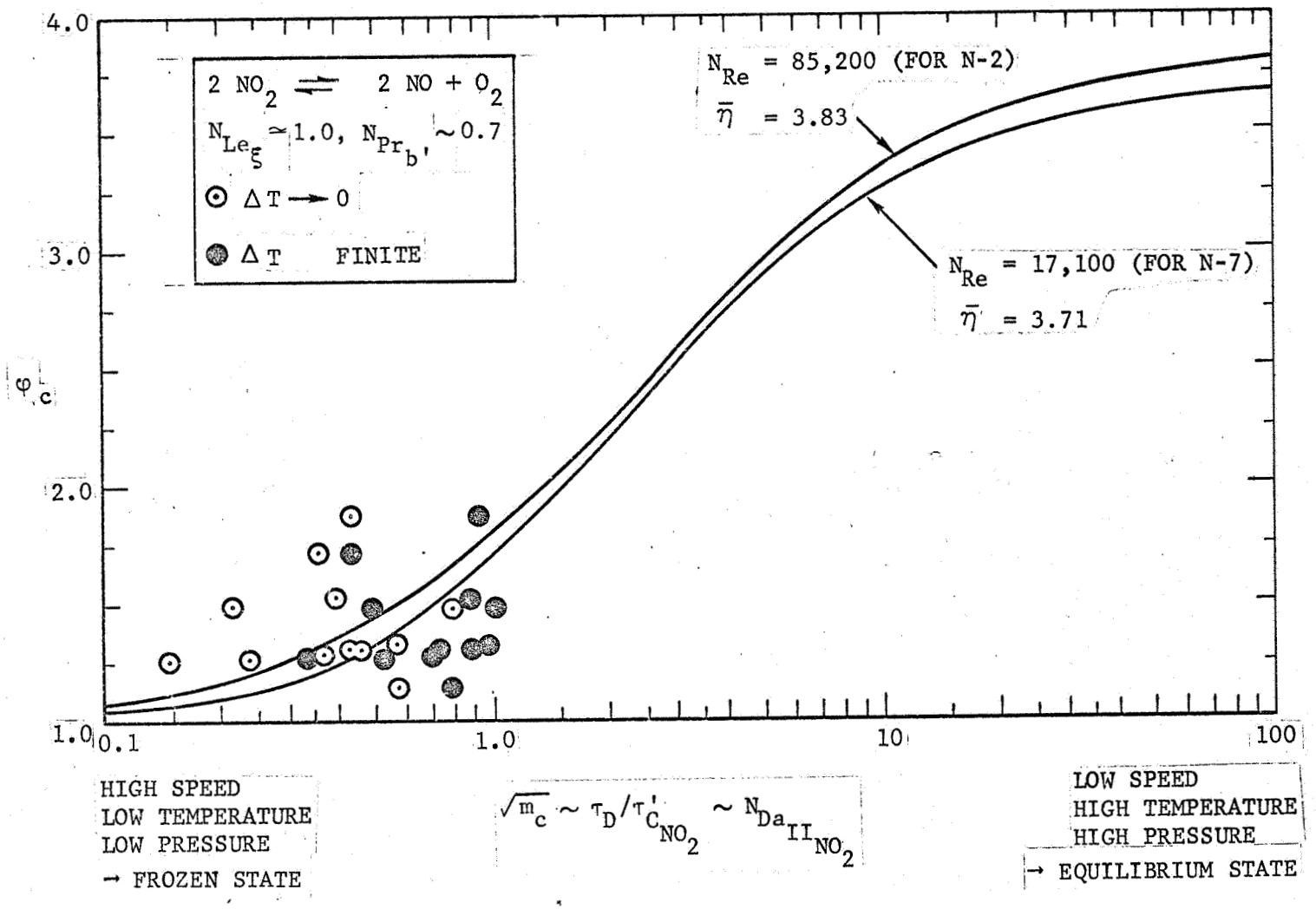

FIGURE 30. EFFECT OF CHEMICAL REACTION RATE ON ENERGY TRANSFER RATE - COMPARISON OF EXPERIMENTAL DATA WITH PREDICTIONS OF MODEL II

where $$T_f = \frac{(T_w + T_c)}{2} \tag{6}$$

so that m was in turn modified by,

$$\overline{m}_c = m_c \left(\overline{k}_{F_{B_c}} / k_{F_{B_c}}\right). \tag{7}$$

Thus the abscissa in Figure 30 should be interpreted as $\sqrt{\overline{m}_c}$ in the case of the solid circles. It is apparent that correcting for a finite ΔT has the effect of shifting the data points to the right in Figure 30. A close examination of Tables 12, 13, and 14 with reference to the independently fixed operating conditions listed in Table 6 reveals how temperature, pressure, and flow rate affect $\sqrt{m_c}$. The designations under the right and left hand ends of the abscissa in Figure 30 are an approximate indication of which conditions tend to favor a higher or lower value of $\sqrt{m_c}$.

In Table 14 are listed the $\lambda_{99\%}$ values for each experiment. Since the start of the heat transfer section coincided with the trip plate ~ 43 test section diameters upstream of the probes (TC, PT, and OP), then the steady state reaction rate assumption of Model II was not fulfilled by the conditions of experiments N-6, N-8, and N-9 (i.e., in each of these cases the radial profile data were obtained at an axial position which was estimated not to be far enough downstream from the start of the heat transfer section so that the reaction rate, r_i, no longer depended on axial position).

A quantitative comparison of the experimental data with the predictions of Model II is shown in Figure 31. The scatter about the 45° line is slightly larger (approximately ± 17% for both the open and closed circles) than that reported by Bodman and coworkers (22)(23)(approximately ± 10%) for the comparison between the predictions of models I, III, and IV and experimental data (no radial profiles were measured — only overall measurements were made) obtained for the turbulent flow of nonequilibrium reacting NO_2 outside a rotating cylinder. In the rotating cylinder experiments the bulk condition was known and agreed with the assumptions

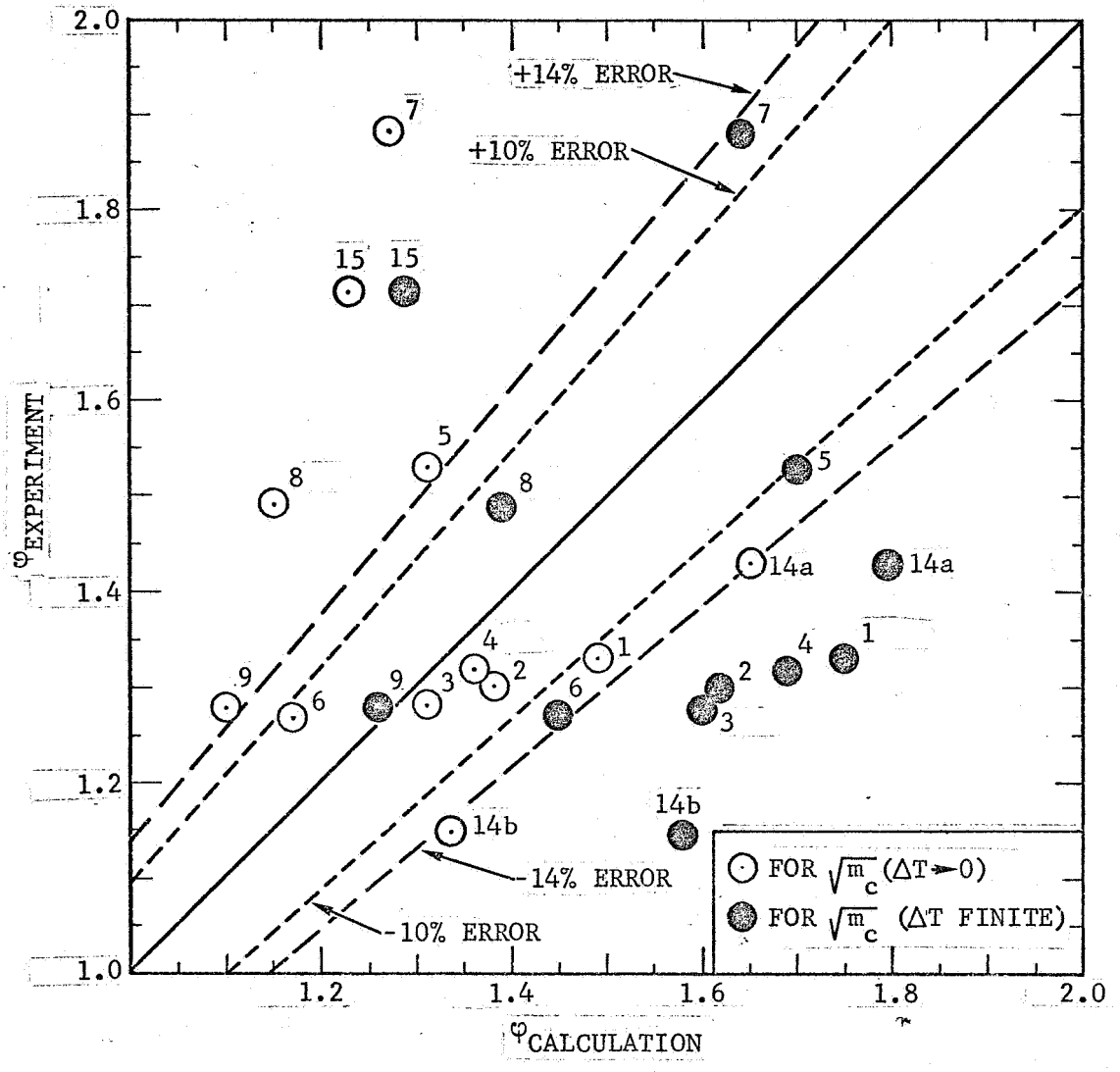

FIGURE 31. COMPARISON OF EXPERIMENTAL DATA WITH THE PREDICTIONS OF MODEL II

of the models. In the case of the tube flow experiments, the bulk "boundary condition" was postulated only. Evidence is presented in the following section that in those cases where the bulk condition was fully determined, the gas was not in chemical equilibrium. In one case, it consisted of essentially unreacted NO_2 (in this case nonequilibrium conditions must have existed over a portion of the region between the bulk of the flow and the wall). Thus calculation of φ and $\sqrt{m_c}$ or $\sqrt{\overline{m}_c}$ from the experimental data using equilibrium properties [as suggested for the $\Delta T \rightarrow 0$ case treated in (20)] is not consistent with the data and could, in itself, account for the scatter being greater than that observed for the rotating cylinder measurements. It should be noted that the heat transfer measurements reported here were for a constant temperature wall condition and not for a constant heat flux condition (from trip plate to sensor location).

The data do suggest that the trend of the predictions from Model II is valid. Most of the data corrected for finite ΔT tend to lie on or below the calculated curves rather than above them.

3.7 CONCENTRATION PROFILES — TIME-AVERAGE DATA

As noted in Section 2.3.4, the optical probe system was modified to accommodate ¼" diameter quartz rods for use in measuring the extinction coefficients, $\epsilon_{NO_2}(\lambda,T)$, in the static reactor. This same assembly was used to make the measurement of $\overline{C}_{NO_2}(r)$ shown in Figure 32. The solid line drawn through the data points is shown in order to help define the trend of the data. For comparison, the dashed line shows how the equilibrium concentration profile would vary with radial position for the estimates of $\overline{T}(r)$ obtained from previous experiments characterized by similar operating conditions. The reference equilibrium concentrations shown at the center of the tube ($r/r_o = 0$) indicate that the nonequilibrium concentration profile was the equivalent of $\sim 6^oF$ (in terms of equilibrium concentration differences) away from the equilibrium profile derived from the estimated temperature profile. Uncertainties in knowing the gap width, ℓ,

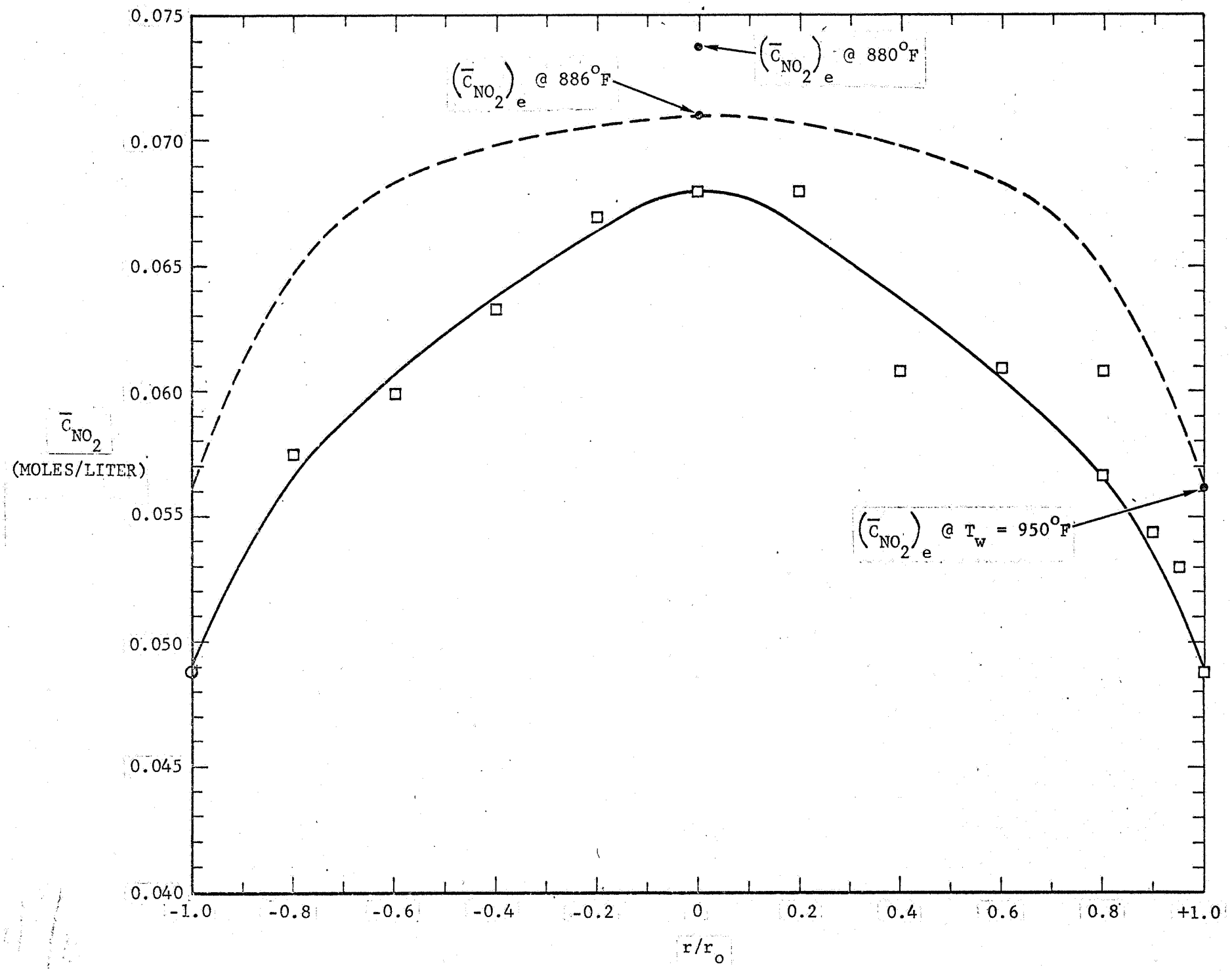

FIGURE 32. CONCENTRATION PROFILE OBTAINED FROM TRAVERSE OF QUARTZ RODS WITH FIXED GAP

at the pressures and temperatures of the experiments, problems with rod breakage due to slight misalignments (at high temperature conditions) between the probe holders on opposite sides of the test section, and difficulties in translating the entire optical assembly (Figure 21) for each radial traverse strongly encouraged us to develop the fiber bundle probe for use at high temperatures at moderate pressures (< 11 atm).

The radial concentration profile data shown in Figure 33 were obtained with the fiber optics probe (ℓ = 0.0095 inches). The raw data were obtained two different ways (refer to Figure 20) — the values obtained from the electronic counter are expected to be more accurate. There is some uncertainty as to the exact radial position of the gap during this particular experiment. We expect that the measured profile data should be shifted to the right $\sim$ 0.2". In any event the results show that across the majority of the flow conduit, the gas is nearly twice as concentrated in NO_2 as would be predicted had equilibrium conditions prevailed (the dashed line is based on the measured temperature profile and the pressure which existed in the flow system at the time of the concentration profile measurement).

As indicated in Section 3.3.3, approximate corrections for the change in gap width between the ends of the fiber bundles as the probe end was heated up to the test conditions for experiment N-14b suggest that the actual nonequilibrium concentrations would be no more than 10% less than the observed values.

It is of interest to determine the local mass density profile having measured the nonequilibrium concentration profile. Since, for the $2\ NO_2 \rightleftarrows 2\ NO + O_2$ system,

$$x_{NO_2} = \frac{1 - \xi}{1 + \frac{\xi}{2}} \tag{8}$$

$$x_{NO} = 2\ x_{O_2} = \frac{\xi}{1 + \frac{\xi}{2}} \tag{9}$$

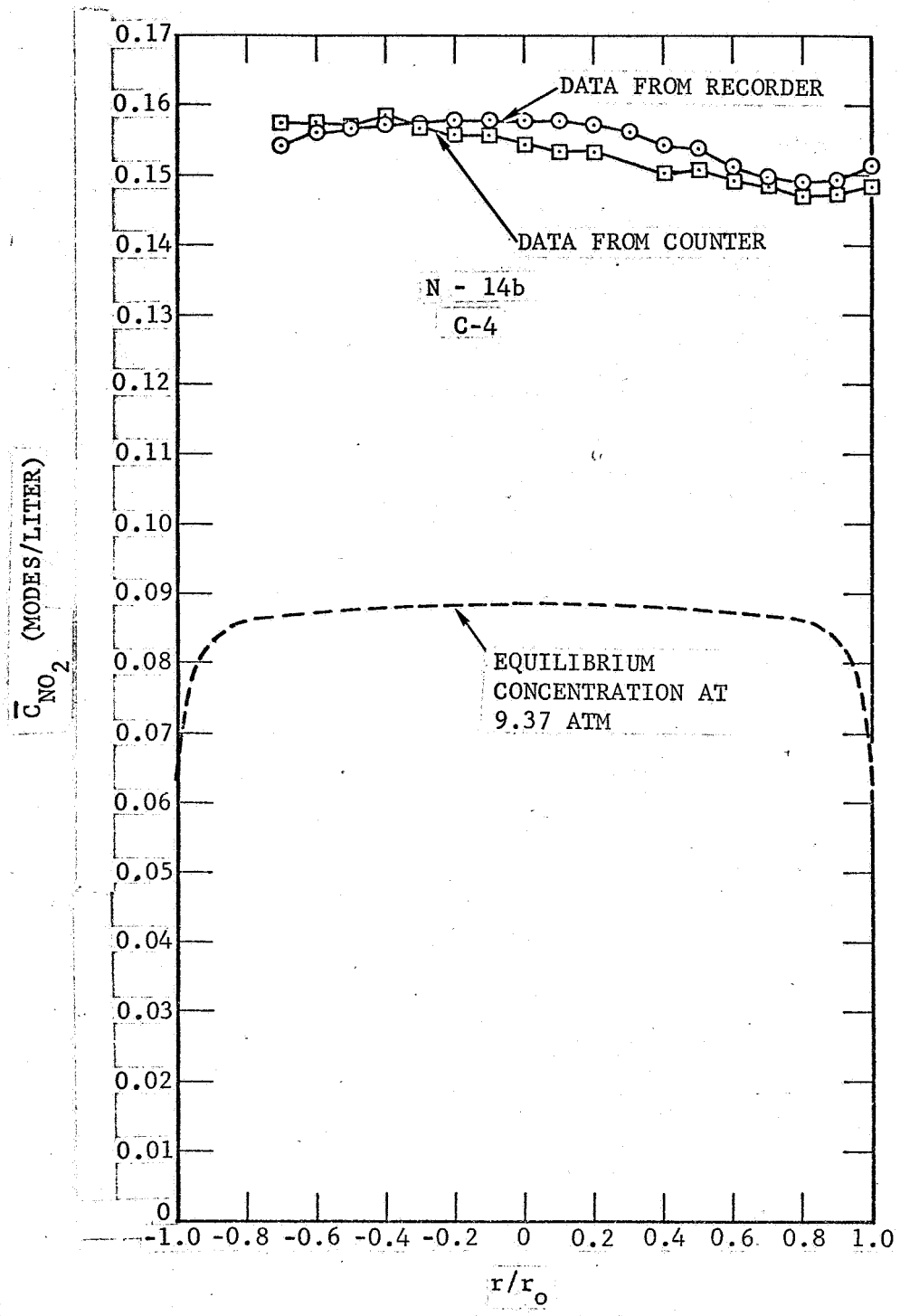

FIGURE 33. CONCENTRATION PROFILE OBTAINED FROM FIBER OPTICS PROBE

$$x_{NO_2} + x_{NO} + x_{O_2} = 1 \tag{10}$$

$$\xi = \frac{\left(1 - x_{NO_2}\right)}{\left(1 + \frac{x_{NO_2}}{2}\right)} \tag{11}$$

$$C_{NO_2} = x_{NO_2}\ C \tag{12}$$

$$C = \frac{P}{RT} \tag{13}$$

$$\rho = \frac{PM}{RT} \tag{14}$$

$$M = \sum_i x_i\ M_i \tag{15}$$

then

$$x_{NO_2} = \frac{C_{NO_2}}{\left(\frac{P}{RT}\right)} \tag{16}$$

and

$$\rho = \frac{P}{RT}\left[\frac{(1 - \xi)\ M_{NO_2} + \xi\ M_{NO} + \left(\frac{\xi}{2}\right) M_{O_2}}{\left(1 + \frac{\xi}{2}\right)}\right]. \tag{17}$$

For experiment N-14b,

$$\left(\overline{C}_{NO_2}\right)_{e_c} \sim 0.0885 \text{ gm moles/liter}$$

$$\left(\overline{C}_{NO_2}\right)_{e_w} \sim 0.0635 \text{ gm moles/liter}$$

$$\left(\overline{C}_{NO_2}\right)_{c} \sim 0.156 \text{ gm moles/liter}$$

$$\left(x_{NO_2}\right) \sim 0.99$$

$$\xi_c \sim 0.0067$$

$$\rho_c \simeq 0.452 \text{ lb}_m/\text{ft}^3$$

$$(\rho_e)_c \simeq 0.365 \text{ lb}_m/\text{ft}^3 .$$

Thus, considering the fact that the nonequilibrium mass density is ~ 20% larger in this case than the equilibrium value consistent with the measured temperature, then the nonequilibrium Reynolds number would be correspondingly larger than the value given in Table 8.

Since only a limited amount of time-average radial concentration data was obtained, it was not possible to re-evaluate the φ versus $\sqrt{m_c}$ data in order to ascertain if it agreed more closely with the Model II predictions when the "true" local nonequilibrium conditions were used in calculating φ and $\sqrt{m_c}$ or $\sqrt{\overline{m}_c}$. Considering the overall length of the flow system (Figure 6) and the long characteristic chemical reaction (i.e., dissociation) times for the NO_2 system at temperatures ~ 750°F (a good estimate for N-14b — most of the gas in the system at a given instant would be at some temperature less than T_c at the sensor location in the test section)(see Figure 2), it is not too surprising that the bulk fluid consisted, in this experiment, of mostly NO_2.

3.8 MOMENTUM/ENERGY TRANSPORT ANALOGY CONSIDERATIONS

The fair similarity between the radial velocity and temperature defect distributions shown in Figures 34 and 35 seem to justify the assumption of an analogy between energy and momentum transport in nonisothermal, nonequilibrium reacting, fully developed turbulent tube flow (51,p.538). One consequence of the Reynolds analogy is that the following relation should be valid (51,p.542),

$$N_{St} = \frac{\frac{f}{2}}{N_{Pr}} . \tag{18}$$

For reacting systems it might be more appropriate to replace N_{St} with N'_{St}.

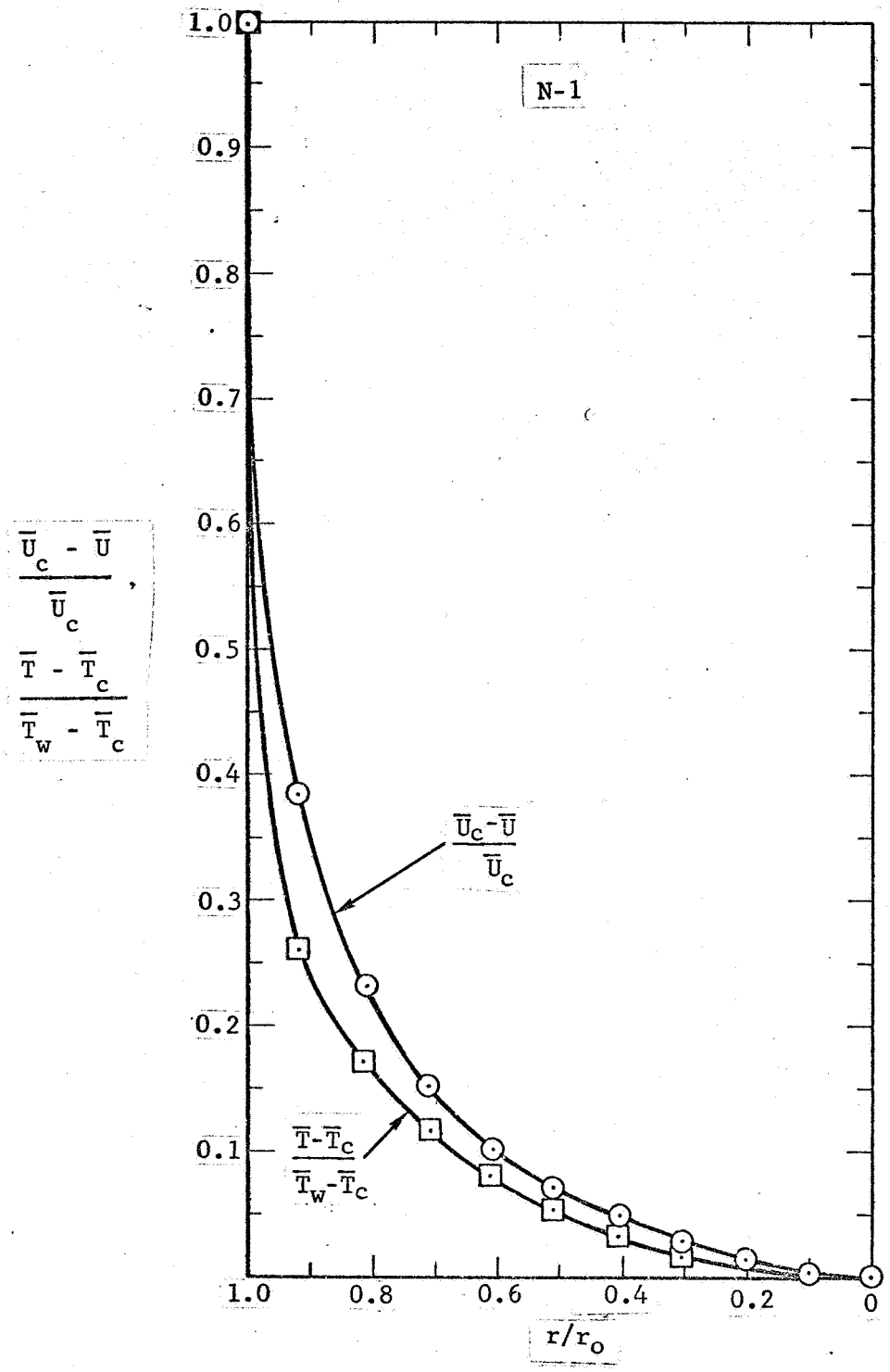

FIGURE 34. VELOCITY AND TEMPERATURE DEFECT IN NONISOTHERMAL, NONEQUILIBRIUM REACTING TUBE FLOW

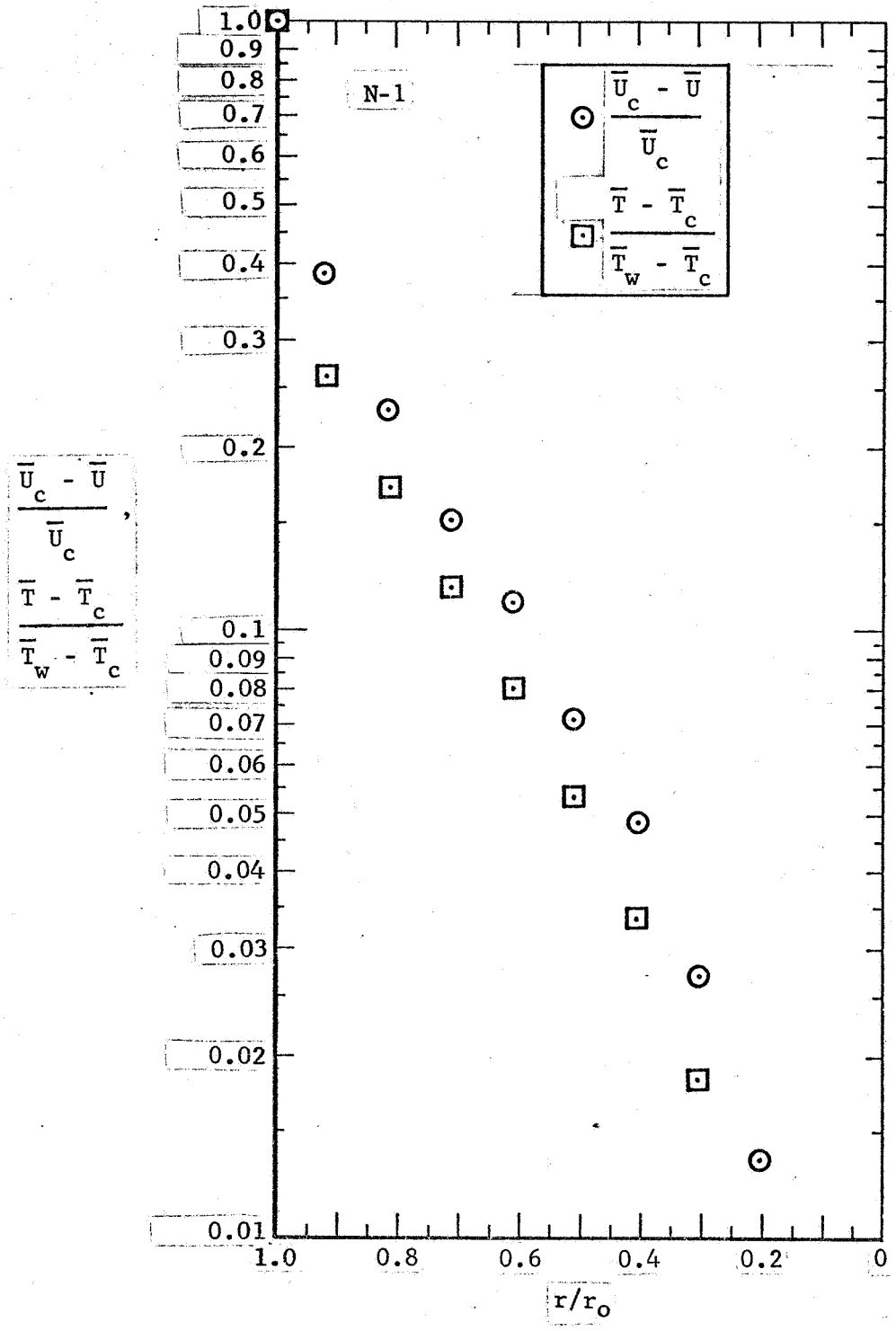

FIGURE 35. VELOCITY AND TEMPERATURE DEFECT IN NONISOTHERMAL, NONEQUILIBRIUM REACTING TUBE FLOW

Data from experiment N-1 were used to check the equivalence of Eq. 18. The following results were obtained:

$$N_{St_c} = 0.00082 \; ; \quad \frac{\frac{f}{2}}{N_{Pr_c}} = 0.0035$$

$$N_{St_{b'}} = 0.0011 \; ; \quad \frac{\frac{f}{2}}{N_{Pr_{b'}}} = 0.0035$$

$$N'_{St_c} = 0.00090$$

$$N'_{St_{b'}} = 0.0012 \; .$$

Thus the two sides of Eq. 18 are equivalent only within a factor of three, at best.

An additional check for an analogy would be the comparison between ϵ_H and ϵ_M. This is discussed in Section 3.10.

3.9 NORMALIZED RADIAL PROFILES OF SPECIFIC ENTHALPY AND TEMPERATURE

It has been shown (10) that the normalized radial profiles of specific enthalpy obtained for homogeneous equilibrium reacting systems are similar over wide ranges of Reynolds number, wall temperature-bulk temperature difference, etc. Furthermore, these profiles all fall on the same dimensionless normalized profile, T^+ versus y^+, used to express the radial temperature profile similarity in the case of fully developed nonreacting turbulent shear flows (52,p.444).

The radial specific enthalpy profiles are shown in normalized form in Figure 36. Certainly the H^+ versus y^+ form is not valid for flows in which the flow is not in chemical equilibrium. It is interesting to note that the data, which was obtained for $y^+ > 10$ and which was derived from the temperature profile data by using equilibrium properties, tends to fall on straight lines whose intersection occurs in the vicinity of the

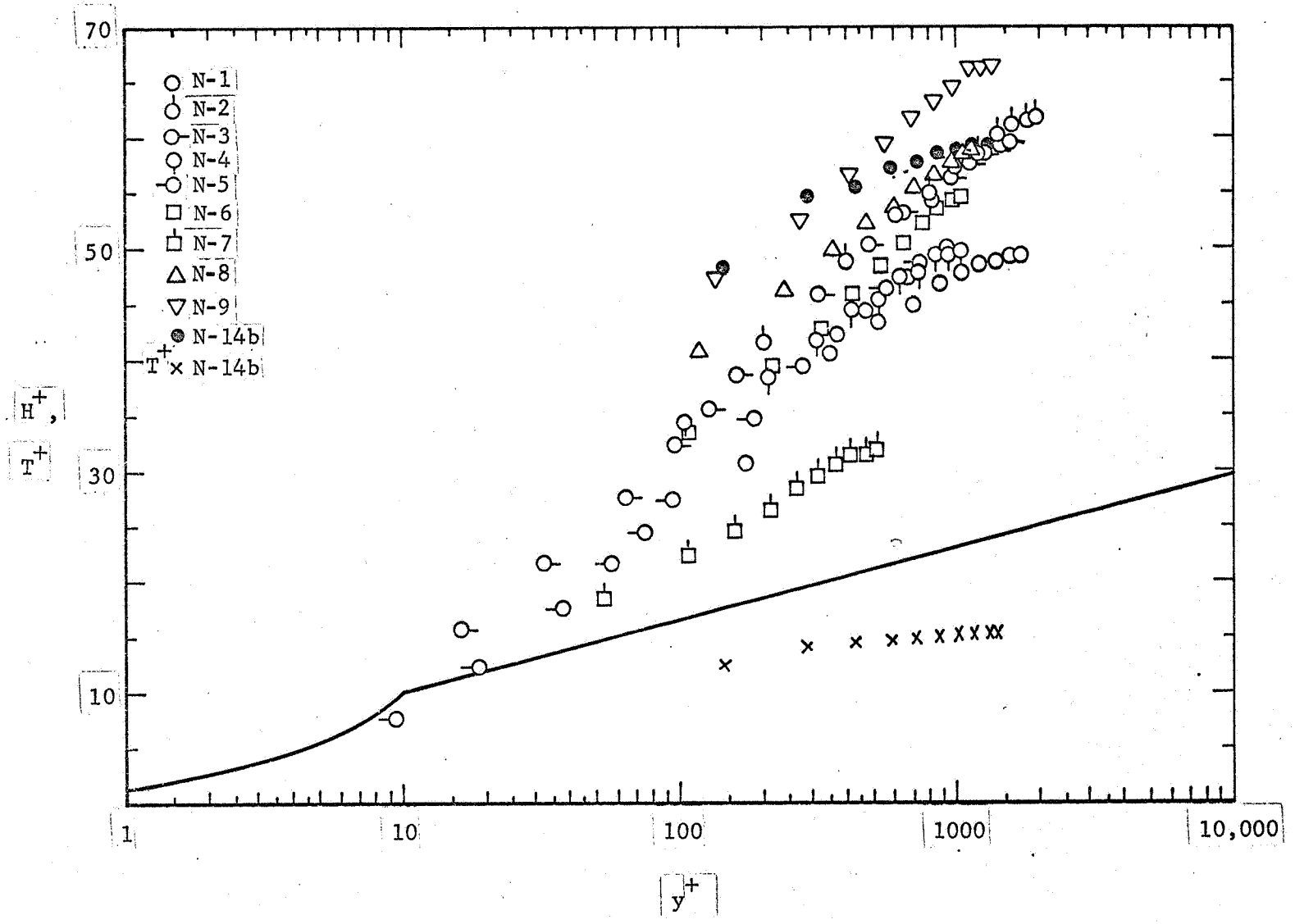

FIGURE 36. DIMENSIONLESS RADIAL SPECIFIC ENTHALPY AND TEMPERATURE PROFILES

junction between the nonlinear and the linear universal profile (solid line in Figure 36). This suggests that if a correction factor is applied to the H^+ of each profile in order to account for the deviation of the bulk from equilibrium, then the lines through the data might be made to coincide with the universal profile.

Since a good measurement of the actual bulk state was obtained in the case of N-14b, the data were also put into the T^+ form (see definition in the Nomenclature) with $C_{P_\xi} \approx C_{P_{\xi_{NO_2}}}$ in this particular case. The effect on the data is to shift them slightly below the universal curve, suggesting that an isobaric specific heat slightly greater than C_{P_ξ} should be used (which is consistent with the limitations of the concentration discussed in Section 3.7).

3.10 EDDY DIFFUSIVITIES — THEIR ESTIMATION AND COMPARISON

The eddy diffusivities for energy, momentum, and mass transfer are, when compared with their molecular counterparts for the situation of interest, indicative of the influence of the turbulent mixing processes on the total transport in the turbulent flow (51,pp.25,542). We have calculated the eddy diffusivities for momentum (ϵ_M) and energy transport (ϵ_H and ϵ'_H) using the fact that the local shear stress is linear with pipe radius and that the heat flux varies with the radius in a similar manner. The latter assumption is that commonly used in calculating ϵ_H for nonreacting systems (48,p.209). Its limitations have been reviewed by Hinze (51,pp.550-551).*

The results for the case of a typical experiment, N-1, are shown in Figures 37, 38, and 39. The shapes of the various eddy diffusivity profiles (see Nomenclature for defining equations) are similar to those reported for nonreacting systems (52,p.439) and for equilibrium reacting

---

*A more accurate determination would require the differentiation of both radial and axial profile information in the manner prescribed by the appropriate conservation equation.

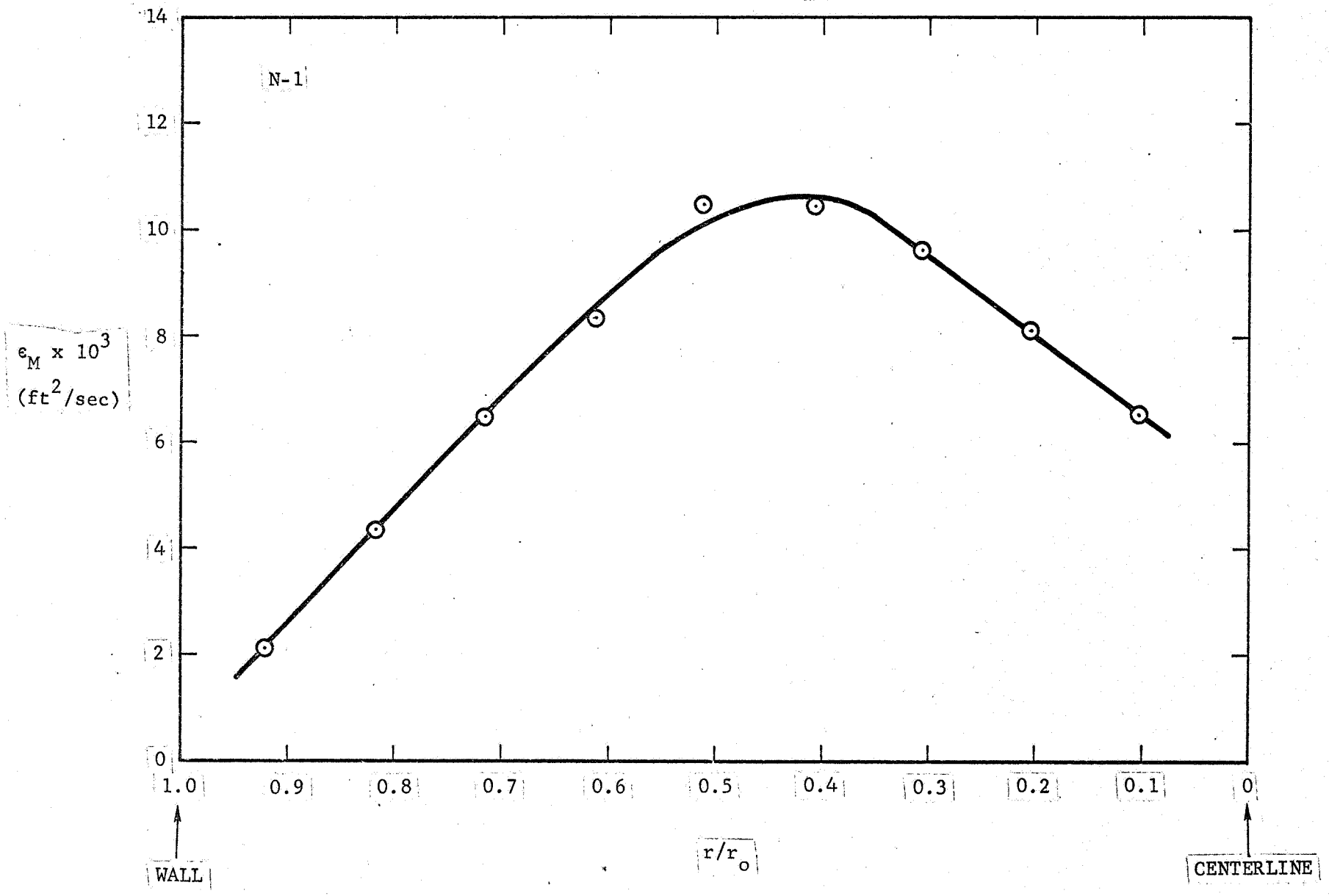

FIGURE 37. EDDY DIFFUSIVITY FOR MOMENTUM TRANSFER AS A FUNCTION OF RADIAL POSITION (EXPERIMENT N-1)

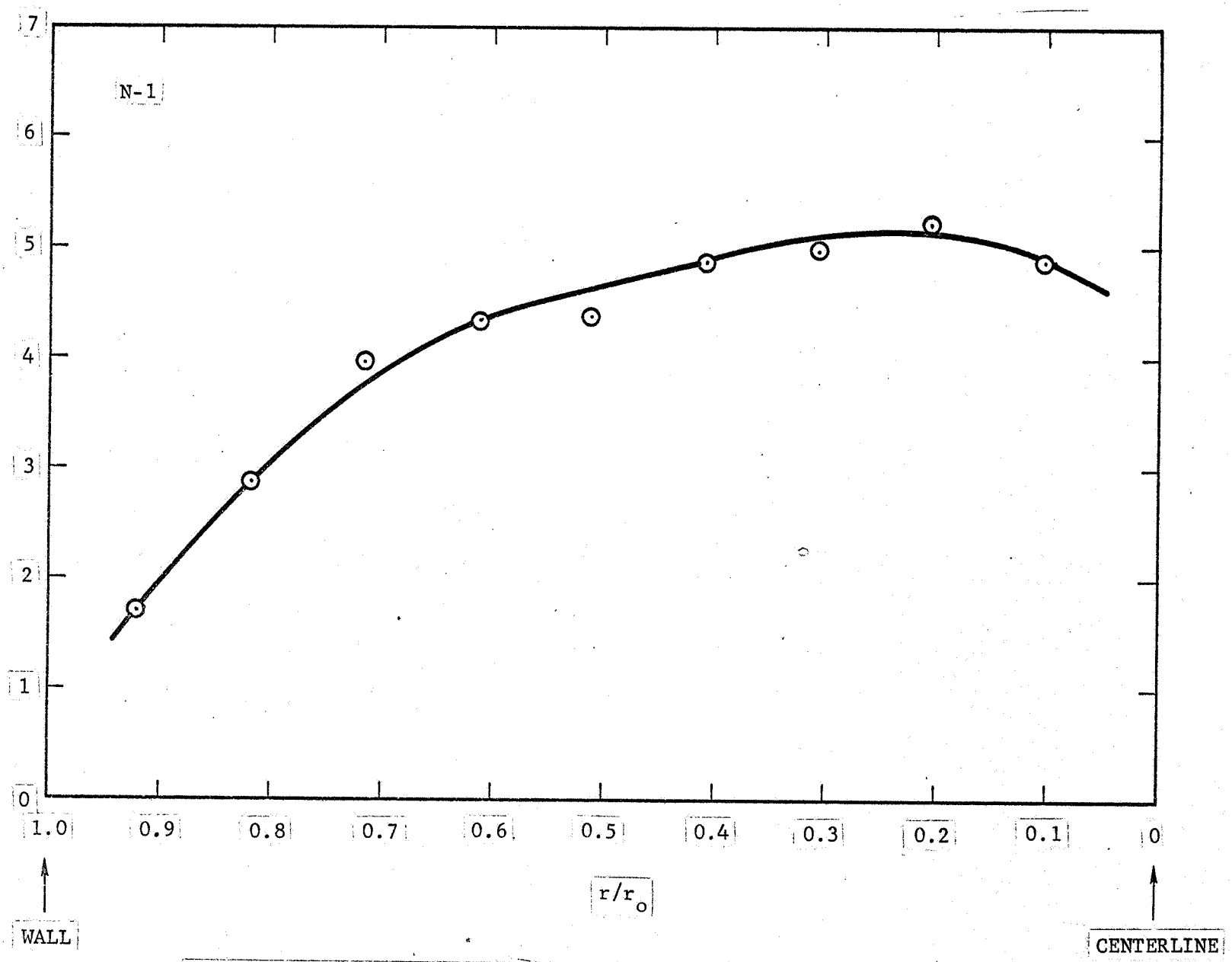

FIGURE 38. EDDY DIFFUSIVITY FOR HEAT TRANSFER AS A FUNCTION OF RADIAL POSITION (EXPERIMENT N-1)

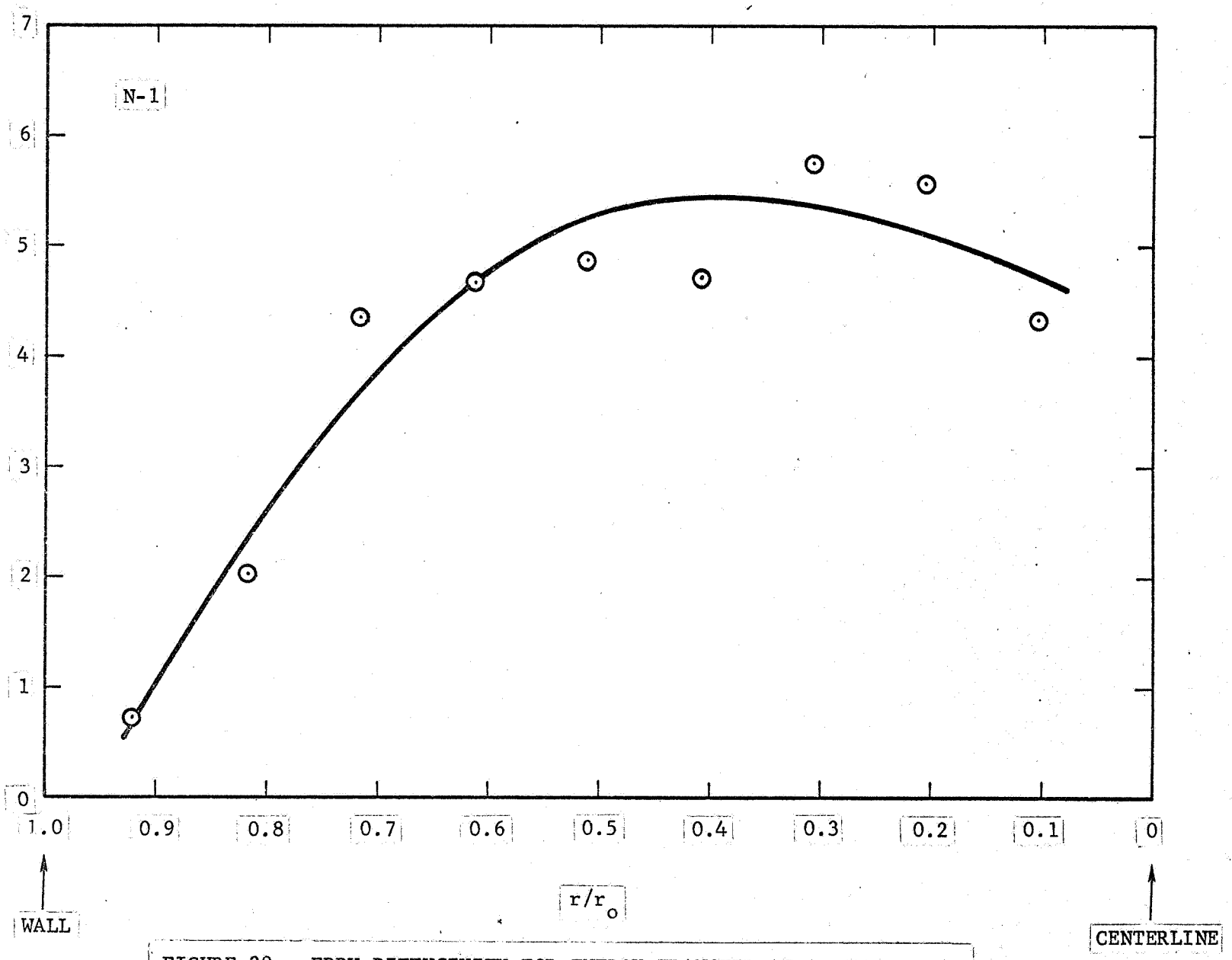

FIGURE 39. EDDY DIFFUSIVITY FOR ENERGY TRANSFER AS A FUNCTION OF RADIAL POSITION (EXPERIMENT N-1)

systems in channel flow (53)*. A comparison of ϵ_H and ϵ_H' with ϵ_M is shown in Figure 40. The results show that the ratio in eddy diffusivities is, over much of the cross section of the flow conduit, on the order of one, again suggesting an analogy. However, $\epsilon_H/\epsilon_M \sim 0.4$ to 0.7, while for air flow between parallel plates (with Prandtl number approximately the same), the ϵ_H/ϵ_M ratio is $\sim$ 1.1 to 1.3 (52,p.440). Thus the ratio in ϵ_H/ϵ_M obtained for N-1 is approximately one-half of the value measured for comparable nonreacting flows. This difference in eddy diffusivity ratio offers indirect evidence for the effect of the turbulent mixing process on the time-average reaction rate.

3.11 TURBULENT TEMPERATURE RESULTS — NONREACTING AND NONEQUILIBRIUM REACTING SYSTEMS

Total rms temperature intensity data for the nonreacting air system (Experiment A-37) measured with the system described in Section 2.3.3 is given in Figure 41. The usual minimum at the center of the pipe, the maximum values near the walls, and the intensity level on the order of 3% is consistent with the limited number of published results (54)(39) for air under conditions of fully developed turbulent pipe flow with heat transfer.

The very surprising results obtained for the nonequilibrium reacting NO_2 system (key pertinent experimental conditions are given on the figures themselves) are shown in Figures 42 and 43. In the case of these experiments, the variation of intensity with radial position is the same as in the case of the nonreacting system results, but the presence of the nonequilibrium chemical reaction has caused a more than order of magnitude increase in the intensity level. A mixing model for the interpretation of these results has not yet been developed (see Section 1.1). The large change in level cannot be primarily due to the difference in thermal properties between the two systems, since the N_{Pr} and N_{Le} parameters are

*The lines drawn through the data points are shown only to assist in discerning the trend of the data with radial position.

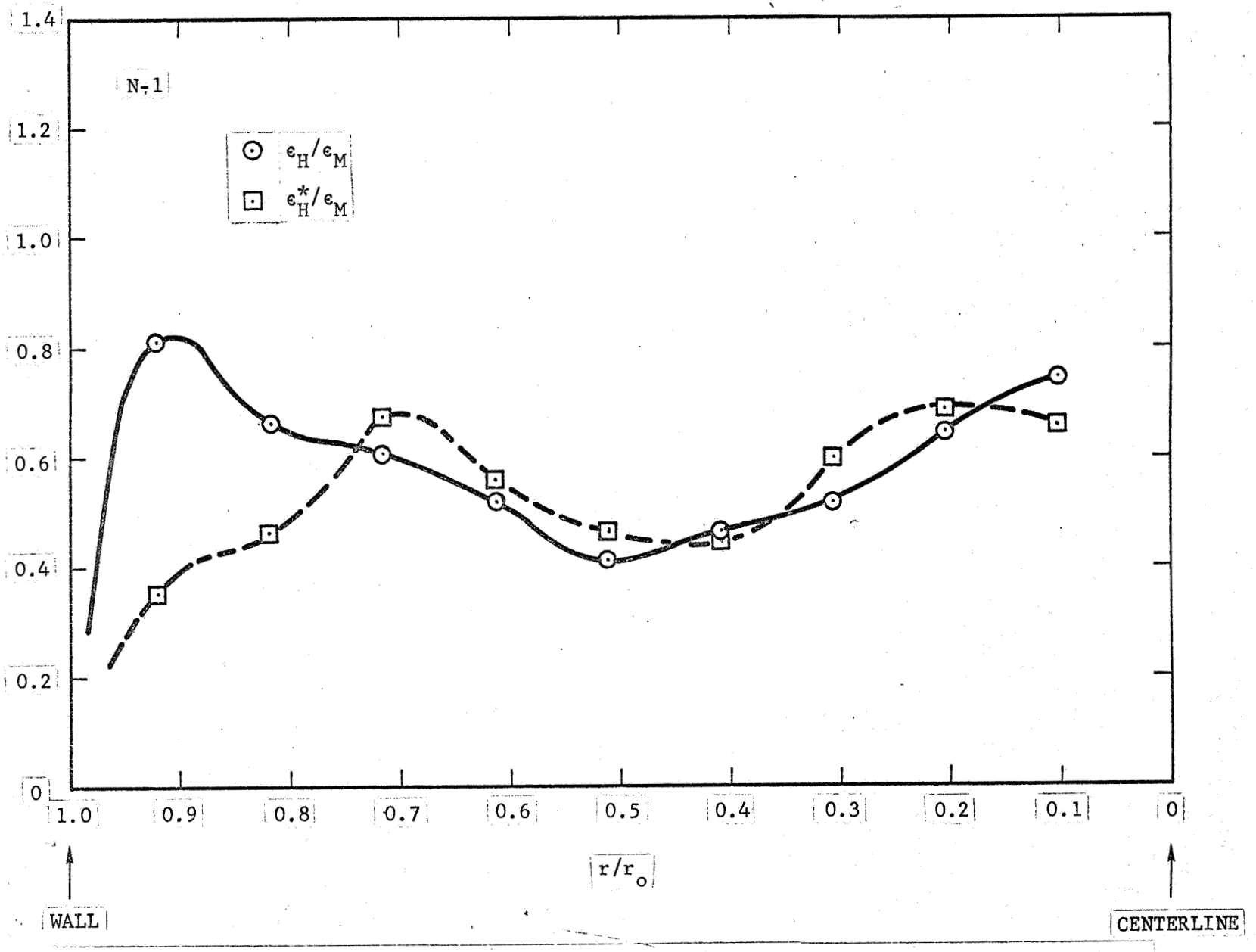

FIGURE 40. RATIO OF EDDY DIFFUSIVITIES AS A FUNCTION OF RADIAL POSITION (EXPERIMENT N-1)

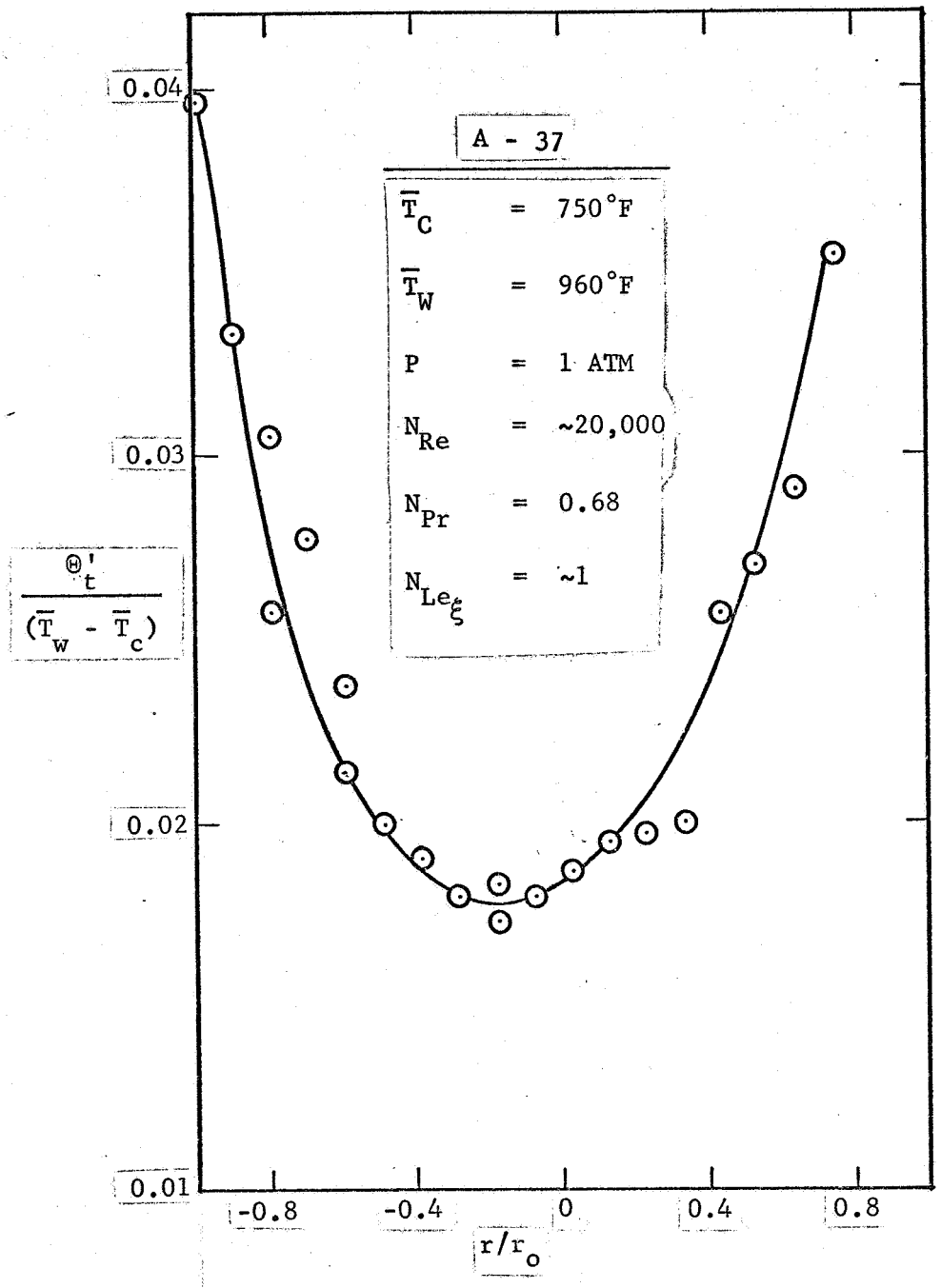

FIGURE 41. TOTAL RMS TEMPERATURE INTENSITIES AS A FUNCTION OF RADIAL POSITION (EXPERIMENT A-37)

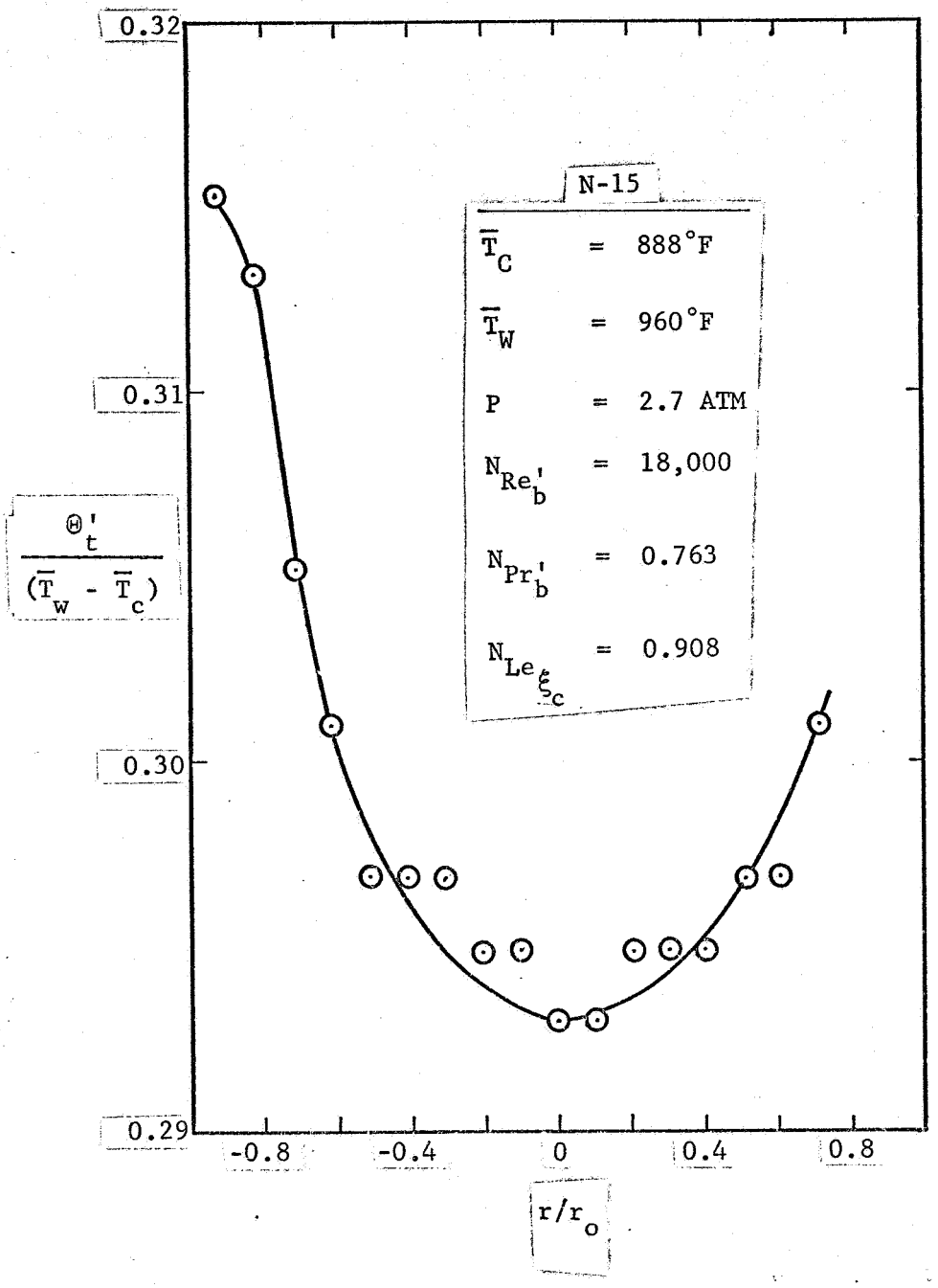

FIGURE 42. TOTAL RMS TEMPERATURE INTENSITIES AS A FUNCTION OF RADIAL POSITION (EXPERIMENT N-15)

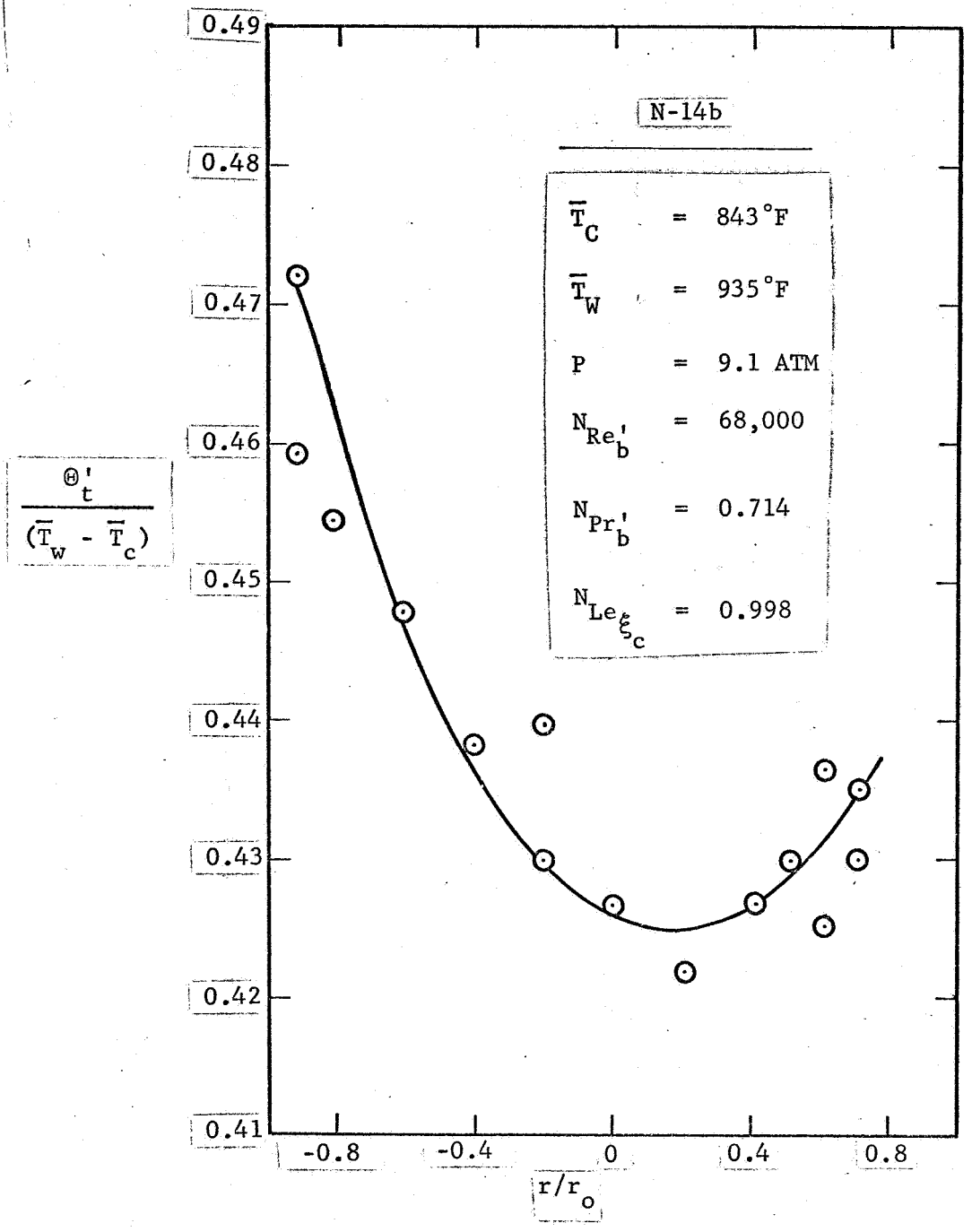

FIGURE 43. TOTAL RMS TEMPERATURE INTENSITIES AS A FUNCTION OF RADIAL POSITION (EXPERIMENT N-14b)

so similar. (Also, the difference in mass density between A-37 and N-15 is no more than ~ 3.) The values reported in Figures 41, 42, and 43 were obtained by either directly reading the dial of the true rms voltmeter or by recording the dc output of the rms voltmeter on a strip chart recorder and then estimating the mean of the rms output. More accurate time averaging (as indicated in Figure 20 — use of the voltage to frequency converter and counter in tandem) of the total rms output would be expected to yield more accurate profile results.

The scalar mixing spectrum for temperature obtained with air at high temperature in the recirculating flow system is shown in Figure 44. The extended slope in the inertial subrange (the essentially straight line region) is probably due to the coexistence of both longitudinal and radial (or transverse) mixing at the sensor location. Longitudinal mixing effects would be expected to arise from the 1 foot long heaters situated along the test section, each pulsing on and off in a random fashion at a frequency between once per second to once per 5 minutes depending on the cooling and heating loads imposed on the system. Thus the energy contributed to the spectrum from longitudinal mixing effects will be characterized by low frequencies and will thus tend to extend the inertial subrange over a greater frequency range than the usual one to one and one half decades of frequency (or one dimensional wave number).* This extension probably accounts for the slope of the spectrum in the inertial subrange not equalling the expected -5/3 (27). For reference the characteristic frequencies based on both the test section diameter ($\sim$ characteristic for transverse mixing), f_D, and the test section length, $f_{\ell_{TS}}$, are given on Figure 44. The conditions of the experiment are also given there for reference purposes.

Temperature spectrum data for two different NO_2 experiments are given in Figures 45, 46, and 47. The presentation of the data is in a form

---

*Terms are defined in the Nomenclature; some pertinent relations are given in Appendix A-1.

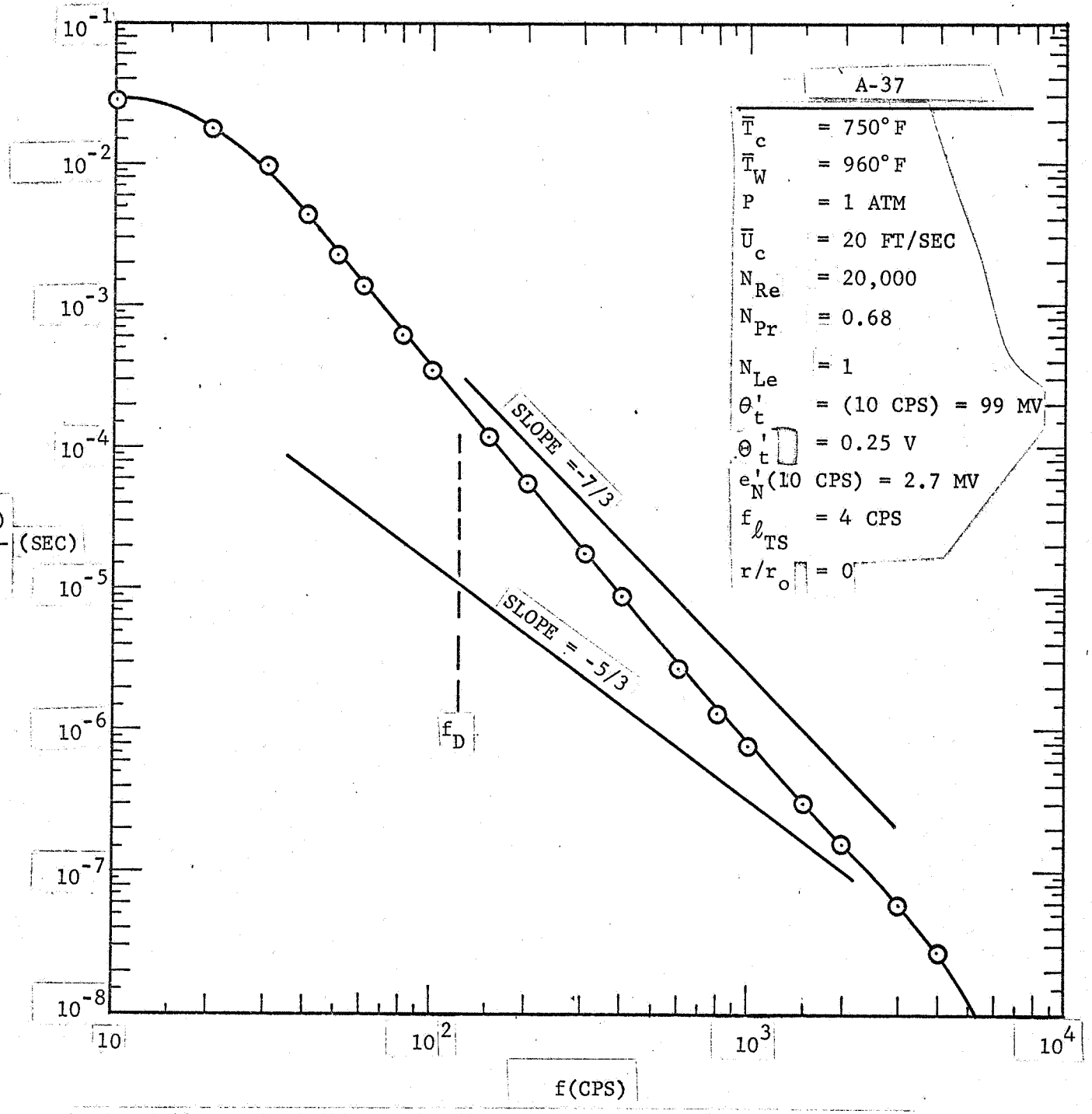

FIGURE 44. SCALAR MIXING SPECTRUM - TEMPERATURE (EXPERIMENT A-37)

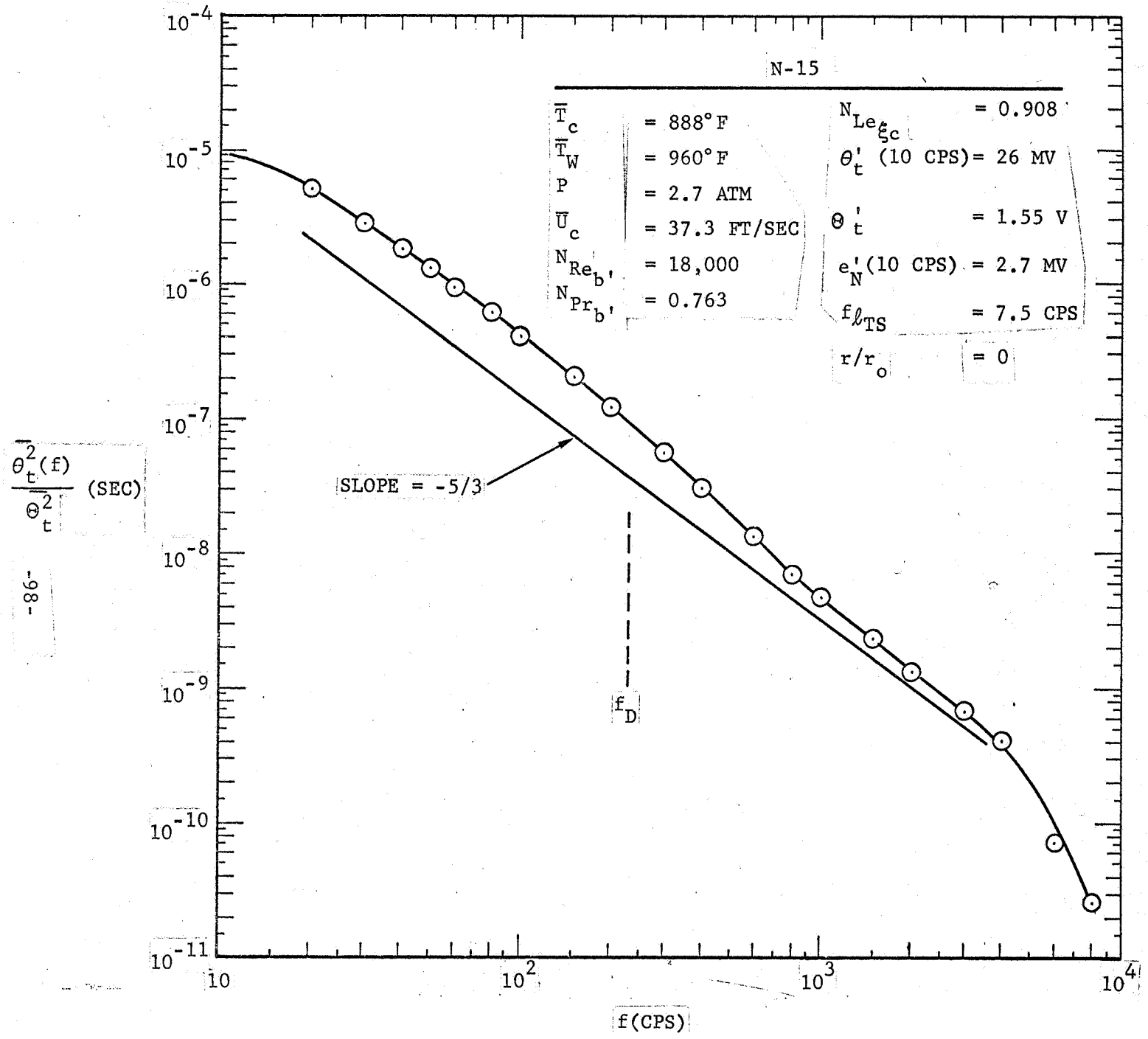

FIGURE 45. SCALAR MIXING SPECTRUM - TEMPERATURE (EXPERIMENT N-15)

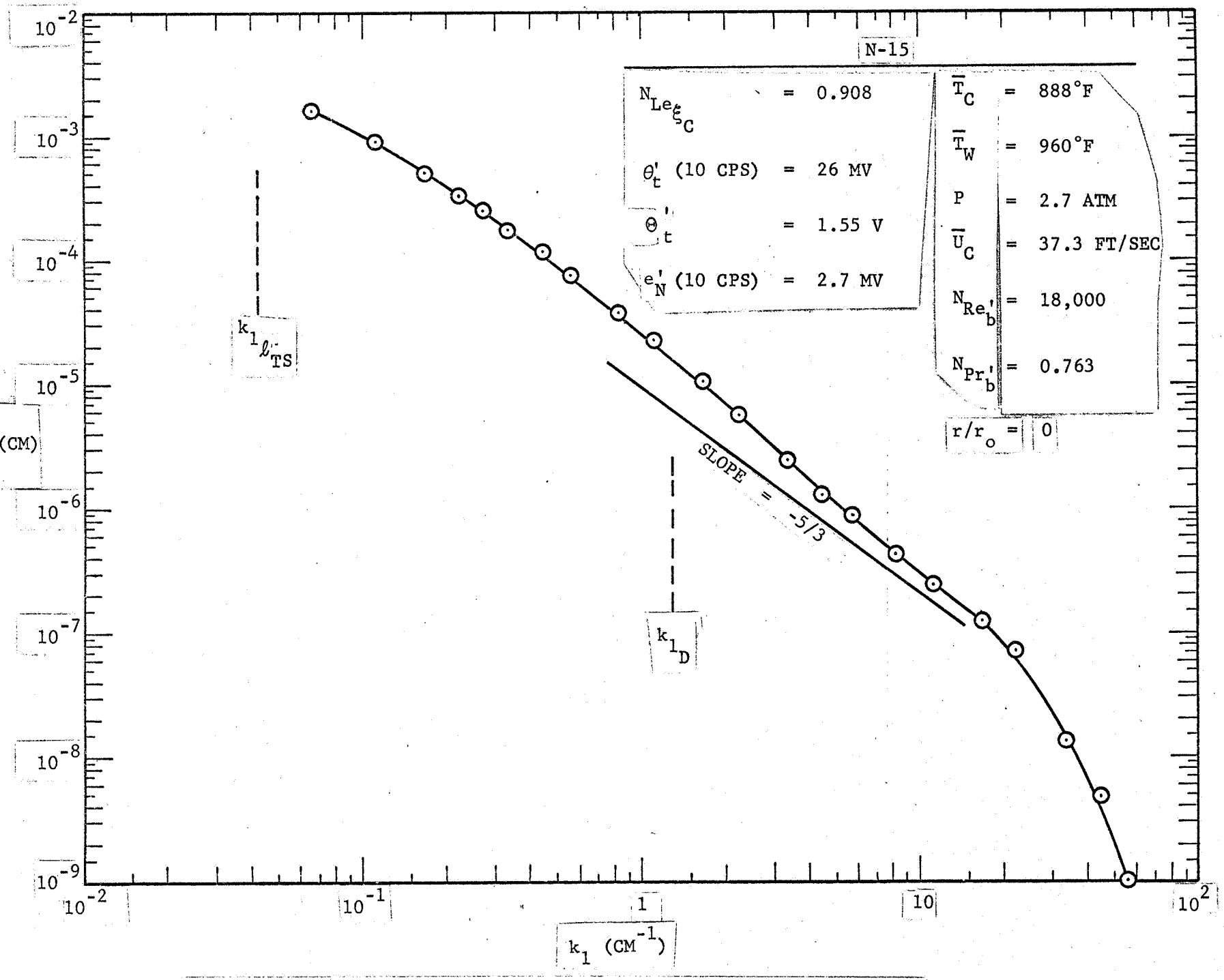

FIGURE 46. SCALAR MIXING SPECTRUM - TEMPERATURE (EXPERIMENT N-15)

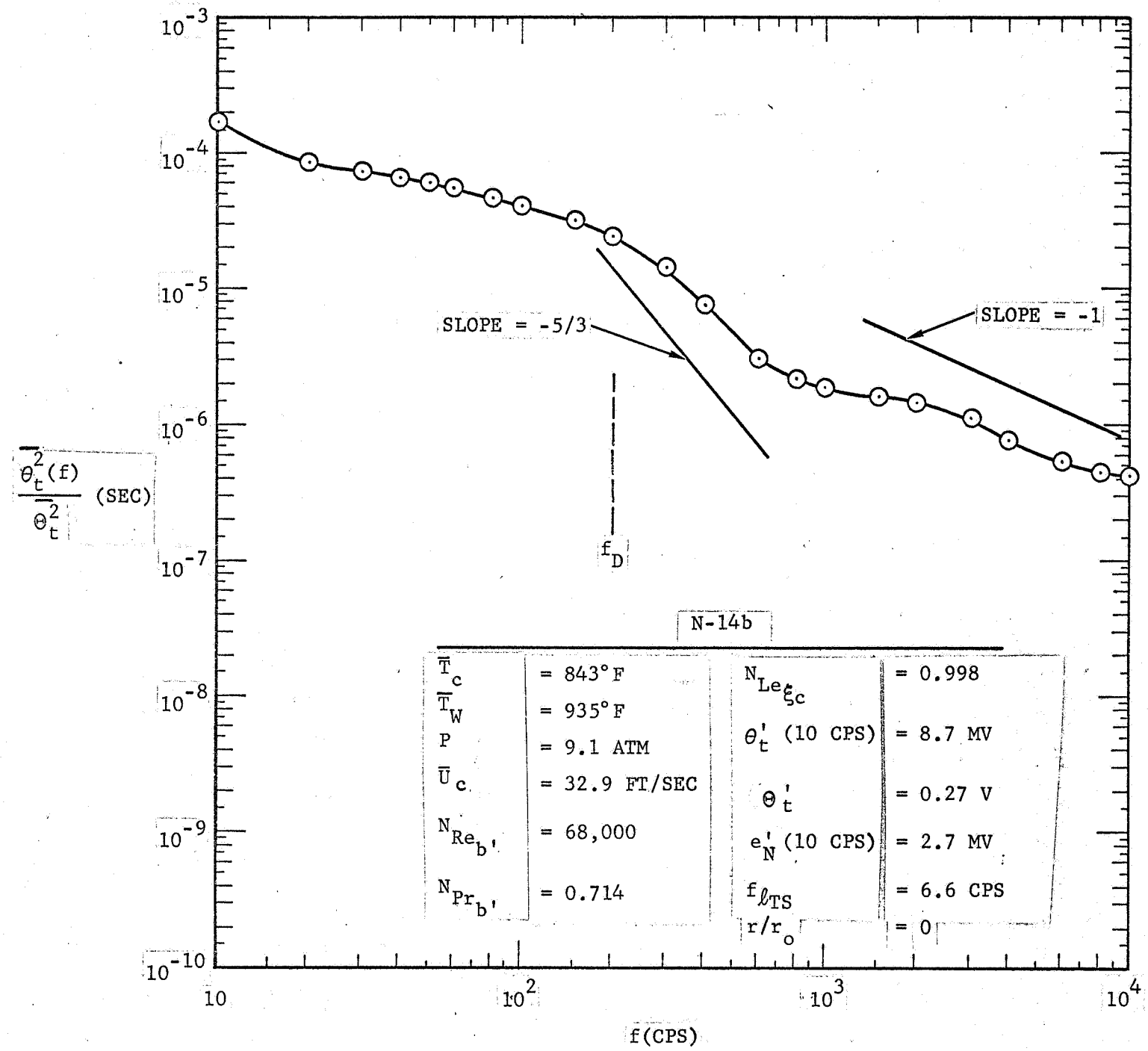

FIGURE 47. SCALAR MIXING SPECTRUM - TEMPERATURE (EXPERIMENT N-14b)

quite similar to that used in Figure 44 except that the NO_2 data obtained at frequencies greater than f_D (or k_{1_D}) which appear to lie in the inertial subrange exhibit, in each case, a slope very close to the characteristic -5/3. The data of Experiment N-15 are shown in the one-dimensional wave number form in Figure 46. The apparent diffusive cutoff at higher frequencies on the order of 10 k Hz may be due more to a start in the fall-off in frequency response of the probe [estimated to be better than 10 k Hz in (39)] than due to the start of a diffusive subrange. In Figure 47, the region exhibiting a -1 slope may be representative of a viscous-convective subrange. In this experiment (N-14b), there was very little turning on and off of the temperature controllers during the period of the turbulence measurements as compared with the other experiments (N-15 and A-37). This may help to explain why the N-14b spectrum results do not exhibit the extended inertial subrange to very low frequencies (the frequency response of the electronics instrumentation is good down to only 20 Hz). In any event, the spectra do not exhibit any unusual characteristics that cannot be ascribed to the nature of the experiment and/or equipment.

3.12 TURBULENT CONCENTRATION RESULTS

The total rms intensity data and the spectral data for the NO_2 experiment, N-14b, is tabulated in Tables 15 and 16. The format of these tables has been arranged so that the steps employed in the reduction of the raw data to the results of interest are evident. The intensities have been calculated assuming that the equilibrium time-average concentration difference based on the measured temperature difference $(\overline{T}_w - \overline{T}_c)$ is a reasonable measure of the actual nonequilibrium time-average concentration difference $\left[\left(\overline{C}_{NO_2}\right)_c - \left(\overline{C}_{NO_2}\right)_w\right]$.* The intensity results are shown in Figure 48. Consistent with the unusually large temperature intensity data given in Figures 42 and 43 for the NO_2 reacting system, the concentration intensity values are also large. In fact, in the case of this experiment,

*A good measure of $\left(\overline{C}_{NO_2}\right)_w$ was not experimentally obtained.

TABLE 15. TOTAL RMS CONCENTRATION INTENSITIES AS A FUNCTION OF RADIAL POSITION

(Experiment N-14b)

r/r_o	$\left[(e'_{S+N})_{NO_2}\right]$ (millivolts)	$(e'_S)_{NO_2}$ (mv)	$\left[(e'_S)_{Air}-(e'_S)_{NO_2}\right]$ (mv)	$b^{-1}_{NO_2}$ $\left(\frac{moles}{liter}\right)$	$\overline{E}$ (volts)	$\Theta'_{C_{NO_2}} \times 10^3$ $\left(\frac{moles}{liter}\right)$	$\frac{\Theta'_{C_{NO_2}}}{\left[\left(\overline{C}_{NO_2}\right)_{e_c}-\left(\overline{C}_{NO_2}\right)_{e_w}\right]}$
+1.00	3.33	3.156	17.814	0.1493	1.190	22.35	0.905
+0.9	3.33	3.156	17.814	0.1469	1.182	22.14	0.896
+0.8	3.30	3.125	17.845	0.1466	1.180	22.16	0.897
+0.6	3.27	3.093	17.877	0.1465	1.162	22.54	0.913
+0.4	3.30	3.125	17.845	0.1465	1.151	22.71	0.919
+0.2	3.30	3.125	17.845	0.1464	1.127	23.17	0.938
0	3.33	3.156	17.814	0.1464	1.120	23.28	0.943
-0.2	3.33	3.156	17.814	0.1464	1.109	23.52	0.952
-0.4	3.33	3.156	17.814	0.1465	1.091	23.92	0.968
-0.6	3.33	3.156	17.814	0.1465	1.097	23.79	0.963

(e'_N) = 1.06 millivolts.

$(e'_{S+N})_{Air}$ = 21 millivolts.

$(e'_S)_{Air}$ = 20.97 millivolts.

$\left(\overline{C}_{NO_2}\right)_{e_c}$ = 0.0884 moles/liter.

$\left(\overline{C}_{NO_2}\right)_{e_w}$ = 0.0637 moles/liter.

TABLE 16. CONCENTRATION SPECTRUM (Experiment N-14b)

f (cps)	$(e'_{S+N})_{f_{Air}}$ (mv)	$(e'_{S+N})_{f_{NO_2}}$ (mv)	$(e'_N)_f$ (mv)	$(e'_S)_{f_{Air}}$ x 10^2 (mv)	$(e'_S)_{f_{NO_2}}$ x 10^2 (mv)	$\overline{\theta^2_{C_{NO_2}}}(f)$ x 10^8 [(moles/liter)^2 sec]	$\overline{\theta^2_{C_{NO_2}}}(f)/\overline{\Theta^2_{C_{NO_2}}}$ x 10^6 (sec)
10	0.677	0.1580	0.0152	67.68	15.72	8.523	3.624
20	0.675	0.1575	0.0118	67.49	15.69	8.471	3.602
30	0.672	0.1570	0.0107	67.19	15.66	8.383	3.564
40	0.670	0.1565	0.0100	66.99	15.61	8.334	3.543
50	0.667	0.1560	0.0095	66.69	15.57	8.250	3.508
60	0.665	0.1555	0.0089	66.49	15.52	8.202	3.487
80	0.662	0.1550	0.0083	66.19	15.47	8.121	3.453
100	0.660	0.1545	0.0077	65.99	15.43	8.070	3.431
150	0.650	0.1530	0.0072	64.99	15.28	7.801	3.317
200	0.647	0.1510	0.0068	64.69	15.08	7.770	3.304
300	0.646	0.148	0.0067	64.59	14.78	7.833	3.330
400	0.643	0.145	0.0066	64.30	14.49	7.833	3.330
600	0.638	0.140	0.0065	63.80	13.98	7.836	3.332
800	0.629	0.135	0.0062	62.90	13.48	7.710	3.278
1,000	0.621	0.130	0.0060	62.10	12.99	7.614	3.237
1,500	0.592	0.120	0.0058	59.19	11.98	7.036	2.991
2,000	0.564	0.0960	0.0053	56.39	9.585	6.918	2.941
3,000	0.500	0.0857	0.0045	49.99	8.558	5.419	2.304
4,000	0.432	0.0753	0.0044	43.20	7.517	4.019	1.709
6,000	0.315	0.0612	0.0030	31.50	6.012	2.051	0.8720
8,000	0.245	0.0490	0.0025	24.49	4.894	1.213	0.5157
10,000	0.210	0.0375	0.0020	20.99	3.744	0.9395	0.3994

BW = 5.52 cps.

b_{NO_2} @ $r/r_o \simeq -0.2$ (Profile C-4) = 6.83 liters/mole.

(ϵ = 283.04 liters/mole cm; ℓ = 0.02413 cm).

$\overline{E}$ = 1.109 volts = 1109 millivolts.

$\overline{\Theta^2_C}$ at $r/r_o \simeq -0.2 = 23.52 \times 10^{-3}$ (moles/liter).

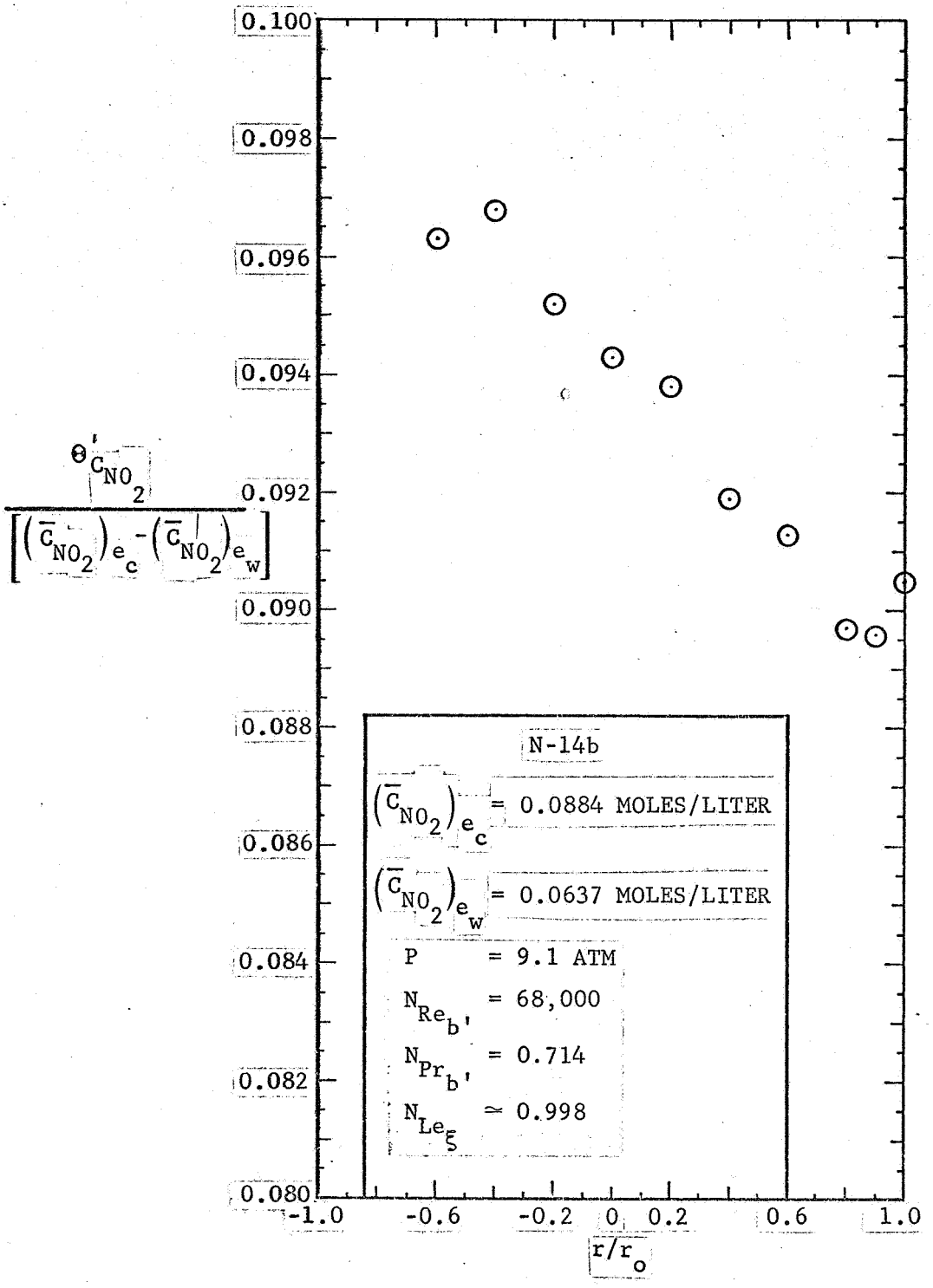

FIGURE 48. TOTAL RMS CONCENTRATION PROFILE AS A FUNCTION OF RADIAL POSITION

the average concentration intensity across the pipe was ~ 93% or approximately twice as large as the temperature intensities. The data in Figure 48 are plotted with a greatly expanded ordinate. Considering the accuracy of the measurement [limitations from boundary layer buildup on the ends of the fiber bundles — expected to be a small effect (45), slight change in flow conditions during the course of the experiment, etc.], the results given in Figure 48 should be interpreted as indicating that the intensity is essentially constant across the pipe (within ± 4%).

Lee (30) has made some interesting predictions, based on a statistical turbulence theory treatment, of how the turbulent concentration mixing spectra of an isotropic flow (one reactant; irreversible, second order reaction) depends on the turbulence Peclet number, $N_{Pe}^{(t)}$, and the turbulence Damkohler number (of the second type), $N_{Da_{II_i}}^{(t)}$. We have calculated these parameters for the conditions representative of most of the NO_2 experiments (including N-14b) and find for,

$$\Theta_u' \sim 0.10\ \overline{U}_c \quad \text{[From (51,p.521-522)]} \tag{19}$$

with,

$$\overline{U}_c \sim 40 \text{ ft/sec}$$

$$\overline{D} \sim 0.2 \text{ cm}^2/\text{sec}$$

$$k_{1_D} \sim 1.3 \text{ cm}^{-1}$$

then,

$$N_{Pe}^{(t)} \sim 490$$

and,

$$N_{Da_{II_{NO_2}}}^{(t)} \simeq 8.9$$

so that the ratio $N_{Da_{II_{NO_2}}}^{(t)}/N_{Pe}^{(t)} \sim 0.02$ and thus, according to Lee's analysis, the NO_2 dissociation is a "slow" reaction. His results may be useful in interpreting our results to the extent that the flow field of our spectrum experiments (sensing probe tip at the center of a fully developed turbulent tube flow) and the chemistry of the NO_2 dissociation

conform to the assumptions embodied in his model.

In Figure 49, the concentration spectrum for Experiment N-14b is shown for the frequency range 10 to 10^4 Hz (data were obtained out to 15 k H_z). The solid line drawn through the data is shown in order to assist in discerning its variation with frequency. The results indicate that what might be considered an inertial subrange begins only at frequencies much greater than f_D. Most of the energy of the concentration spectrum is distributed uniformly across 2½ decades of frequency with fall-off occurring only at comparatively high frequencies. Additional experiments should be carried out with probes with significantly different gap widths, ℓ, in order to determine if the shape of the concentration spectrum is more probe geometry-limited or phenomena-limited.

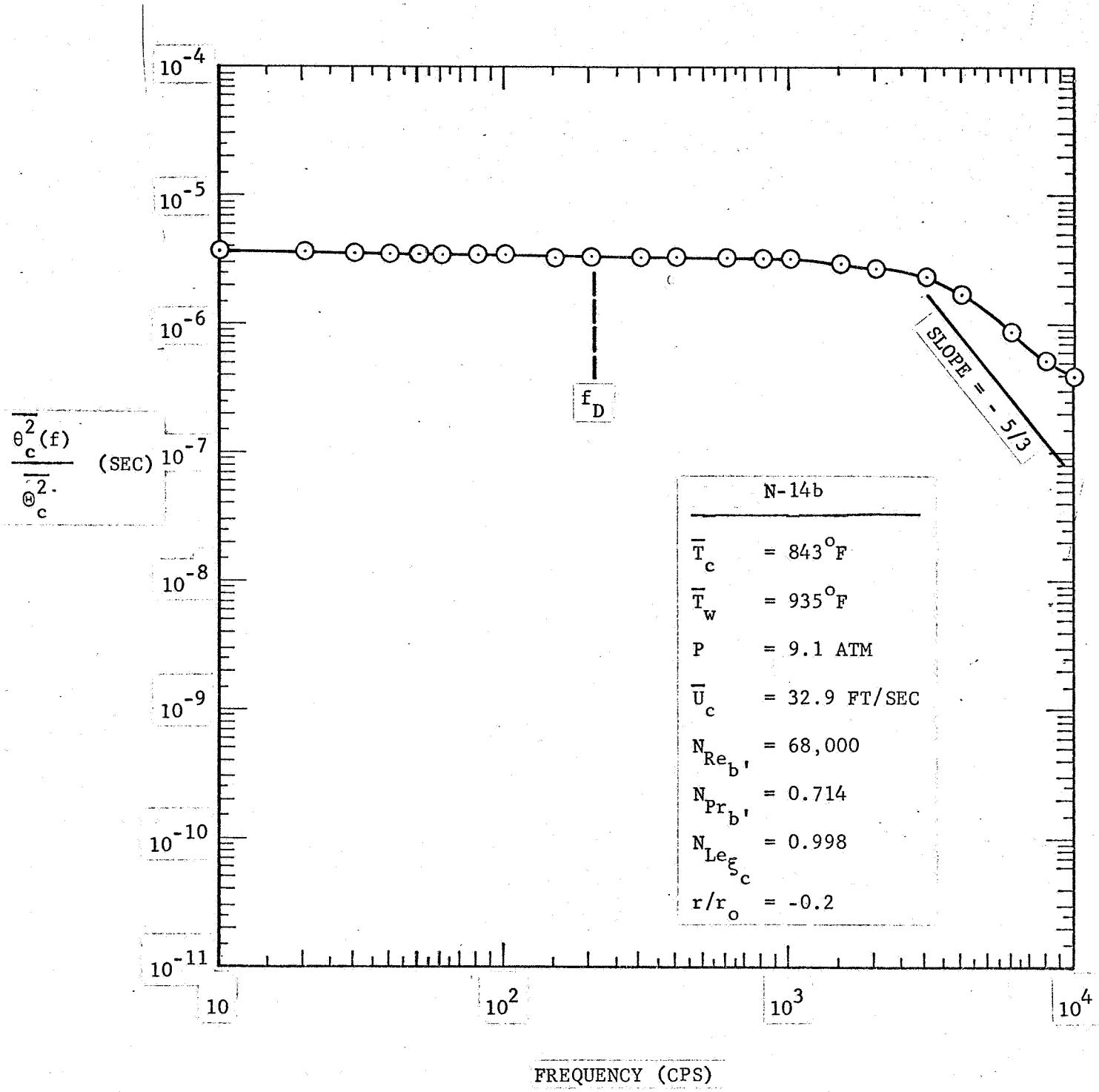

FIGURE 49. CONCENTRATION SPECTRUM (EXPERIMENT N-14b)

SECTION 4

CONCLUSIONS

4.1 EXPERIMENTAL RESULTS

This investigation is the first known attempt to obtain both time-average and fluctuating radial profile measurements in nonequilibrium reacting turbulent tube flow with heat transfer. In order to make these measurements, a number of problems had to be solved. These included: (a) the selection of a reacting system whose kinetics were homogeneous and unaffected by the materials required for construction of the flow system and the sensing ends of the instrumentation, (b) the determination of all of the required property data (thermodynamic, transport, kinetic, and optical absorption) over the ranges of temperature and pressure required for the experimental measurements, (c) the design, fabrication, and checkout of a large recirculating flow system capable of handling a toxic, corrosive gas at elevated temperatures and pressures with negligible leakage of the gas or appreciable deterioration of the system itself after extended periods of operation, (d) the design of a rotating shaft seal compatible with the system requirements (temperature, pressure, flow rate, period of operation), (e) the design, checkout, and calibration of appropriate fast response, low noise, small spatial resolution temperature and concentration probes compatible with the system requirements and capable of providing the desired time-average and fluctuating information, and finally (f) the development of techniques for operation of both the flow system and the associated instrumentation so that the desired results could be obtained. During the course of this program these, and many lesser problems were solved.

The reduction of experimental data itself and its comparison to the predictions of available models revealed the following (for details, reference should be made to the appropriate portions of Section 3):

a. As expected, the presence of a nonequilibrium homogeneous reaction has little, if any, significant effect on the momentum transport situation for the conditions investigated

b. Conventional heat transfer correlations are inadequate for correlating fully developed turbulent tube flow heat transfer data when a nonequilibrium reaction occurs in the flow

c. The only available model (Model II - see Section 1.1) for predicting "heat" transfer coefficients for such situations is, in principle, inadequate in four principal ways:

   (1) the temperature difference between the wall and the bulk of the flow is assumed to be small, and in addition equilibrium fluid properties are assumed applicable

   (2) the time-average reaction rate is assumed to be independent of longitudinal position after a certain "starting" length

   (3) the eddy diffusivities for energy, mass, and momentum transport are assumed to be equal to each other and equal to the eddy diffusivity for momentum transport measured in nonreacting flow

   (4) the time-average reaction rate is assumed to depend only on the time-average temperature and composition, but it is known (55)(56) that in the case of second and higher order reactions (as is the case for the relatively slow NO_2 decomposition) the time-average reaction rate, in a turbulent flow, depends on the usual time-average quantities multiplied by a factor

equal to one plus the concentration intensity squared (for concentration intensities greater than 30%, the effect of the turbulence in the flow on the reaction rate is such as to increase the time-average reaction rate by greater than 10%).

The experimental data showed that even if a correction is made for the finite ΔT which occurs in any actual "heat" transfer situation, the theoretical predictions and the experimental data do not agree for three principle reasons:

a. Evaluation of the bulk properties assuming equilibrium leads to significant errors because the bulk region is sufficiently far from an equilibrium state

b. Though an analogy between energy and momentum transport is suggested (within a factor of three), the eddy diffusivities are not equal and, in fact, are different from each other, by a factor of two

c. The actual time-average reaction rate is much greater than the one assumed to depend only on the time-average temperature and composition

Points a. and c. are expected to be the major reasons for the discrepancies between the experimental data and the predictions of the theoretical model.*

The principal reason why it now appears that point c. does lead to large errors in the predictions of the model is that the experimental data show that the turbulent fluctuation intensities of both concentration and temperature can be <u>much larger</u> in nonequilibrium reacting shear flows than in corresponding nonreacting shear flows.

---

*The data obtained for turbulent flow outside a rotating cylinder deviates about the same amount from the predictions of the model (IV) as was found for the tube flow data.

4.2 AREAS REQUIRING FURTHER INVESTIGATION

The principal areas requiring further investigation can be summarized as follows:

a. Revision of the model to make it both a reliable predictive tool and more faithful to physical reality (remove $\Delta T \rightarrow 0$ restriction, modify the bulk and wall boundary conditions so that even though nonequilibrium conditions actually prevail at these "boundaries," only equilibrium and/or frozen fluid properties are required in order to apply the revised model for the prediction of turbulent heat transfer rates in nonequilibrium tube flow, use a time-average reaction rate dependent on a correlation of the turbulent concentration intensity data, use eddy diffusivities that approximate the experimental results)

b. Measurement of time-average energy, mass, and momentum transport data (φ, $\sqrt{m}$, etc.) over a wider range of Damkohler numbers with the following features: measurement of time-average concentration at the wall, measurements as a function of longitudinal position, calculation of eddy diffusivities using both radial and longitudinal data, measurements for both constant wall heat flux and isothermal wall cases, use of <u>in situ</u> heat flux gauges in the test section walls, and modification of the optical probe sensing end so that it points upstream with reduced fiber bundle diameters in the tip region

c. Measurement of both turbulent temperature and concentration data over a wide range of Damkohler numbers (frozen to equilibrium conditions)

d. Develop a mixing model, based on the experimental results obtained in part c., which predicts the unusually large

increase in turbulent intensities which have now been observed.

These areas have been confined to the fully developed turbulent tube flow case primarily because of the practical importance of such a flow geometry. Of course, the effect of chemical reaction rates on transport in the case of other flow geometries should also be explored.

ACKNOWLEDGMENTS

We are indebted to Dr. James E. Danberg (Headquarters) and Dr. Richard S. Brokaw (Lewis Research Center) of NASA for their support throughout this program. Dr. Brokaw minimized our problems in obtaining for us most of the NO_2 property data used in processing the experimental data.

A number of our colleagues deserve recognition for the many contributions they have made to this difficult and demanding program. Mr. H. Russell Harmon was primarily responsible for redesigning and rebuilding the rotating mechanical shaft seal of the turboblower so that it would seal NO_2 at 730°F and 11 atm for extended periods of time. Dr. Donald L. Peters assisted in the design of the piping and heating system. Mr. Rodger W. Baier and Mr. Walter B. Barker carried out the heterogeneous kinetics measurements. Mr. Duane G. Piper carried out the machine computations for Model II using the $N_{Le} = 1$ program graciously loaned to us by Dr. P.L.T. Brian (MIT). Messrs. Richard W. Lindberg, Jerold C. Ososkie, Donald D. Pinsky, James G. Myers, and A. G. Chartier were especially helpful in the design, fabrication, and checkout of the optical probe system. Several members of the Applied Chemistry Department provided assistance on various experiments. In particular, we are grateful for the assistance of Mr. Gilbert Segovia, Mr. David E. Breen, Dr. William Baerg, and Mr. John C. Britt. We also are appreciative of the compositional competence of Mrs. Stephanie W. Maguire and the continual encouragement and support of Dr. Henry Shanfield.

NOMENCLATURE

a	=	proportionality constant relating the light intensity incident on the end of the photomultiplier tube to the resulting voltage output of the tube (intensity/volts)
A	=	heat transfer area (ft^2)
b_i	=	product of extinction coefficient and transmitted light path length $\equiv \epsilon_i(\lambda,T)\ell$ (gm moles/liter)$^{-1}$
BS	=	designated turboblower setting as indicated by the dial on the varidrive
BW	=	band width of wave analyzer (cycles/second or Hertz)
C	=	conversion factor relating voltage output of thermocouple to sensed temperature (volts/^oF)
C	=	coefficient of discharge of orifice plate
C	=	total molar concentration of the gas system (moles/cm^3)
C_p	=	isobaric specific heat (BTU/lb_m ^oR)
d	=	diameter of orifice in orifice plate (ft)
d_p	=	probe diameter (inches)
D	=	pipe inside diameter (ft)
$\overline{D}$	=	averaged binary diffusion coefficient for NO_2-O_2 and NO_2-NO systems (cm^2/sec)
e	=	fluctuating voltage (volts)
e_{S+N}	=	fluctuating voltage with signal and noise information (volts)
e_N	=	fluctuating voltage with only noise information (volts)

E = voltage applied to heater at location of test probes (volts)

E = instantaneous voltage from the sample beam (volts)

E_o = instantaneous voltage from the reference beam (volts)

f = Fanning friction factor

f = frequency (cycles/second or Hertz)

f_D = frequency based on test section diameter and centerline axial flow velocity (Hz)

$f_{\ell_{TS}}$ = frequency based on test section length (5 ft) and centerline axial flow velocity (Hz)

g = local acceleration due to gravity (ft/sec^2)

g_c = gravitational constant = 32.17 lb_m ft/lb_f sec^2

G = mass flow rate ($lb_m/sec\ ft^2$)

G = gain of amplifier(s)

h = vertical displacement of liquid level in manometer (inches H_2O)

h = heat transfer coefficient defined by the equation

$$h \equiv \frac{Q}{T_w - T_b} \left(\frac{BTU}{ft^2 \cdot sec \cdot {}^oF}\right)$$

h' = heat transfer coefficient defined by the equation

$$h' \equiv \frac{Q}{H_w - H_b} \left(\frac{lb_m}{sec \cdot ft^2}\right)$$

h'' = heat transfer coefficient for reacting gases defined by the equation

$$h'' \equiv \frac{Q}{T_w - T_{b'}} \left(\frac{BTU}{ft^2 \cdot sec \cdot {}^oF}\right)$$

h''' = heat transfer coefficient defined by the equation

$$h''' \equiv \frac{Q}{H_{\xi_w} - H_b} \left(\frac{lb_m}{sec \cdot ft^2}\right)$$

h^* = heat transfer coefficient of a nonreacting gas (equivalent to h) $\left(\frac{BTU}{ft^2 \cdot sec \cdot {}^oF}\right)$

$$h^* = \frac{N^*_{Nu_f} \; k_\xi}{D}$$

with $N^*_{Nu_f} = 0.0245 \; N^{0.77}_{Re_f}$ for $N_{Pr_f} = 0.7$ (49)

H = specific enthalpy (BTU/lb_m)

$\Delta\tilde{H}_R$ = molar heat of reaction (cal/mole)

H^+ = normalized specific enthalpy defined by the equation

$$H^+ \equiv \frac{(H_w - H) \; \tau_w \; g_c}{Q_w \; (\tau_w \; g_c/\rho_w)^{\frac{1}{2}}}$$

$H^\dagger$ = activation enthalpy for the decomposition reaction $2 \; NO_2 \rightleftarrows 2 \; NO + O_2$ equal to 26,900 cal/mole of NO_2

I = current through heater at location of test probes (amps)

I = light intensity transmitted through the gap of absorbing gas (intensity)

I_o = incident light intensity (intensity)

J_{i_r} = mass flux of species i in the radial direction due to molecular processes; relative to the mass-average velocity in the radial direction (gm/cm^2 sec)

$J_{i_r}^{(t)}$ = mass flux of species i in the radial direction due to both molecular and turbulent transport processes; relative to the mass average velocity in the radial direction (gm/cm^2 sec)

k = thermal conductivity ($BTU/ft \cdot hr \cdot {}^oF$)

k_D = forward specific reaction rate constant used by Rosser and Wise (33) (see Eq. A-13) ($cm^3/mole \cdot sec$)

k_{F_B} = forward specific reaction rate constant used by Bodman (21)(26) (see Eq. A-14) (related to partial pressures) ($mole/sec \cdot cm^3 \cdot atm^2$)

k_1 = one-dimensional wave number (cm^{-1})

k_{1_D} = one-dimensional wave number based on test section diameter (cm^{-1})

$k_{1_{\ell_{TS}}}$ = one-dimensional wave number based on test section length (5 ft) (cm^{-1})

k_R = reverse specific reaction rate constant (see Eq. A-15) ($cm^6/mole^2$ sec)

k_{R_B} = reverse specific reaction rate constant used by Bodman (21) (26) (see Eq. A-14) (related to partial pressures) ($mole/sec\ cm^3\ atm^3$)

k_w = assumed first order heterogeneous decomposition rate for NO_2 (sec^{-1})

K = flow coefficient for an orifice plate defined by the equation

$$K \equiv \frac{C}{\sqrt{1 - \beta^4}}$$

K = distance from pressure port to upper level of manometer fluid (in)

ℓ = estimate of the momentum boundary layer thickness approximated by

$$\ell \approx \frac{D_i}{0.0276\ N_{Re_{f'}}^{0.77}\ N_{Pr_{f'}}^{1/3}} \quad \text{(cm)}$$

ℓ = gap width of optical probe (cm)

ℓ_{TS} = length of center test section = 5 feet

L = length of heater or distance between static pressure ports; distance in axial direction (ft)

m_c = designates a measure of the ratio of the characteristic time for diffusion to the characteristic time for chemical reaction defined by the equation (evaluated at centerline conditions)

$$m_c \equiv \frac{k_{F_{B_c}}\ p^2\ (x_{NO_2})_c^2\ k_{\xi_c}^2 \left[\frac{3}{\xi(1-\xi)}\right]_c}{C_c\ \overline{D}_c\ (h^*)_c^2} \quad (h^* \text{ based on } N_{Re_c} \text{ and } N_{Pr} = 0.7)$$

m = mass velocity (lb_m/sec)

$\overline{m}$ = m modified for an energy transfer situation involving a finite temperature difference

$$\overline{m} \equiv m \exp\left[\frac{1}{(2/\lambda) + \mu}\right]$$

M = molecular weight (gm/gm mole)

$N_{D_{II_{NO_2}}}$ = Damkohler number of the second type for NO_2 defined by the equation: $N_{D_{II_{NO_2}}} \equiv \tau_D/\tau'_{C_{NO_2}} = [k_\xi^2/(h^*)^2\ \bar{D}](k_D\ C_{NO_2})$

$$N_{D_{II_{NO_2}}} \equiv m\ \frac{[\xi(2+\xi)]}{6}$$

$N^{(t)}_{Da_{II_{NO_2}}}$ = Damkohler number of the second type for NO_2 defined by

$$N^{(t)}_{Da_{II_{NO_2}}} \equiv \frac{k_D\left(\bar{C}_{NO_2}\right)_c}{\bar{D}\ k^2_{1_D}}$$

N_{Le_ξ} = frozen Lewis number defined by $N_{Le_\xi} \equiv \dfrac{C_{P_\xi}\ \rho\ D_{12}}{k_\xi}$

N_{Nu} = Nusselt number defined by $N_{Nu} \equiv h\ D/k$

$N'_{Nu_{b'}}$ = Nusselt number defined by $N'_{Nu_{b'}} \equiv h'\ D/(k/C_P)_{b'}$

$N'_{Nu_{f'}}$ = Nusselt number defined by $N'_{Nu_{f'}} \equiv h'\ D/(k/C_P)_{f'}$

$N''_{Nu_{f'}}$ = Nusselt number defined by $N''_{Nu_{f'}} \equiv h''\ D/k_{\xi_{f'}}$

$N'''_{Nu_{f'}}$ = Nusselt number defined by $N'''_{Nu_{f'}} \equiv Q\ D/(k/C_P)_{f'}(H_{\xi_w} - H_b)$

N^*_{Nu} = Nusselt number for nonreacting system defined by

$N^*_{Nu} \equiv h^*\ D/k_\xi$

$N^{(t)}_{Pe}$ = Peclet number defined by $N^{(t)}_{Pe} \equiv \Theta'_u/\bar{D}\ k_{1_D}$

N_{Pr} = Prandtl number defined by $N_{Pr} = C_P\ \mu/k$

N_{Re} = Reynolds number defined by $N_{Re} = DG/\mu$

N_{Sc} = Schmidt number defined by $N_{Sc} \equiv \mu/\rho\ \bar{D} = N_{Pr_\xi}/N_{Le_\xi}$

N_{St_c} = Stanton number defined by

$$N_{St_c} \equiv \frac{Q_w}{C_{P_c}\ \rho_w\ U_c\ (T_w - T_c)}$$

(time-average temperatures and velocity)

N'_{St_c} = modified Stanton number defined by

$$N'_{St_c} \equiv \frac{Q_w}{\rho_w U_c (H_w - H_c)}$$

(time-average specific enthalpies and velocity)

P = total system pressure (atm)

ΔP = pressure drop in system or across flow meter (lb_f/ft^2)

q = heat flux (positive if direction of transport is from wall to fluid) (BTU/hr)

Q = heat flux density = q/A ($BTU/hr \cdot ft^2$)

r = radial distance from the center line of the tube to a point of interest (ft)

r_i = net rate of disappearance of reactant species i [for the reaction $2\ A \rightleftarrows 3\ U$, r_A has units of (g-mole/cc·sec)]

r_o = tube radius (feet)

R = gas constant equal to 10.731 $ft^3\ lb_f/in^2$ lb mole ^oR = 1.987 cal/mole ^oK = 82.06 cm^3 atm/mole ^oK

t = time (min)

T^+ = normalized temperature (for case of bulk gas consisting mostly of NO_2 — negligible decomposition) defined by

$$T^+ \equiv \frac{\left(C_{p_\xi}\right)_{NO_2} (T_w - T)\ \tau_w\ g_c}{Q_w\ (\tau_w\ g_c/\rho_w)^{\frac{1}{2}}}$$

T = temperature (^oF)

u = local longitudinal velocity at some location within the pipe (ft/sec)

U = mass average velocity defined by $U \equiv m/\rho_b \pi r_\sigma^2$ (ft/sec)

x = distance between two locations of temperature measurement (in)

x_{NO_2} = mole fraction of NO_2

y = distance from the pipe wall to a point of measurement (ft)

y_i = mass fraction of species i

y^+ = normalized distance from the pipe wall defined by

$$y^+ \equiv \frac{(\tau_w \, g_c/\rho_w)^{\frac{1}{2}}}{(\mu_w/\rho_w)} \, y$$

Y = an expansion factor related empirically to the discharge or flow coefficient for a gas to that for a liquid at the same Reynolds number

z = longitudinal position in test section (ft)

Greek Symbols:

β = ratio of orifice diameter to pipe diameter

ϵ = wall roughness (rms inches)

ϵ_H = turbulent eddy diffusivity for energy transfer defined by

$$\epsilon_H \equiv \left[(Q_w/\rho \; C_p)(1 - \frac{y}{r_o}) \right] \left(- \frac{\partial \overline{T}}{\partial y} \right)_z^{-1} - \frac{k}{\rho \; C_p} \quad (ft^2/sec)$$

ϵ_H' = modified turbulent eddy diffusivity for energy transfer defined by

$$\epsilon_H' \equiv \left[(Q_w/\rho)(1 - \frac{y}{r_o}) \right] \left(- \frac{\partial \overline{H}}{\partial y} \right)_z^{-1} - \frac{k}{\rho \; C_p} \quad (ft^2/sec)$$

ϵ_M = turbulent eddy diffusivity for momentum transfer defined by

$$\epsilon_M \equiv \left[(\tau_w \; g_c/\rho)(1 - \frac{y}{r_o}) \right] \left(\frac{\partial \overline{U}}{\partial y} \right)_z^{-1} - \frac{\mu}{\rho} \quad (ft^2/sec)$$

ϵ_{M_ξ} = turbulent eddy diffusivity for momentum transfer in a non-reacting (or "locally" frozen) flow (definition as for ϵ_M) (ft^2/sec)

ϵ_m = turbulent eddy diffusivity for mass transfer defined by

$$\epsilon_m \equiv \left[J_{i_r}^{(t)}/\rho\right]\left(-\frac{\partial y_2}{\partial y}\right)_z^{-1} - \bar{D} \quad (ft^2/sec)$$

$\epsilon_{NO_2}(\lambda,T)$ = extinction coefficient for NO_2 at wavelength, λ, and temperature, T [$(mole/liter)^{-1}$ cm^{-1}]

η = ratio of equilibrium to frozen thermal conductivities

$$\eta = k/k_\xi$$

η' = ratio of equilibrium to frozen isobaric specific heats

$$\eta' = C_P/C_{P_\xi}$$

$\bar{\eta}$ = linear average of η and η'

$$\bar{\eta} = \frac{\eta + \eta'}{2}$$

λ = wavelength of light (angstroms)

$\lambda_{99\%}$ = pipe diameters downstream from entrance to test section (where zone of constant wall heat flux begins) at which the reaction rate reaches a constant value with axial position; defined by (20)

$$\lambda_{99\%} = \frac{4.6\ N_{Re_{b'}}\ N_{Sc_{b'}}}{m_c\ \eta_c'\ (N^*_{Nu_c})^2}$$

λ_c = dimensionless temperature difference defined by

$$\lambda_c \equiv \frac{H^{\dagger}\ (T_w - T_c)}{RT_c^{\ 2}}$$

μ = viscosity (lb_m/ft sec)

μ_c = a dimensionless temperature level defined by the equation

$$\mu_c \equiv RT_c/H^{\dagger}$$

ξ = degree of advancement of a chemical reaction, for $2\ A \rightleftarrows 3\ U$,

$$\xi = \frac{1 - x_{NO_2}}{1 + \frac{x_{NO_2}}{2}} \quad \text{(gm moles)}$$

ρ = mass density (lb_m/ft^3)

τ = shear stress (lb_f/ft^2)

τ'_{C_i} = characteristic chemical reaction time (sec)

$$(\tau'_{C_{NO_2}})^{-1} \equiv k_D\ C_{NO_2}$$

τ_D = characteristic molecular diffusion time (sec); for example

$$\tau_D \equiv \frac{d_p^2}{\bar{D}}$$

τ_F = characteristic flow time (sec); for example

$$\tau_F \equiv \frac{d_p}{U}$$

φ = heat transfer coefficient ratio defined by $\varphi \equiv h''/h^*$

[h^* based on N_{Re_f} and $N_{Pr_f} = 0.7$ (49)]

χ = a function of the reaction rate parameter - characteristic diffusion length product $\psi \ell$

$$\chi \equiv \left\{ 1 + \frac{\tanh(\psi_c \ell)}{(\psi_c \ell)} \left[\frac{k - k_\xi}{k_\xi} \right] \right\}$$

ψ = reaction rate parameter defined by (13)

$$\psi \equiv \left\{ \left[\frac{k}{k_\xi (k - k_\xi)} \right] \left(\frac{\Delta \tilde{H}_R}{RT} \right)^2 R \, r_i \right\}^{\frac{1}{2}} \quad (cm^{-1})$$

$\theta_t'(f)$ = rms fluctuating temperature at frequency f (^oF/cps)

$$\theta_t'(f) = [\overline{\theta_t^2}(f)]^{\frac{1}{2}}$$

$\theta_c'(f)$ = rms fluctuating concentration at frequency f [(moles/liter)/cps]

Θ_t' = total rms fluctuating temperature (over the entire frequency range) (^oF)

Θ_u' = total rms fluctuating velocity (over the entire frequency range) (ft/sec)

Θ_c' = total rms fluctuating concentration (over the entire frequency range)(moles/liter)

Superscripts:

' = refers to the use of an enthalpy reference rather than a temperature reference film condition

' = root mean square value of a fluctuating quantity

* = refers to orifice plate measurement, property based on orifice plate measurement; or parameter derived from nonreacting flow experiments

Subscripts:

A = refers to the cross sectional area of the pipe wall or to the upper static pressure port

b	=	refers to properties of the bulk gas
B	=	refers to the lower static pressure port
c	=	refers to a value corrected for instrument error or to properties evaluated at the pipe center line temperature
cs	=	refers to control settings (back wall of test section or bulk gas before the entrance plenum)
e	=	chemical equilibrium state
f	=	refers to properties evaluated at the film temperature defined by $T_f \equiv (T_w + T_b)/2$
f'	=	refers to properties evaluated at a film temperature corresponding to $H_f \equiv (H_w + H_b)/2$
F	=	designates frictional pressure drop
g	=	refers to the gas used to pressurize instrument lines
h	=	refers to the period of time during which the heater at the probe location was on
i	=	refers to insulation or to the inside pipe dimensions
L	=	refers to longitudinal measurements along the pipe wall
m	=	average value
M	=	refers to the manometer or manometer fluid
ow	=	refers to measurements made at the outer pipe wall
op	=	orifice plate (flange taps, square edged orifice)
pt	=	pitot tube (or total head - static pressure)
sp	=	static pressure (at wall along tube length)
T	=	refers to the total quantity or total time interval

w	=	refers to measurements made at the inside pipe wall of the test section
1,2	=	denotes different radial positions in the test section insulation; or 1 = upstream position, 2 = downstream position
ξ	=	refers to a property evaluated at frozen conditions
∞	=	refers to bulk gas conditions before entering the test section

Overlines:

$\bar{\ }$	=	refers to a value averaged over the length of the pipe
$\bar{\ }$	=	time average

Mathematical Symbols:

ln	=	natural or Naperian logarithm
π	=	3.1416

APPENDIX 1

EQUATIONS FOR DATA REDUCTION

Energy Transport:

$$H_b = \frac{2\pi}{m}\int_o^{r_o} r\ u\ \rho\ H\ dr \tag{A-1}$$

T_b, = temperature corresponding to H_b

Momentum Transport:

$$m = 2\pi\int_o^{r_o} r\ u\ \rho\ dr \tag{A-2}$$

$$G = \frac{m}{\pi\ r_o^2} \tag{A-3}$$

$$m^* = \frac{\pi\ d^2}{4}\left\{\frac{C\ Y_1}{(1-\beta^4)^{\frac{1}{2}}}\right\}\left[2\ g_c\ \rho_1\ (\Delta\ P)_{op}\right]^{\frac{1}{2}} \tag{A-4}^*$$

$$u = \left[2\ g_c\ (\Delta\ P)_{pt}/\rho\right]^{\frac{1}{2}} \tag{A-5}$$

$$(\Delta\ P)_{sp} = \left[h(\rho_M - \rho_g) - K_A\ \rho_A + K_B\ \rho_B\right]\frac{g}{g_c} \tag{A-6}^*$$

$$\frac{(\Delta\ P)_F}{L} = \frac{(\Delta\ P)_{sp}}{L} + \frac{m^2}{g_c\ (\pi\ r_o^2)}\left[\frac{1}{\rho_{b_1}} - \frac{1}{\rho_{b_2}}\right] + \frac{g}{g_c}\ \bar{\rho}_b \tag{A-7}$$

$$\rho_b = \frac{\int_o^{r_o} 2\pi\ \rho\ r\ dr}{\pi\ r_o^2} \tag{A-8}$$

---

*Note: $\Delta P \equiv P_1 - P_2$.

$$\bar{\rho}_b = \frac{\int_1^2 \rho_b \, d\,z}{L} \tag{A-9}$$

$$(\Delta\ P)_{op\ or\ pt} = \left[\ h\ (\rho_M - \rho_g)\ \right] \frac{g}{g_c} \tag{A-10}$$

$$f = \frac{D_i\ g_c}{4\ L} \left\{ \frac{(\Delta\ P)_F}{\left[\frac{1}{2}\ \bar{\rho}_b\ U^2\right]} \right\} \tag{A-11}$$

$$\tau_w = \frac{D_i}{4\ L}\ (\Delta\ P)_F \tag{A-12}$$

<u>Kinetics Parameters</u>* ($2\ NO_2 \rightleftarrows 2\ NO + O_2$):

$$k_D = 10^{12.60} \exp\left[\ \frac{-26{,}900}{RT}\ \right] \qquad \left[\ \frac{cm^3}{gm\ mole\ sec}\ \right] \tag{A-13}$$

$$k_{F_B} = \frac{k_D}{(RT)^2}\ ;\ k_{R_B} = \frac{k_R}{(RT)^3} = k_{F_B}/K_p(T) \tag{A-14}$$

For $2NO_2 \rightleftarrows 2NO + O_2$ approximated by $2A \rightleftarrows 3U$

$$-\ r_{NO_2} = \left[\frac{d\ C_{NO_2}}{d\ t}\right]_{\substack{chemical \\ reaction}} = -k_D\ C^2_{NO_2} + k_R\ C^3_U \tag{A-15}$$

$$C = P/RT \tag{A-16}$$

$$D\ (T;P) = \frac{(1\ atm)}{(P\ atm)}\ D\ (T,1\ atm) \tag{A-17}$$

$$D\ (T,1\ atm) = \left[\ \frac{D_{NO_2-NO} + D_{NO_2-O_2}}{2}\ \right]_{T,1\ atm} \tag{A-18}^*$$

*Values obtained from reference 26.

Concentration Calculations:

$$\frac{I}{I_o} = \exp\left(-\varepsilon_i \ell C_i\right) \qquad C_i = \overline{C}_i + c_i \qquad I \equiv a\,E \tag{A-19}$$

Time-Average Concentration:

For c_i small,

$$\overline{C}_i = -\frac{1}{b_i} \ln \frac{\overline{E}}{\overline{E}_o} \tag{A-20}$$

For c_i large,

$$\overline{C}_i \simeq -\frac{1}{b_i} \ln \frac{\dfrac{\overline{E}}{\overline{E}_o}}{\left[1 + \dfrac{b_i^2}{2}\,\overline{c_i^2}\right]} \tag{A-21}$$

RMS Concentration at Frequency, f ($e/\overline{E}$ small):

$$\theta'_{C_{NO_2}}(f) = \frac{\left[(e'_S)_{Air} - (e'_S)_{NO_2}\right]_f}{G_2\,(b_{NO_2}\,\overline{E}/G_1)\,(BW)^{\frac{1}{2}}} \tag{A-22}$$

$$(e'_S)_{f_{Air}} = \left[(e'_{S+N})^2_{Air} - (e'_N)^2\right]^{\frac{1}{2}}_f \tag{A-22a}$$

$$(e'_S)_{f_{NO_2}} = \left[(e'_{S+N})^2_{NO_2} - (e'_N)^2\right]^{\frac{1}{2}}_f \tag{A-22b}$$

$$G_1 = 100 \;;\quad G_2 = 10$$

Total RMS Concentration ($e/\overline{E}$ small):

$$\Theta'_{C_{NO_2}} = \frac{\left[(e'_S)_{Air} - (e'_S)_{NO_2}\right]}{G_2\,(b_{NO_2}\,\overline{E}/G_1)} \tag{A-23}$$

Fluctuating Temperature:

$$\theta'_t(f) = \frac{\left(\overline{e^2_{S+N}} - \overline{e^2_N}\right)^{\frac{1}{2}}_f}{CG\,(BW)^{\frac{1}{2}}} = \left[\overline{\theta^2_t}(f)\right]^{\frac{1}{2}} \tag{A-24}$$

$$\Theta'_t = \frac{\left(\overline{e^2_{S+N}} - \overline{e^2_N}\right)^{\frac{1}{2}}}{CG} = \left[\overline{\Theta^2_t}\right]^{\frac{1}{2}} \tag{A-25}$$

$G = 12{,}600$

$C = 5.34 \times 10^{-6}$ volts/^{o}F (Pt/Pt-10% Rh @ $\sim 800^{o}$F)

$BW = 5.52$ Hz

$$k_1 = \frac{2\pi f}{\overline{U}} \tag{A-26}$$

$$\overline{\theta_t^2}(k_1) = \frac{\overline{U}}{2\pi}\,\overline{\theta_t^2}(f) \tag{A-27}$$

$$k_{1_D} = \frac{2\pi}{D}\ ;\ k_{1_{\ell_{TS}}} = \frac{2\pi}{\ell_{TS}} \tag{A-28}$$

$$f_D = \frac{\overline{U}}{D}\ ;\ f_{\ell_{TS}} = \frac{\overline{U}}{\ell_{TS}} \tag{A-29}$$

REFERENCES

1. Richardson, John L. "Heat Transfer in an Equilibrium Chemically Reacting System." Ph.D. Dissertation. Stanford, California: Department of Chemical Engineering, Stanford University (1964).

2. Brokaw, R. S. "Energy Transport in High Temperature and Reacting Gases." Planetary and Space Sciences, Vol. 3 (February 1961), pp. 238-252.

3. Spalding, D. B. "Heat Transfer from Reacting Systems." in Modern Developments in Heat Transfer, Ibele, W. E. (Editor), New York: Academic Press (1963), pp. 19-64.

4. Chung, Paul M. "Chemically Reacting Nonequilibrium Boundary Layers." in Advances in Heat Transfer, Hartnett, James P., and Irvine, Thomas F., Jr. (Editors), Volume 2, New York: Academic Press (1965), pp. 109-268.

5. Krieve, Walter F., and Mason, David M. "Heat Transfer in Reacting Systems: Heat Transfer to Nitrogen Dioxide Gas under Turbulent Pipe Flow Conditions." A.I.Ch.E. Journal, Volume 7 (1961), pp. 277-281.

6. Richardson, J. L., et al. "Heat Transfer in Reacting Systems — Heat Transfer to N_2O_4 Gas Flowing Normally to a Heated Cylinder." Chemical Engineering Science, Vol. 13 (February 1961), pp. 130-142.

7. Richardson, J. L., and Mason, D. M. "Energy and Momentum Transport in an Equilibrium Reacting Wake Behind a Heated Cylinder." Preprint 25b, Symposium on Simultaneous Diffusion and Chemical Reaction; 57th Annual Meeting - A.I.Ch.E., Boston, Massachusetts. New York: American Institute of Chemical Engineers (December 1964).

8. Fan, S.S.T., Rozsa, R. A., and Mason, D. M. "Heat Transfer in Reacting Systems — Effect of Chemical Kinetics on the Thermal Conductivity of Gases." Chem. Eng. Science, Vol. 18 (1963), pp. 737-752.

9. Bopp, Gordon R., and Mason, David M. "Experimental Natural Convection Heat Transfer from Wires to Nonequilibrium Chemically Reacting Systems: NO_2-NO-O_2." I&EC Fundamentals, Vol. 4 (1965), p. 222.

10. Callaghan, Michael J., and Mason, David M. "Momentum and Heat Transfer Correlations for a Reacting Gas in Turbulent Pipe Flow." A.I.Ch.E. Journal, Vol. 10 (January 1964), pp. 52-55.

11. Brokaw, Richard S. "Correlation of Turbulent Heat Transfer in a Tube for the Dissociating System $N_2O_4 \rightleftarrows 2\ NO_2$." NACA RM E57K19a (1958).

12. Brokaw, Richard S. "'Thermal Conductivity' and Chemical Kinetics." J. Chem. Phys., Vol. 35 (November 1961), pp. 1569-1580.

13. Svehla, Roger A., and Brokaw, Richard S. "Thermodynamic and Transport Properties for the $N_2O_4 \rightleftarrows 2\ NO_2 \rightleftarrows 2\ NO + O_2$ System." NASA TN D-3327, Washington, D.C.: NASA (March 1966).

14. Irving, J. P., and Smith, J. M. "Heat Transfer in a Chemically Reacting System (Nitrogen Tetroxide-Dioxide)." A.I.Ch.E. Journal, Vol. 7 (1961), pp. 91-96.

15. Furgason, R. R., and Smith, J. M. "Heat Transfer in the Nitrogen Dioxide-Nitrogen Tetroxide System." A.I.Ch.E. Journal, Vol. 8 (1962), pp. 654-658.

16. Rothenberg, R. I., and Smith, J. M. "Heat Transfer and Reaction in Laminar Tube Flow." A.I.Ch.E. Journal, Vol. 12 (1966), pp. 213-220.

17. Rothenberg, R. I., and Smith, J. M. "Dissociation and Heat Transfer in Laminar Flow." Canadian Journal of Chemical Engineering, Vol. 44 (1966), pp. 67-73.

18. Presler, Alden F. "An Experimental Investigation of Heat Transfer to Turbulent Flow in Smooth Tubes for the Reaction N_2O_4-NO_2 System." NASA TN D-3230, Washington, D.C.: NASA (January 1966).

19. Brian, P.L.T., and Reid, R. C. "Heat Transfer with Simultaneous Chemical Reaction: Film Theory for a Finite Reaction Rate." A.I.Ch.E. Journal, Vol. 8 (July 1962), pp. 322-329.

20. Brian, P.L.T. "Turbulent Pipe Flow Heat Transfer with a Simultaneous Chemical Reaction of Finite Rate." A.I.Ch.E. Journal, Vol. 9 (November 1963), pp. 831-841.

21. Brian, P.L.T., and Bodman, S. W. "The Effect of Temperature Driving Force on Heat Transfer to a Nonequilibrium Chemically Reacting Gas." I&EC Fundamentals, Vol. 3 (November 1964), pp. 339-346.

22. Brian, P.L.T., Reid, R. C., and Bodman, S. W. "Heat Transfer to Decomposing Nitrogen Dioxide in a Turbulent Boundary Layer." A.I.Ch.E. Journal, Vol. 11 (1965), pp. 809-814.

23. Brian, P.L.T., and Bodman, S. W. "Turbulent Heat Transfer to a Nonequilibrium Chemically Reacting Gas." I&EC Fundamentals, Vol. 6 (1967), pp. 89-97.

24. Edwards, L. L., and Furgason, R. R. "Heat Transfer in the Thermally Decomposing Ozone System: Theoretical Investigation." Chemical Engineering Progress Symposium Series, Vol. 61, No. 59 (1965), pp. 299-306.

25. Edwards, L. L., and Furgason, R. R. "Heat Transfer in the Thermally Decomposing Ozone System: Experimental Investigation." Paper 17a Presented at the 59th Annual Meeting of the A.I.Ch.E., Detroit, Michigan (December 1966).

26. Bodman, Sam W. "Heat Transfer Accompanied by a Nonequilibrium Reversible Chemical Reaction." Sc.D. Thesis, Department of Chemical Engineering, Cambridge Massachusetts: Massachusetts Institute of Technology (November 1964).

27. Brodkey, Robert S. "The Phenomena of Fluid Motions." Reading, Massachusetts: Addison-Wesley Publishing Company (1967), pp. 343-351.

28. Beek, John, Jr., and Miller R. S. "Turbulent Transport in Chemical Reactors." Chemical Engineering Progress Symposium Series, Vol. 55, No. 25 (1959), pp. 23-28.

29. Corrsin, Stanley. "Statistical Behavior of a Reacting Mixture in Isotropic Turbulence." Physics of Fluids, Vol. 1 (1958), pp. 42-47.

30. Lee, Jon. "Isotropic Turbulent Mixing under a Second-order Chemical Reaction." Physics of Fluids, Vol. 9 (September 1966), pp. 1753-1763.

31. Chung, Paul M. "A Simplified Statistical Description of Turbulent Chemically Reacting Flows." Report No. TR-1001 (S2855-20)-5. San Bernardino, California: Aerospace Corp. (1967).

32. Toor, H. L. "Mass Transfer in Dilute Turbulent and Non-turbulent Systems with Rapid Irreversible Reactions and Equal Diffusivities." A.I.Ch.E. Journal, Vol. 8 (1962), pp. 70-78. See reference 27 for a brief review of more recent results obtained by Toor and coworkers.

33. Rosser, W. A., and Wise, H. "Thermal Decomposition of Nitrogen Dioxide." J. Chem. Phys., Vol. 24 (1956), pp. 493-494.

34. Ashmore, P. G., and Burnett, M. G. "Concurrent Molecular and Free Radical Mechanisms in the Thermal Decomposition of Nitrogen Dioxide." Trans. Faraday Soc., Vol. 58 (1962), pp. 253-261.

35. Ashmore, P. G., and Levitt, B. P. "Thermal Decomposition of Nitrogen Dioxide." Research Correspondence, Vol. 9 (1956), pp. 525-526.

36. Brokaw, R. S., and Svehla, R. Private Communication (February 9, 1967).

37. Fan, S.S.T., and Mason, D. M. "Properties of the System $N_2O_4 \rightleftarrows 2\ NO_2 \rightleftarrows 2\ NO + O_2$." Journal of Chemical and Engineering Data, Vol. 7 (April 1962), pp. 183-186.

38. Giauque, W. F., and Kemp, J. D. "The Entropies of Nitrogen Tetroxide and Nitrogen Dioxide." J. Chem. Phys., Vol. 6 (1938), pp. 40-52.

39. Rodriquez-Ramirez, Abraham. "Characteristics of Turbulent Temperature Fluctuations in Air." M.S. Thesis. Lafayette, Indiana: Department of Nuclear Engineering, Purdue University (June 1965).

40. Rust, J. H., and Sesonske, Alexander. "Turbulent Temperature Fluctuations in Mercury and Ethylene Glycol in Pipe Flow." International Journal of Heat and Mass Transfer, Vol. 9 (1966), pp. 215-227.

41. Brophy, James J. "Low Noise Modifications of the Tektronix Type 122 Preamplifier." Rev. of Sci. Instru., Vol. 26 (1955), p. 1076.

42. Eisenman, W. L. "Tektronix Type 122 Preamplifier Modification." Applied Optics, Vol. 4 (1965), p. 512.

43. Rust, James H. "Characteristics of Turbulent Temperature Fluctuations in Mercury and Ethylene Glycol." Ph.D. Thesis. Lafayette, Indiana: Department of Nuclear Engineering, Purdue University (1965).

44. Lee, Jon, and Brodkey, Robert S. "Light Probe for the Measurement of Turbulent Concentration Fluctuations." The Review of Scientific Instruments, Vol. 34 (October 1963), pp. 1086-1090.

45. Nye, James O., and Brodkey, Robert S. "Light Probe for Measurement of Turbulent Concentration Fluctuations." The Review of Scientific Instruments, Vol. 38 (January 1967), pp. 26-28.

46. Schott, Garry L. "Chemical Studies in Shock Waves." Ph.D. Thesis. Pasadena, California: California Institute of Technology (1956).

47. Schott, Garry, and Davidson, Norman. "Shock Waves in Chemical Kinetics: The Decomposition of N_2O_5 at High Temperatures." J.A.C.S., Vol. 80 (1958), pp. 1841-1853.

48. McAdams, W. H. Heat Transmission. Third Edition. New York: McGraw-Hill Book Company, Inc. (1954).

49. Sparrow, E. M., et al. "Turbulent Heat Transfer in the Thermal Entrance Region of a Pipe with Uniform Heat Flux." Appl. Sci. Res., Ser. A, Vol. 7 (1957), pp. 37-52.

50. Perry, Robert H., et al. (Editors) Chemical Engineers' Handbook, Fourth Edition. New York: McGraw-Hill (1963), pp. 5-20.

51. Hinze, J. O. Turbulence - An Introduction to its Mechanism and Theory. New York: McGraw-Hill Book Company, Inc. (1959).

52. Knudsen, James G., and Katz, Donald L. Fluid Dynamics and Heat Transfer. New York: McGraw-Hill (1958).

53. Callaghan, Michael J. "Heat Transfer to a Dissociating Gas in Fully Developed Turbulent Flow between Asymmetrically Heated Parallel Plates." Ph.D. Dissertation. Stanford, California: Department of Chemical Engineering, Stanford University (1963).

54. Tanimoto, S., and Hanratty, T. J. "Fluid Temperature Fluctuations Accompanying Turbulent Heat Transfer in a Pipe." Chem. Eng. Sci., Vol. 18 (1963), pp. 307-311.

55. Vassilatos, G., and Toor, H. L. "Second-Order Chemical Reactions in a Nonhomogeneous Turbulent Fluid." A.I.Ch.E. Journal, Vol. 11 (1965), pp. 666-673.

56. Saidel, G. M., and Hoelscher, H. E. "Chemical Reaction in the Turbulent Wake of a Cylinder." A.I.Ch.E. Journal, Vol. 11 (1965), pp. 1058-1063.